Hall A Annual Report
2010

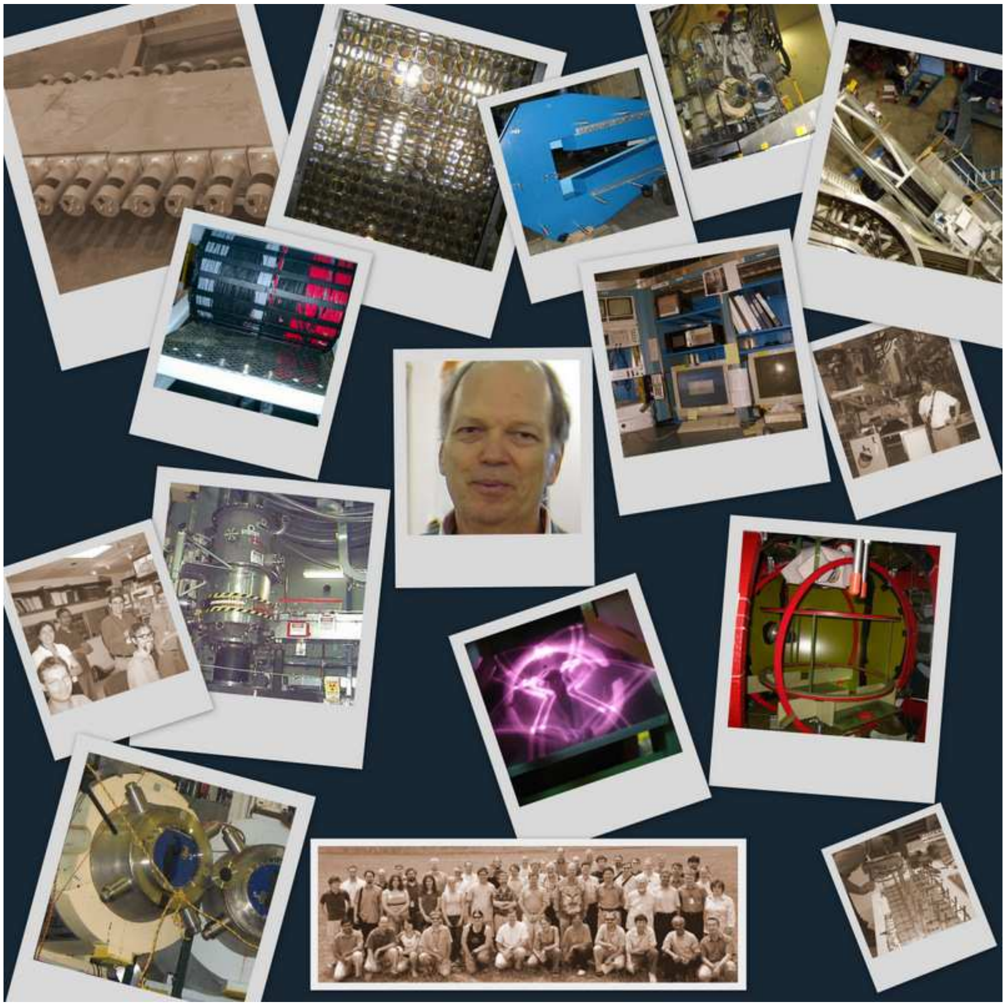

Edited by Guy Ron & Kees de Jager

Contents

1 Introduction 6

2 General Hall Developments 7
- 2.1 Polarized ^{3}He Target 7
  - 2.1.1 Overview 7
  - 2.1.2 Hardware Set-up 7
  - 2.1.3 Auto Spin Flip and Polarimetry 8
- 2.2 Møller Polarimeter (Configuration #2) 10
  - 2.2.1 Introduction 10
  - 2.2.2 General description 10
  - 2.2.3 The Polarized Target 11
  - 2.2.4 The Target Polarization Measurement 12
  - 2.2.5 The Beam Polarization Measurement 15
  - 2.2.6 The Møller Polarimeter Systematic Error 16
- 2.3 Fifteen nanosecond coincidence time between HRSs 19

3 Summaries of Experimental Activities 20
- 3.1 E03-101 20
  - 3.1.1 ^{3}He(γ,pp)n 20
  - 3.1.2 ^{3}He(γ,pd) 21
- 3.2 C12-10-009 26
  - 3.2.1 Introduction 26
  - 3.2.2 Expected reach and impact 26
  - 3.2.3 Concept 27
  - 3.2.4 PAC35 report and concerns 28
  - 3.2.5 The results of the test run and the future plans 28
- 3.3 E06-014 30
  - 3.3.1 The Experiment 30
  - 3.3.2 Analysis Progress: Left HRS 32
  - 3.3.3 Analysis Progress: BigBite 34
  - 3.3.4 Analysis Progress: Target 38
- 3.4 E07-007/E08-025 44
  - 3.4.1 Goals of the experiments 44
  - 3.4.2 Experimental status 44
  - 3.4.3 Data acquisition 46
  - 3.4.4 Polarimetry and helicity 47
- 3.5 E06-002 48
- 3.6 E05-015 54
  - 3.6.1 Introduction 54
  - 3.6.2 Experiment overview 54
  - 3.6.3 Analysis 54
  - 3.6.4 Results 55
- 3.7 E08-027 56
  - 3.7.1 Introduction 56
  - 3.7.2 The Experiment 56
- 3.8 E06-010 Transversity 58
  - 3.8.1 Introduction 58
  - 3.8.2 Summary of Pressure Curve Analysis in E06-010 58
  - 3.8.3 Cross Check between MLE and Angular-bin-fit Methods 69
  - 3.8.4 SIMC-Transversity 71
  - 3.8.5 Preliminary Results 73

4 Publications 81

5 Theses **82**

6 Hall A Collaboration Member List **83**

List of Figures

1 The polarized ^{3}He target setup. 7
2 The water NMR signal with fit. 8
3 An EPR measurement on a K atom. 9
4 Photo of the target chamber of the Møller polarimeter in Hall A. 11
5 Lay-out of the Møller polarimeter 12
6 The target holder design. 13
7 The polarized electron target holder in assembly. 13
8 The magnetic stand for magnetization measurements of the ferromagnetic foils. 15
9 Polarization profile for Target 2 (Supermendure 29.4 μm thick). 16
10 Correction of the measured beam polarization for beam energy fluctuations. 17
11 The d(γ,p)n (a) and ^{3}He(γ,pp)n (b) invariant cross section scaled by s^{11}. 24
12 The invariant cross section $d\sigma/dt$ multiplied by s^{17} to remove the expected energy dependence. 25
13 The reach of the APEX experiment, the APEX test run and existing constraints. 27
14 The lay-out of the APEX experimental setup. 28
15 The components of the target for the APEX experiment. 29
16 E06-014: Current status of $\Delta q/q$ measurements 31
17 E06-014: Projected statistical errors for A_1^n measurement 31
18 E06-014: PID efficiency of the LHRS gas Čerenkov 32
19 E06-014: Pion and electron spectra in the LHRS pion rejectors 32
20 E06-014: Calibrated drift time spectrum for BigBite MWDC 34
21 E06-014: Time-to-distance conversion in BigBite MWDC 34
22 E06-014: BigBite track residuals. 35
23 E06-014: BigBite vertex reconstruction 36
24 E06-014: Continuity of momentum spectrum 36
25 E06-014: Reconstructed invariant-mass spectrum in BigBite 37
26 E06-014: Momentum resolution for BigBite negative optics 37
27 E06-014: Distribution of E vs. p for calibrated preshower and shower 37
28 E06-014: Calibration of BigBite gas Čerenkov 38
29 E06-014: BigBite gas Čerenkov ADC signal for a beam-side PMT 39
30 E06-014: BigBite gas Čerenkov ADC signal for a RHRS-side PMT 39
31 E06-014: Pion selection for BigBite gas Čerenkov studies 39
32 E06-014: Electron selection for BigBite gas Čerenkov studies 39
33 E06-014: Average pion rejection factors for the BigBite gas Čerenkov 40
34 E06-014: BigBite gas Čerenkov electron efficiency (small-angle side) 40
35 E06-014: BigBite gas Čerenkov electron efficiency (large-angle side) 40
36 E06-014: Interference phenomenon in glass-thickness measurements. 41
37 E06-014: EPR measurements 42
38 E06-014: Preliminary pumping-chamber polarizations 43
39 Left: DVCS stand. Right: Calorimeter in position in the hall. 45
40 DVCS calorimeter energy resolution 45
41 DVCS on-line results 46
42 Calorimeter Gain variation 46
43 The slug plot for PREX asymmetry. 49
44 Shifted, blinded asymmetry for a positive product of half-waveplate and Wien filter. 49
45 Same as figure 44 except for a negative product of half-waveplate and Wien filter. 50
46 Simulated and reconstructed scattering angle. 51
47 Simulated rates in one HRS versus Q^2 for two assumptions about septum current setting. . . 52
48 The raw asymmetry, sensitivity to R_N, and error in R_N as functions of Q^2. 53
49 The preliminary ^{3}He target single-spin asymmetries at $Q^2 = 0.98$ GeV^2. 55
50 E08-027 Projected Uncertainties 57
51 Schematic view of the ^{3}He glass cell 59
52 Vertex Z cut for the production cell. Only the shadowed region is selected. 60

53 ^{3}He missing-mass spectrum of the reference-cell and the production-cell runns. 61
54 ^{14}N missing-mass spectrum of the reference-cell and the production-cell runs. 62
55 Single-track efficiency for each run. 63
56 Yield vs. density for the reference-cell ^{3}He runs. 63
57 ^{3}He missing-mass spectrum of simulation (red) and data (black). 64
58 The ratio between the simulated yields of the reference-cell runs and those of the production-cell run. 65
59 Vertex dependence of the density due to the temperature distribution. 65
60 The density curve of the reference-cell ^{3}He runs, fit to a straight line. 66
61 The density curve of the reference cell N_2 runs, fit to a straight line. 66
62 Yields with the ^{3}He elastic cut for the production-cell runs, fit to a constant. 67
63 Yields for the production-cell runs with the ^{14}N elastic cut, fit to a constant. 67
64 Yields for the reference-cell runs with the ^{3}He cuts, fit to a constant. 68
65 Cross-check of the two-term extraction of the DSA modulations for the $^3\mathrm{He}^{\uparrow}(e, e'\pi^{\pm})$ channels. 70
66 Comparison of SIMC and data yields for the $^3\mathrm{He}(e, e'\pi^+)X$ and $^3\mathrm{He}(e, e'\pi^-)X$ reactions . . . 71
67 Comparison of the phase-space coverage in SIMC and data for Q^2, W, z, and W' as a function of x. 72
68 Successful maximum-likelihood extraction of the Collins and Sivers moments from “pseudo-data” 75
69 Results of subdividing a high-statistics SIMC run into 50 trials for an input asymmetry of 10% Sivers and 0% Collins. 76
70 Results of subdividing a high-statistics SIMC run into 50 trials for an input asymmetry of 0% Sivers and 10% Collins. 77
71 Results of subdividing a high-statistics SIMC run into 2500 trials for an input asymmetry of 10% Sivers and 0% Collins. 78
72 Results of subdividing a high-statistics SIMC run into 2500 trials for an input asymmetry of 0% Sivers and 10% Collins. 79
73 The preliminary results for the Collins and Sivers moments of ^{3}He. 80

1 Introduction

The first half of 2010 was a very difficult time for Hall A, especially for the technical support group. The installation for PREX already presented large challenges. First, the scattering chamber together with the two septum magnets had to be installed in the upstream position and carefully surveyed. Then, the cryotarget had to be artfully lowered into the scattering chamber in its new position. Finally, the connections between the scattering chamber and both the spectrometers and the exit beam line had to be fitted with great care. In the same period the old Hall C superconducting solenoid was installed in the Møller polarimeter. It was a great achievement that all of this was completed only two weeks late. Then, during the running of PREX the very high radiation caused by running 50 μA on a thick lead target caused several major and many minor interruptions of the production running. The PREX collaboration succeeded in achieving all its goals on systematic errors, but regrettably only collected 25% of the projected statistics. The start of the summer installation was shifted by three weeks in order to get first beam into Hall C for initial check-out of the Qweak installation. This gave PREX a much needed extension and made a very successful test run for the APEX experiment possible. In the APEX test run all of the concerns raised by PAC35 were successfully addressed and enough real data were collected to achieve a much improved lower limit on the possible existence of a vector boson, albeit in a limited mass range.

Notwithstanding the additional work caused by the radiation damage of a variety of equipment, the technical support staff succeeded in completing the installation for the two DVCS experiments on time. However, the start-up of DVCS was delayed by over three weeks by problems first with the End Station Refrigerator and then with the Analog Ring Sampling (ARS) electronics for the DVCS calorimeter read-out. After the late start both experiments ran smoothly, albeit at a lower luminosity until December 15, when the trigger board became operational. All in all, DVCS succeeded in collecting $\sim$75% of the projected data.

In 2010 essential progress was made on the research program in Hall A with the 12 GeV upgrade. Hall A now has nine fully approved and four conditionally approved proposals. For the upcoming PAC37 three new proposals have been submitted, together with resubmissions of all four conditionally approved proposals. Regrettably, no reports on the three large projects initiated for Hall A with the 12 GeV upgrade are presented in this Annual Report, but great progress has been made on all three in 2010. The funding proposal to DOE for the SuperBigBite (SBS) project regrettably was ignored due to a bureaucratic misunderstanding. It is now again being discussed with DOE as a two-phase process, where the first phase would be funded through JLab capital funding, while the second phase would be submitted as an MIE project. A second Technical Review, was held at JLab on January 2, 2010. While the summary stated that "The Committee is convinced that the SBS will be the instrument of choice for a large variety of important physics problems requiring large acceptance at small angles, high luminosity, and needing modest resolution, only", the committee listed a number of problems. All of those, except for one, have been resolved and the collaboration is working very hard to complete a full set of simulations and a tracking software package. The MOLLER experiment to study parity violation in scattering of longitudinally polarized 11 GeV electrons from the atomic electrons in a liquid hydrogen target (Møller scattering) has received a glowing recommendation from a Director's Review on January 14 and 15. The project was presented and discussed at DOE and an MIE proposal is being prepared with the goal to convince DOE to include MOLLER in its out-year projections. The PVDIS experiment (SoLID) to measure A_{PV} in the deep-inelastic scattering of polarized electrons to high precision in order to search for physics beyond the Standard Model in lepton-quark neutral current interactions was fully approved at PAC35, together with the SIDIS proposal that also uses the SoLID solenoid. Both experiments are now looking forward to a similar Director's Review as for MOLLER.

I would like to recognize the expertise, dedication and just plain hard work that made all this possible, by the design and engineering staff, Al Gavalya, Susan Esp, Joyce Miller, Al Chavira, Paul Brindza and our two new engineers Robin Wines and Whit Seay, and the technical staff Ed Folts, Jack Segal, Jessie Butler, Heidi Fansler, David Galinski, Andrew Lumanog, Howard Smith and Todd Ewing.

As this is the last Annual Report that I am contributing to, I would like to acknowledge the physics staff, Alexandre Camsonne, Jian-ping Chen, Javier Gomez, Ole Hansen, Doug Higinbotham, John LeRose, Bob Michaels, Sirish Nanda, Arun Saha, Bogdan Wojtsekhowski and our two new post-docs Kalyan Allada and Jixie Zhang. It has been a great pleasure to work with such a dedicated and highly qualified staff for fourteen years. I have also very much appreciated the support of and the positive interaction with the Hall A user community.=

2 General Hall Developments

2.1 Polarized ^{3}He Target

Contributed by Yi Qiang for the polarized ^{3}He target group

2.1.1 Overview

Recently, from October 2008 to June 2009, the Hall A polarized ^{3}He target [1] was successfully used for a series of experiments: neutron transversity (E06-010) [2], d_2^n (E06-014) [3], A_y^n (E05-015) [4], ^{3}He$(e,e'd)$ (E05-012) [5], DIS A_y^n (E07-013) [6] and semi-inclusive A_y^n ^{3}He$(e,e'n)$ (E08-005) [7] during their total 7 months of data taking.

The polarized ^{3}He target used optically pumped Rubidium vapor to polarize ^{3}He nuclei via spin-exchange in earlier Hall A experiments [8, 9, 10, 11, 12, 13]. Typical in-beam (10-15 μA) polarization steadily increased from 30% to over 40%. Since the Hall A G_E^n experiment [14], a new hybrid technique for spin-exchange which uses a K-Rb mixture [15] increased the in-beam polarization to over 50% (close to 60% without beam) due to the much higher K-^{3}He spin-exchange efficiency. The new hybrid cells also achieved significantly shorter spin-up times (5 hours compared to 10 hours for a pure Rb cell). Further improvement was made for the 2008-2009 series of ^{3}He experiments by using the recently available Comet high-power narrow line-width diode lasers instead of the Coherent broad line-width diode lasers that have been used previously. The target polarization improved significantly to 65% with 15 μA beam current and a 20-minute spin-flip and over 70% was achieved without beam.

2.1.2 Hardware Set-up

The design group (Al Gavalya, Susan Esp et al.) worked over a year to ensure the new system satisfied the stringent requirements of all six experiments with minimum change-over and very tight space constraints. A number of modifications and upgrades were implemented in the new design.

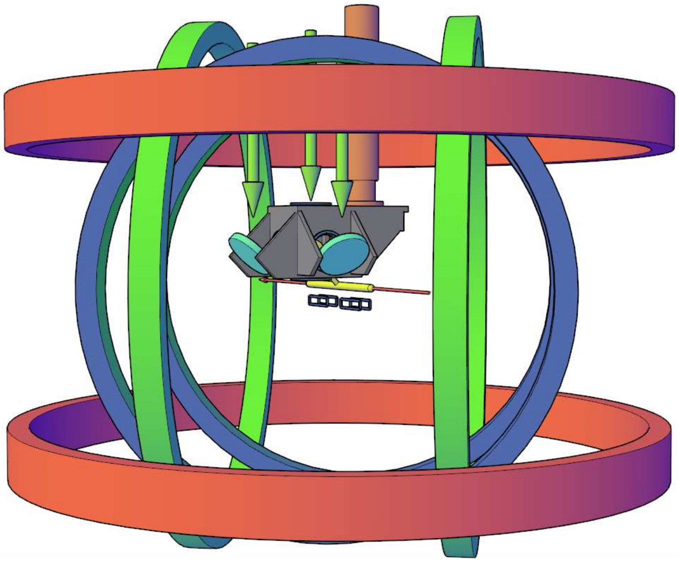

Figure 1: The polarized ^{3}He target setup.

The original system used two sets of Helmholtz coils to create a holding field up to 32 G in the scattering (horizontal) plane. The transversity and A_y experiments needed vertical polarization. Therefore, a third set of coils was built to provide the additional vertical field. Using all three sets of coils, target polarization in any direction in 3-D space is possible.

The target cells used in all experiments have a 3 inch diameter pumping chamber and a 40 cm long target chamber with density of about 10 amg (10 atm at 0°C). The luminosity is about 3×10^{36} nuclei/s/cm^2 with 15 μA beam. Two kinds of cells were built with different pull-off locations to accommodate different pumping direction combinations for each experiment: vertical and horizontal transverse for transversity and A_y^n, horizontal transverse and longitudinal for d_2^n and $(e,e'd)$. In total, six cells were used in beam with 10 to 15 μA and all survived.

A bigger oven which can hold both kinds of targets and allow all three pumping directions was built with CS85 structural insulation material. This new material has about half the density compared to the ceramics used in old ovens and much better insulation. The interior of the oven was painted black to reduce the internal laser reflection.

To minimize the change-over time and access to the hall, a total of fifteen long optical fibers connected the lasers from the upstairs laser room to the hall. They were then connected to three 5-to-1 optical fiber combiners so that up to five lasers could be used in each single polarizing direction (longitudinal, transverse and vertical). During the experiments, three higher-power (30 W) Comet (narrow line-width) lasers were used together. In a compact optical bench above the pivot area, the laser beam for each pumping direction was polarized after passing through an individual set of polarizing optics. The laser light then got reflected into the pumping cell by two mirrors. For transverse and vertical pumping directions, the two mirrors were in a polarization preserving configuration. However, this is not the condition for the longitudinal direction, which was required for the d_2^n and $(e, e'd)$ experiments. With no luck in finding a vendor to buy polarization preserving mirrors, a solution was found by using two, instead of one, pre-tuned 1/4-wave plates in front of the two mirrors to compensate the phase change. This solution worked very well for the Comet lasers thanks to their narrow line-width spectrum.

2.1.3 Auto Spin Flip and Polarimetry

With a lot of hard work by a dedicated group of students and postdocs (C. Dutta, J. Huang, J. Katich, Y. Zhang and Y. Qiang), the LabVIEW based control system and the polarimetry were upgraded with many new features.

Fast target spin reversals were needed for the transversity and A_y^n experiments (every 20 minutes). The spin reversal was achieved with the Adiabatic Fast Passage (AFP) technique and the polarizing laser spin direction reversal was accomplished with rotating 1/4-wave plates. The polarization loss due to fast spin reversal was less than 10% relative to the maximum polarization depending on the AFP loss and the spin up time. The improvement of spin-up time with the hybrid cell has significantly reduced the polarization loss due to the fast spin reversal. A sophisticated automatic spin-flip control system was written based on LabVIEW. The system automatically flipped the target spin every 20 minutes, recorded the NMR data during each AFP flips, validated the spin state from the sign of the NMR signals and updated the EPICS spin state. It also monitored most of the system variables, such as holding-field currents and target temperatures and would trigger alarms when problems occur. The whole target system worked very reliably during these experiments with more than five thousand flips.

Two kinds of polarimetry, NMR (Nuclear Magnetic Resonance) and EPR (Electron Paramagnetic Resonance), were used to measure the polarization of the target.

Two pairs of RF coils (vertical and longitudinal) and five pairs of NMR pick-up coils (three on the pumping chamber and two on the target chamber) were mounted inside the target chamber to perform NMR measurements for different spin directions. The magnetic flux of the polarized ^{3}He passing through the target chamber pick-up coils was calibrated using water NMR measurements with the calculable proton polarization. Three sets of water NMR data were taken, and the signal from one set of data is shown in Figure 2. The statistical error of the water NMR signal is much better than 1%. Taking into account the relative flux corrections due to different distances between the cells and the pick-up coils, the total uncertainty of the water calibration is better than 3%.

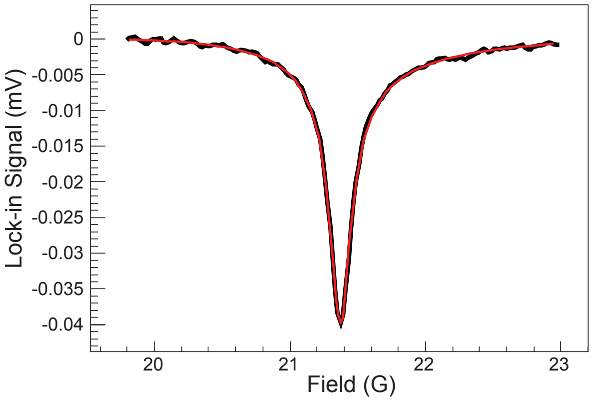

Figure 2: The water NMR signal (black) with fit (red).

The EPR measurements took place in the pumping chamber and both K and Rb EPR signals were used. Due to the much larger size of the oven, to have enough perturbative RF power, an EPR RF coil made of high-temperature enameled wire was put inside the oven. A collection system with two lenses was installed to have better EPR D2 light detection. Because EPR is a destructive measurement, new control and analysis software had been developed to shorten the time needed for a measurement. A complete EPR calibration now can be done within 5 minutes with better than 1% statistical uncertainty.

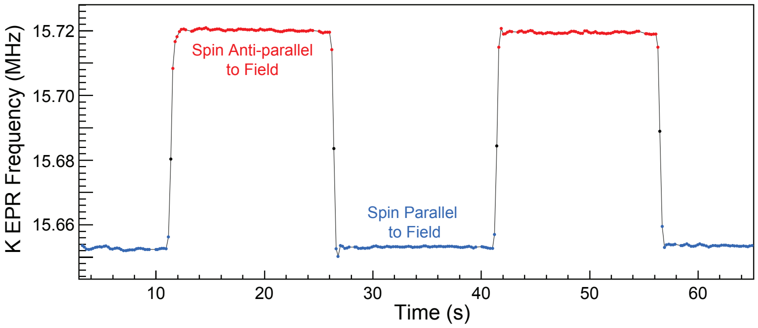

Figure 3: An EPR measurement on a K atom.

The target density and its distribution are crucial systematics for both NMR and EPR measurements. The densities of all production cells have been measured at JLab using pressure broadening with less than 2% statistical uncertainties and the results are consistent with independent measurements done at UVa using the same technique. The density of the first production cell used during transversity was also measured by the reference cell pressure curve. The preliminary analysis matches the pressure broadening result. To determine the density distribution, other than deploying seven RTD temperature sensors on the target cell, five on the target chamber and two on the pumping chamber, to monitor the cell surface temperature all the time, special internal temperature tests were done to determine the internal pumping chamber temperature to better than 5°C, which corresponds to less than 1% relative impact on the polarization results.

The analysis of EPR and NMR are ongoing and the preliminary results suggest that both methods agree within errors.

References

[1] http://hallaweb.jlab.org/targets/polhe3/polhe3tgt.html.

[2] JLab E06-010, Spokespersons; J. P.Chen, E. Cisbani, H. Gao, X. Jiang, and J. C. Peng.

[3] JLab E06-014, Spokespersons: S. Choi, X. Jiang, Z.-E. Meziani, and B. Sawatzky.

[4] JLab E05-015, Spokespersons: T. Averett, J. P. Chen, and X. Jiang.

[5] JLab E05-102, Spokespersons: S. Gilad, D. Higinbotham, W. Korsch, B. Norum, and S. Sirca.

[6] JLab E07-013, Spokespersons: T. Averett, T. Holmstrom, and X. Jiang.

[7] JLab E08-005, Spokespersons: T. Averett, D. Higinbotham, and V. Sulkosky.

[8] M. Amarian *et al.*, Phys. Rev. Lett. **89**, 242301 (2002).

[9] W. Xu *et al.*, Phys. Rev. Lett. **85**, 2900 (2000).

[10] X. Zheng *et al.*, Phys. Rev. Lett.**92**, 012004 (2004).

[11] K. Kramer *et al.*, Phys. Rev. Lett. **95**, 142002 (2005).

[12] P. Solvignon *et al.*, Phys. Rev. Lett. **101**, 182502 (2008).

[13] JLab E97-110, Spokespersons: J. P. Chen, A. Deur, and F. Garibaldi.

[14] JLab E02-013, Spokespersons: G. Cates, N. Liyanaga, and B. Wojtsekhowski.

[15] E. Babcock *et al.*, Phys. Rev. Lett. **91**, 123003 (2003).

2.2 Møller Polarimeter (Configuration #2)

E. Chudakov, O. Glamazdin, R. Pomatsalyuk, J. Zhang

2.2.1 Introduction

The Møller polarimeter in Hall A measures the polarization of beam electrons in an energy range of 0.8–6.0 GeV. The polarimeter consists of a polarized electron target and a magnetic spectrometer, which detects the pair of scattered electrons. Magnetized ferromagnetic foils are used for the polarized target. Three target configurations have been used so far[1]:

Configuration #1: (1998-2004) A Supermendure foil which could be rotated around Y, magnetized by a $B_Z \sim 0.026$ T field;

Configuration #2: (2005-2009) Several foils, of Supermendure and iron, fixed at an angle of 20.5° to the beam in the YZ plane, magnetized by a $B_Z \sim 0.035$ T field;

Configuration #3: (2009-2010) Several iron foils perpendicular to the beam, magnetized by a $B_Z \sim 4$ T field;

In configurations #1-2 the magnetizations of the targets were measured before their installation, at different magnetic fields. For configuration #3 the magnetization was assumed to be fully saturated and taken from the world data on properties of pure iron. The average polarization of the electrons in the target is derived from the value of the magnetization. In configuration #2 the systematic errors of the target polarization could be studied in detail and reduced to a level below 2%. Tilting the target in the vertical plane in contrast with the horizontal plane of configuration #1, allowed to reduce the contribution from a sizable horizontal beam polarization, to the measured asymmetry. Configuration #3 was implemented to reduce the systematic error to <1%.

Efficient running in configuration #3 requires a new cryo-supply line for the superconducting magnet. Since the g2p experiment scheduled to run in 2011 requires a modest polarization accuracy, configuration #2 will be restored in the beginning of 2011. A summary of the Møller polarimeter features in configuration #2 is presented bellow.

2.2.2 General description

The target foils are tilted at an angle of 20.5° to a vertical plane and magnetized in a magnetic field of about 350 G along the beam. The target polarization was derived from the foil magnetization measurements. A photo image of the Møller target chamber is presented in Fig. 4.

The Møller scattering events are detected with a magnetic spectrometer (see Fig. 5) consisting of a sequence of three quadrupole magnets and a dipole magnet. The electrons scattered in a plane close to the horizontal plane are transported by the quadrupole magnets to the entrance of the dipole which deflects the electrons down, towards the detector. The optics of the spectrometer is optimized in order to maximize the acceptance for pairs scattered at about 90° in the CM. The acceptance depends on the beam energy. The typical range for the accepted polar and azimuthal angles in CM is $75° < \theta_{\mathrm{CM}} < 105°$ and $-6° < \phi_{\mathrm{CM}} < 6°$. The non-scattered electron beam passes through a 4 cm diameter hole in a vertical steel plate 6 cm thick, which is positioned at the central plane of the dipole and provides a magnetic shielding for the beam. The plate, combined with the magnet's poles, forms two 4 cm wide gaps, which serve as θ_{CM} angle collimators for the scattered electrons. Two additional lead collimators restrict the ϕ_{CM} angle range. The polarimeter can be used at beam energies from 0.8 to 6 GeV, by setting the appropriate fields in the magnets. The lower limit is defined by a drop of the acceptance at lower energies, while the upper limit is determined mainly by the magnetic shielding of the beam inside the dipole.

The detector consists of total absorption calorimeter modules, split into two arms in order to detect two scattered electrons in coincidence. There are two aperture plastic scintillator detectors at the face of the calorimeter. The beam helicity driven asymmetry of the coincidence counting rate (typically about 10^5 Hz) is used to derive the beam polarization. Additionally, about 300 Hz of "minimum bias" events containing the

---

[1] We use a right-handed frame with Z pointing in the beam direction, and Y pointing vertically up.

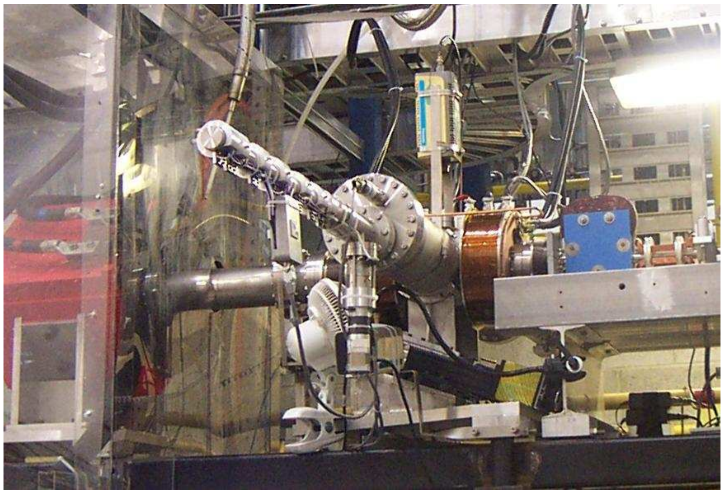

Figure 4: Photo of the target chamber of the Møller polarimeter in Hall A.

amplitudes and timings of all signals involved are recorded with a soft trigger from one of the arms. These data are used for various checks and tuning, and for studies of the non–Møller background. The estimated background level of the coincidence rate is below 1 %.

2.2.3 The Polarized Target

In configuration #2 a set of ferromagnetic target foils (see Table 1) (7-30 μm thick, 30 mm wide and 160 mm long) tilted at 20.5° to the direction of the electron beam, is used. The foils are made either of pure iron or of Supermendure (49% Fe, 49% Co, 2% V).

Table 1: Target foils. (SM - Supermendure)

Position	6(right limit)	5	4	3	2	1(old target)	0(left limit)
Material	empty	SM	Fe	Fe	SM	SM	Al
Thickness μ		6.8	9.3	14.3	29.4	13.0	16.5

The target holder design[2] is shown in Fig. 6. The holder can move the targets across the beam in two projections: transversely - along X, and longitudinally - along the longer sides of the foils (a line in the YZ-plane, at 20.5° to Z). The goal is to study the observed effects of non-uniformity of the target magnetic flux, measured by a small pickup coil at different locations along the foil.

The target chamber is equipped with flanges and bellows to connect to the upstream and downstream parts of the beam pipe. The Helmholtz coils are attached to the chamber.

A slide is installed inside the target chamber for the transverse target motion. The target foils are attached to a frame with their centers about 89 mm apart. The frame is movable along the slide (see the top of Fig. 6 and Fig. 7) with the help of a Rack and Pinion mechanism[3] installed on the left (looking downstream the beam) side of the target chamber. The frame position is measured with a position transducer. Additionally,

---

[2] The target holder was designed and assembled by V. Gorbenko.

[3] Professional Rack and Pinion (PRP) from UHV is used. The PRP is coupled to an MD25 MagicDrive.

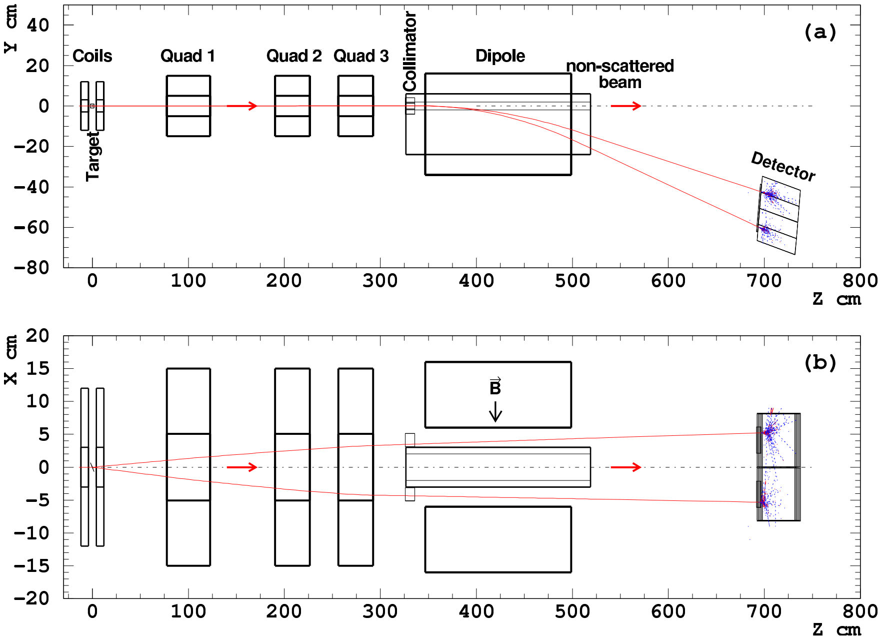

Figure 5: Lay-out of the Møller polarimeter, (a) presents the side view while (b) presents the top view. The trajectories displayed belong to a simulated event of Møller scattering at $\theta_{\text{CM}} = 80°$ and $\phi_{\text{CM}} = 0°$, at a beam energy of 4 GeV.

the center positions of all five targets are marked by five position switches. Two limit switches define the motion range of about 440 mm.

The target chamber is installed on another slide[4], tilted at about 20° to the beam direction, similar to the target foils. This slide provides the longitudinal target motion across the beam, with a full range of 55 mm. The longitudinal position (along the slide) is measured by a transducer. Three switches mark the following positions:

1. top Limit (+30 mm) - the beam would hit the upstream-bottom part of the target foil;
2. center (0 mm) - the beam would hit the the target center,
3. bottom Limit (-25 mm) - the beam would hit the downstream-top part of the target foil;

The motion mechanisms use stepping motors operated in the micro-stepping mode. The motion control system is located inside Hall A, close to the power supplies for the Møller quadrupole magnets.

Additionally to the limit switches, the system is equipped with mechanical stoppers preventing it from moving beyond the allowed range. In the range allowed no element of the target frame or other thick piece of material can obstruct the beam. Since only the targets - thin foils - can be moved in the beam, there is no need to turn the beam off while moving the targets.

2.2.4 The Target Polarization Measurement

Typically, the dominant systematic error of Møller polarimetry is the target polarization uncertainty. For ferromagnetic materials, the electron polarization and the resulting magnetization come from the atomic *d*-shell, which is not fully populated. However, the present theory of ferromagnetics does not allow to calculate accurately the polarization or magnetization at saturation. In iron, about 2 electrons per atom are polarized, providing an average electron polarization of about 8%.

---

[4] BiSlide from Velmex, Inc.

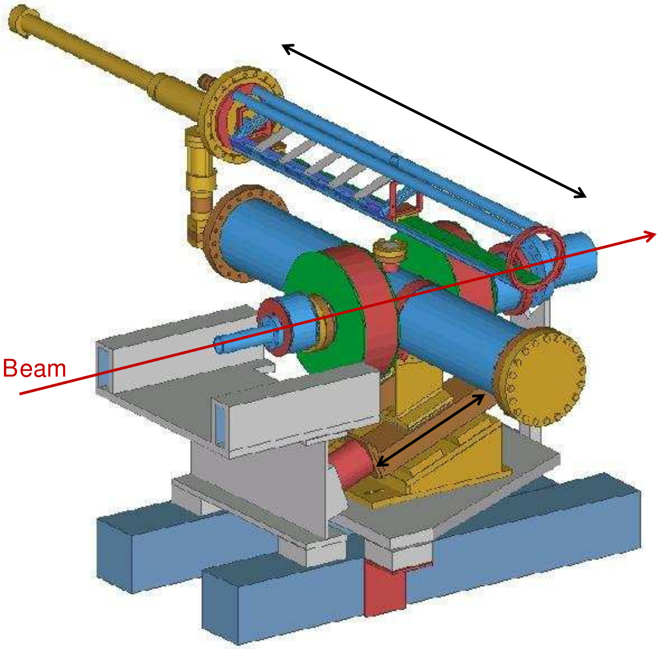

Figure 6: The target holder design. The direction of electron beam direction and of the target motion in two projections is shown.

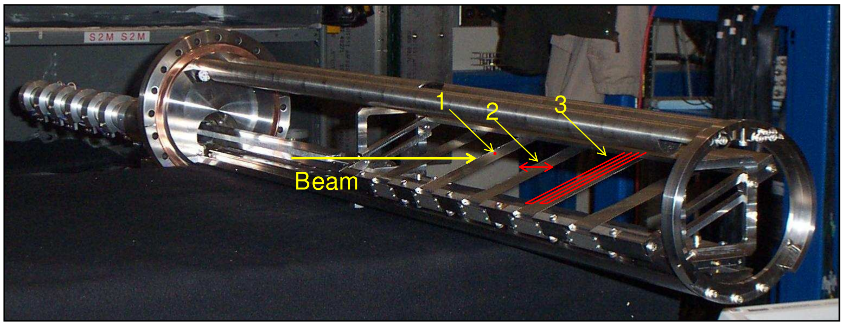

Figure 7: The polarized electron target holder in assembly. The electron beam direction and types of the beam polarization measurement are shown. 1 - static measurement, 2 - transverse target scan, 3 - double target scan.

The electron polarization P^t can be derived from the value of the magnetization M:

$$P^t = \frac{(g\prime - 1)}{g\prime} \cdot \frac{g_e}{(g_e - 1)} \cdot \frac{M}{N_e \mu_B} \qquad (1)$$

where g_e=2.00232 is the g-factor of a free electron, $g\prime$ is the gyromagnetic ratio for the target material (1.919±0.002 for iron),N_e is the electron density (derived from the density ρ and the average atomic properties Z, A through $N_e = \rho A v \cdot Z/A$), $\mu_B = 9.2740 \times 10^{-24}$ J $\cdot$ T^{-1} is the Bohr magneton. The magnetization must be measured. The magnetic inductance in material B is related to the external field H and the magnetization through: $B = \mu_\circ(H + M)$.

A long and narrow ferromagnetic foil strip can be magnetized in relatively low external magnetic fields directed along the long side of the foil strip. Still, in fields of $\mu_\circ H < 0.04$ T thin foils used for Møller polarimetry do not reach full magnetic saturation by several percents, depending on the material purity and the quality of annealing. Therefore, one can not use the existing accurate data on magnetization at saturation, but rather has to measure the magnetization of the foils used, in the proper field range.

The standard way to measure the magnetization of the thin rectangular foils used for Møller polarimetry was as follows:

1. provide a small pick-up coil around the narrower cross section of the foil;
2. flip the external magnetic field directed along the longer side of the foil in order to flip the foil magnetization;
3. measure the change of the magnetic flux through the pick-up coil by integrating the *emf* value on the coil $\int \varepsilon(t)dt = \Delta\Phi = \mu_\circ \Delta M \cdot S_{foil} + \mu_\circ \Delta H \cdot S_{coil} + \Delta B_{stray} \cdot S_{coil}$, where H is the external field, B_{stray} is the stray (return) field from the foil, while S_{coil}, S_{foil} are the cross sections of the coil and the foil;
4. measure the empty-coil contribution $\mu_\circ \Delta H \cdot S_{coil}$ by making a similar measurement without the foil.

The magnetization is derived from the magnetization flip as $M = \Delta M/2$. It is difficult to measure the foil thickness with a sub-percent accuracy, and, therefore, to measure directly the cross section S_{foil}. Typically, the foil weight W and the length l are measured: $W = \rho \cdot l \cdot \overline{S_{foil}}$. Here $\overline{S_{foil}}$ is the average cross section along the length. The foil width can be made uniform along the length to a 0.3% level, but the thickness of thin foils may vary by more than 10%. Even in the ideal case of uniform magnetization, the magnetic flux should be measured at multiple positions along the full length of the foil, in order to normalize properly to the average foil cross section.

The annealing procedure and a possible mechanical damage of the ferromagnetic target structure can lead to an inhomogeneous magnetic permeability throughout the foil length. Hence, the change of the magnetization value along the target should be carefully investigated.

Several uncertainties associated with the method described increase the final systematic error:

– the empty-coil contribution to the flux is ∼10 times larger than the magnetization contribution;

– multiple measurements along the foil are time consuming, which limits the potential to study the relevant systematic error.

In order to overcome these problems a different method of magnetization measurements was applied[5]. The external field stays the same during the measurement, but the foil is moved through the pickup coil, changing the magnetic flux and creating an *emf*. The pickup coil is placed at the center of the magnetic system consisting of two Helmholtz coils (see Fig. 8). A foil piece (say, $300 \times 30 \times 0.01$ mm^3) is kept in a long plastic envelope placed in a slit of the pickup coil and connected to a stepper motor. The stepper motor allows moving the plastic envelope with the foil through the pickup coil in both forward and backward direction, at a selected speed. The *emf* produced on the pickup coil is measured with a 16-bit ADC with a sampling rate of 10 kHz. Two big and sharp spikes in the *emf* define the moments when the foil's edges cross the pickup coil. A special computer program synchronizes the motion and the data acquisition. Starting the DAQ before the motion allows to identify a 60 Hz noise pattern for subsequent subtraction.

---

[5] A new method of foil magnetization measurements was developed by V.Gorbenko.

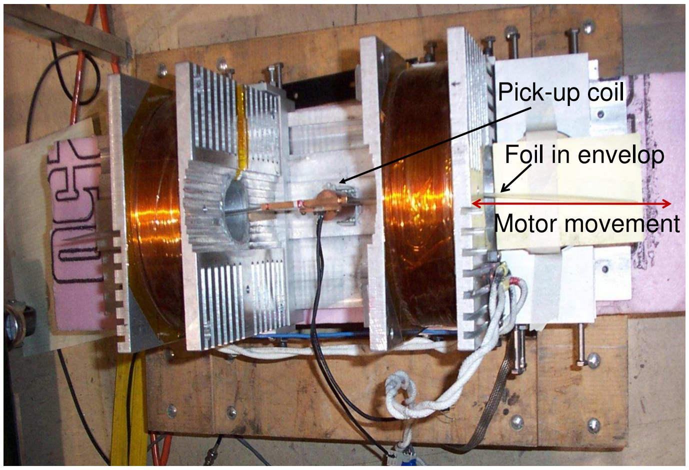

Figure 8: The magnetic stand for magnetization measurements of the ferromagnetic foils. The motor (not shown) is located on the right side.

This method allows to measure the magnetic flux smoothly along the foil length. The measured flux allows to calculate the average magnetization in the area covered by the pickup coil. No empty-coil subtraction is needed, since the external field stays constant.

Two magnetic field configurations were used, one with a pseudo-Helmholtz geometry with a space between the coils of 15 cm and a field in the center of about 0.034 T (close to the field used in the polarimeter). In the other geometry the coils were installed close to each other, resulting in a field of about 0.1 T at the center.

The polarization profile for one of the Møller polarimeter targets is shown in Fig. 9. The variations along the foil (±0.3%) might be due to variations in the target thickness. In this case the foil polarization is in fact constant and equal to the average value along the foil. The variations may also reflect a real polarization variation, due to variations of chemical and mechanical properties along the foil. Measuring the event rate and the Møller asymmetry in a two-dimensional scanning of the target across the beam allows to constrain these two contributions and reduce the associated systematic error.

2.2.5 The Beam Polarization Measurement

The electron beam asymmetry measured by the Møller polarimeter is defined as:

$$A = \frac{N_{\uparrow\uparrow} - N_{\uparrow\downarrow}}{N_{\uparrow\uparrow} + N_{\uparrow\downarrow}} = A_{zz} \cdot P^t_z \cdot P^b_z \tag{2}$$

where A_{zz} is the Møller polarimeter analyzing power, P^t_z the longitudinal component of the target polarization, P^b_z the longitudinal component of the beam polarization and $N_{\uparrow\uparrow}$ and $N_{\uparrow\downarrow}$ - the measured yields with the beam polarization direction along and opposite to the beam direction.

The beam polarization value is calculated from:

$$P^b_z = \frac{A}{A_{zz} P^t_z}. \tag{3}$$

The Møller polarimeter analyzing power is calculated using a GEANT simulation. The target polarization is measured on the magnetic stand.

Three different types of beam polarization measurements were used to study the systematics of the polarized electron targets (see Fig. 7) :

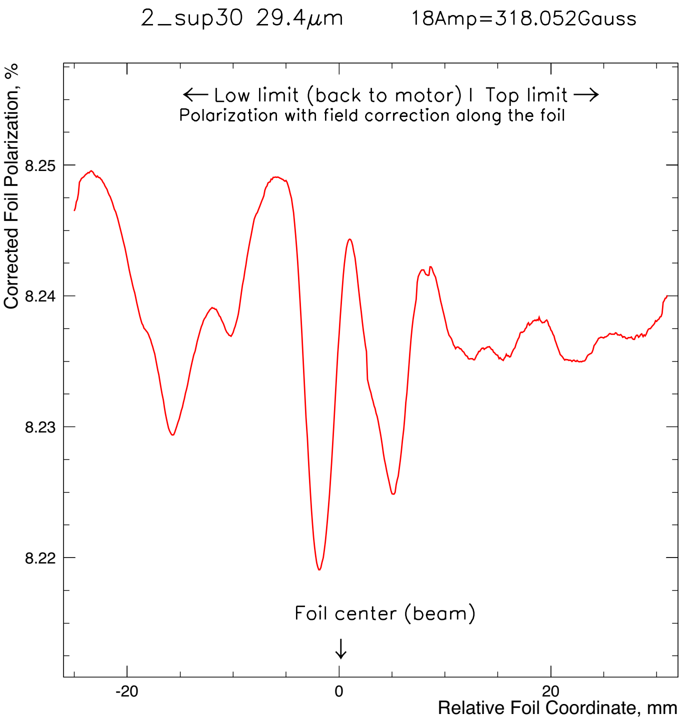

Figure 9: Polarization profile for Target 2 (Supermendure 29.4 μm thick). The target polarization is corrected for the magnetic field geometry in the target area.

1. Static. This is the most often used Møller measurement where the target is not moved with respect to the beam during the measurement. In this case, the target polarization measured on the magnetic stand at the point of the target and beam crossing is used.
2. Transverse target scan. The target is moved horizontally across the beam. With the Hall A fast raster turned on, the beam width (taking into account the 20.5° foil tilt) is about 1.5-2 mm. This is close to the magnetic stand pick-up coil width.
3. Double scan. In this two-dimensional target scan the target polarization value measured at each target coordinate on the magnetic stand (see Fig. 9) is used. A long time is needed to measure the whole target surface with good statistics at each point.

The results of the beam polarization measurement with different target foils provide an additional information about the target polarization systematic error. A summary is given in Tab. 2.

2.2.6 The Møller Polarimeter Systematic Error

A typical beam current for a Møller measurement is 0.3-1.0 μA. At these low currents the Hall A fast energy feedback can not be used. Usually, the Hall C BSY fast energy feedback is used during Hall A Møller measurements. In 2009 there were long periods when Hall C was not running. In that case only the ARC2 slow energy feedback could be used. Occasionally the beam energy during the Møller measurement would fluctuate and differ from its value during the running experiment. For high beam energies and large transverse components of the beam polarization due to precession, these energy variations lead to sizable variations of the longitudinal beam polarization in the hall (see for more details ref. [1]). An example of the beam energy fluctuation and its influence on the measured beam polarization is shown in Fig. 10. This difference has to be calculated and corrected run-by-run. Sometimes the fluctuations became very large or very noisy, prohibiting a precise correction. An additional systematic error was assigned to the beam polarization measurements in these conditions.

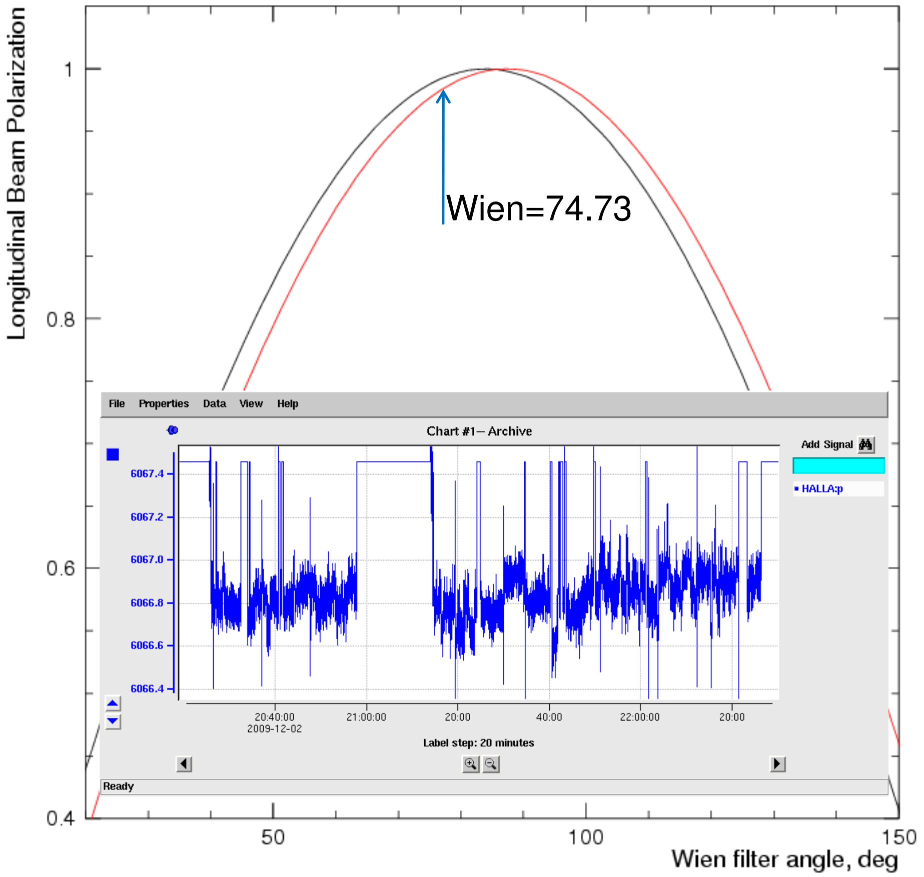

Figure 10: Correction of the measured beam polarization for beam energy fluctuations. The PDVIS energy on the strip chart was 6067.46 MeV (0.987% of the maximal longitudinal polarization at a 74.73° Wien angle). The beam energy for the Møller measurements is 6066.8 MeV (0.976% of the maximal longitudinal polarization at a 74.73° Wien angle). The beam polarization correction thus is 1.1%.

Table 2: Systematic error of the target polarization.

Variable	Error [%]
Magnetic Stand	0.23
Double Scan (left vs. right)	0.3
Type 1 vs Type2	0.7
Type1 vs Type 3	1.0
Different targets	0.5
Target angle	0.3
Others	0.5
Total	1.5

The summary of the Møller polarimeter systematic errors for the period 2005-2009 is presented in Tab. 3.

Table 3: Systematic error of the Hall A Møller polarimeter for 2005-2009.

Variable	Error [%]
Target polarization	1.5
Analyzing Power	0.3
Levchuk-effect	0.2
Dead time	0.3
Background	0.3
Others	0.5
Energy Fluctuation *	1.0
Total	1.7
Total*	2.0

References

[1] D. W. Higinbotham, arXiv:0901.4484v1, JLAB-PHY-09-942 (2009).

2.3 Fifteen nanosecond coincidence time between HRSs

Eric Jensen, Albert Shahinyan, Bogdan Wojtsekhowski

Operation of experiments often requires a minimum DAQ dead time, for which we would like to reduce the coincidence time window between the signal of the two arms. In the recent APEX test run we demonstrated that a fifteen ns coincidence time window is feasible. The coincidence time between the two arms is spread due to the different path lengths through the spectrometers as well as to misalignment of the various trigger counters. In the test run we aligned the timing of 32 trigger counters (16 per arm) by using cable delays (0.5-7 ns) inserted at the output of the fastest tubes. The procedure used the S0 counter as a reference and cosmic rays for alignment. We also aligned the 20 phototubes of the gas Cherenkov detectors by using production data (electrons/positrons). The figures demonstrate the quality of the alignment and the achieved coincidence time spectrum. We observe that the amount of delay needed correlates well with the expected propagation time in the phototube and the variation of high voltage settings.

Timing Alignment in Hardware

- Run at high rates, small timing gate is important
- Must align timing of the trigger detectors
  - S0 counter as a reference
  - Inserted 1–5 ns delay cables

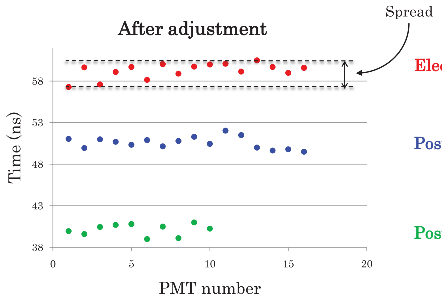

	σ	Spread
Electron S2m	0.9 ns	3.2 ns
Positron S2m	0.7 ns	2.6 ns
Positron GC	0.7 ns	2 ns

Coincidence Timing

Time difference between
Electron S2m and trigger

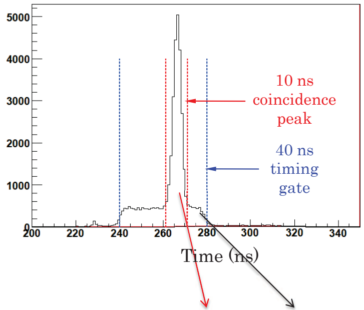

Under test run conditions: signal / background is ~ 5/1
For proposed experiment: signal / background expected to be ~ 1/4
which improves in off-line to ~ 12/1

3 Summaries of Experimental Activities

3.1 E03-101

Hard Photodisintegration of a Proton Pair

R. Gilman and E. Piasetzky, spokespersons,
D.W. Higinbotham, S. Strauch and the Hall A Collaboration,
contributed by I. Pomerantz

3.1.1 ^{3}He(γ,pp)n

Extensive studies of high-energy deuteron photodisintegration over the past two decades have probed the limits of meson-baryon descriptions of nuclei and reactions [1, 2, 3, 4, 5], and the effects of the underlying quark-gluon degrees of freedom. At low energies, up through the region of Δ resonance excitation, photodisintegration of the deuteron is well understood, although certain detailed problems remain [6, 7, 8, 9]. Above ∼1 GeV, deuteron photodisintegration cross sections have been shown to follow the constituent-counting rules [10, 11, 12, 13, 14], which have been derived from dimensional analysis, QCD and AdS/CFT correspondence [13, 15, 16].

We define a hard photodisintegration of a nucleon pair as a process in which a high-energy photon is absorbed by a nucleon pair and as a result the pair is disintegrated by emitting two nucleons with large transverse momenta, greater than about 1 GeV/c. As defined, in this process the Mandelstam parameters s and t (the square of the total energy in the c.m. frame, and the four-momentum transfer from the photon to the nucleon), are large.

In an attempt to more clearly identify the underlying dynamics at play in high-energy photodisintegration, E03-101 measured the hard photodisintegration of two protons, using ^{3}He. The basic idea is that theoretical models should be able to predict the relative size of *pp* versus *pn* disintegration [17]. Also, if the *pp* and *pn* disintegrations are related to the corresponding *pp* and *pn* elastic scattering via hard re-scattering [19], deviations from power scaling in the elastic scattering should be reflected in corresponding differences in the photodisintegration processes.

Experiment E03-101 ran in Hall A during the summer of 2007 and measured the cross section of the photodisintegration of a proton pair in ^{3}He at $\theta_{c.m.} = 90°$ for photon energies in the range of 0.8 - 4.7 GeV [20]. Figure 11 shows the $\gamma + \mathrm{d} \rightarrow p + n$ and $\gamma + {}^3\mathrm{He} \rightarrow p + p + n$ cross section at $\theta_{c.m.} = 90°$ scaled by s^{11}. The ^{3}He(γ,*pp*)n events were selected with $p_n < 100$ MeV/c. The cross section is compared to theoretical models, discussed below, that produced predictions for the photodisintegration of both *pn* and *pp* pairs [17].

Our new data [18], along with previous low-energy data, indicate that the ^{3}He two-proton disintegration can be divided into three energy regions. At *low* photon energies (below $E_\gamma \approx 0.5$ GeV), the dynamics of $\theta_{c.m.} = 90°$ proton-pair break-up is governed by hadron and meson degrees of freedom and the cross section has a large three-body component [21].

In a *transition* region (1 GeV $< E_\gamma <$ 2.2 GeV) the scaled cross section for deuteron (*pn* pairs) break-up is flat while for *pp* pairs a significant structure is observed. This structure may be the result of resonances in the γN or γNN systems. The energy dependence in the transition region more closely resembles the energy behavior of the photo-induced pion production [22, 23, 24] than that of deuteron photo-disintegration. It has been suggested that the structure might result from a meson photo-produced on a proton and then absorbed on a *pn* pair [25].

In the *scaling* region the cross section for both *pn* and *pp* break-up scales in agreement with the constituent counting rule [13, 15, 16]. For proton-pair break-up, the onset of the scaling is at $E_\gamma \approx 2.2$ GeV, while for *pn* pairs scaling commences at $E_\gamma \approx 1$ GeV [5]. The scaling in the ^{3}He case indicates that in this regime the two-body process is dominant. It further suggests (in a relatively model-independent way) that the quarks are the relevant degrees of freedom that govern the dynamics. In a hadronic picture, two-body/one-step processes are strongly suppressed since no charged pion can be exchanged between the protons.

The reduced nuclear amplitude (RNA) formalism after normalization to the deuteron data [17] yields cross sections that are about 200 times larger than the present data. The quark-gluon string model (QGS) [26, 27], as estimated in [17], predicts cross sections about a factor of 5 larger than measured. The QCD hard re-scattering model (HRM) [28] allows an absolute calculation of the cross sections for both *pn* and *pp* pair photodisintegration from nucleon-nucleon measured cross sections without adjustable parameters. It reproduces reasonably well the deuteron data and the proton pair cross section. The HRM model predicts a deviation from the scaling of the cross section that the data are not accurate enough to either confirm or reject.

An explanation for the low magnitude of the scaled cross section of proton-pair break-up is given in the HRM [19] by a cancellation of the opposite sign of the NN helicity amplitudes ϕ_3 and ϕ_4 in the pp break-up [6]. The energy dependence predicted by the HRM in the scaling region agrees well with the data. Therefore, hard re-scattering is a plausible explanation for the origin of the large transverse momenta. Models that hold compact NN pairs in the initial state to be the reason for the large transverse momenta [29] would have to assume either a fairly low abundance of pp pairs within the ^{3}He wave function or the same type of nuclear amplitude cancellation in order to explain the low magnitude of the pp break-up scaled cross section.

Another possible explanation for the cross-section magnitude may lie in tensor correlations [30, 31, 32]. These nucleon-nucleon correlations cause the ratio of pp to np pairs to be $\sim$5% in the relative momentum range of 300-600 MeV/c for both high-energy electron and proton scattering [33, 34, 35]. Starting with such a pair and final-state re-scattering might lead to the observed relative transverse momentum and would explain the relatively small cross sections.

3.1.2 ^{3}He(γ,pd)

E03-101 also extended the search for scaling to an $A = 3$ system, using the $\gamma^3\text{He} \to pd$ reaction. This is the first measurement of this reaction in the GeV energy region. As previous measurements have only involved $A = 1$ or 2, the expected scaling degree of $d\sigma/dt \propto s^{-17}$ is higher than any previous observation.

E03-101 was a measurement of the $\theta_{c.m.} = 90^\circ$ energy dependence of the $^3\text{He}(\gamma, pp)n_{spectator}$ reaction [18]. At an incident energy of 1.656 GeV we also took data at two kinematical set-ups which did not match the $\theta_{c.m.} = 90^\circ$ conditions. In these two kinematics we could identify two-body photodisintegration of the ^{3}He into a proton and a deuteron at angles corresponding to $\theta_{p\ c.m.} = 85^\circ$. This reaction has also been measured by the CLAS/Hall B collaboration and their data are currently being analyzed.

Figure 12 shows the resulting cross sections compared to previously published data [36] for s>10 GeV^2. Results from E03-101 and CLAS are preliminary. The scaled cross sections are clearly observed to be constant. In the range of the new data, $E_\gamma = 0.4 - 1.3$ GeV or $s = 10 - 15$ GeV^2, the cross section falls by two orders of magnitude. The fall-off of our data is fit as $s^{-18\pm1}$, which is consistent with the CCR prediction of $n = -17$. This is the first observation of a high-energy cross-section scaling consistent with the CCR for an $A > 2$ system.

The scaled cross section of $\sim$30 Gb$\cdot$GeV^{32} corresponds to an invariant cross section of $d\sigma/dt \approx 0.4$ nb/GeV^2 for $E_\gamma \approx 1.3$ GeV. The corresponding cross section for $\gamma d \to pn$ at this energy is about 30 nb/GeV^2, about two orders of magnitude larger, while the scaled cross section for $\gamma^3\text{He} \to pp + n_{spectator}$ at this energy is about 13 nb/GeV^2, about 30 times larger.

If one adopts the view that large momentum transfer reactions select initial states in which all the quarks and nucleons are close together, it is much more likely that there is a short-range, and thus high-momentum, pn pair than a pp one. This is what has been found in recent studies for nucleons above the Fermi surface that have momenta of several hundred MeV/c [35, 34]. Furthermore, in ^{3}He there is nearly as large a probability for a short-range pd pair as for a pp pair.

If the reaction dynamics rely instead on rescattering, it appears that hard pn rescattering is more likely than hard pp rescattering – which is known to be the case from cancellations in the pp amplitude [19]– and that hard pd rescattering is also suppressed, presumably due to the likelihood of breaking up the deuteron in a hard scattering and the small probability of a pick-up reaction that create a deuteron from a scattered proton or neutron.

The E03-101 and CLAS collaborations are currently working on a joint publication of these results.

---

[6] ϕ_3 and ϕ_4 are the NN elastic scattering helicity amplitudes that connect zero helicity in the initial states to zero helicity in the final state.ϕ_3 does it without helicity exchange. ϕ_4 exchanges helicity between the scattered nucleons. This cancellation of ϕ_3 and ϕ_4 was not recognized in [17].

References

[1] E. Schulte *et al.*, Phys. Rev. Lett. 87, 102302 (2001).

[2] J. Napolitano *et al.*, Phys. Rev. Lett. 61, 2530 (1988); S.J. Freedman *et al.*, Phys. Rev. C 48, 1864 (1993).

[3] J.E. Belz *et al.*, Phys. Rev. Lett. 74, 646 (1995).

[4] C. Bochna *et al.*, Phys. Rev. Lett. 81, 4576 (1998).

[5] E. Schulte *et al.*, Phys. Rev. C 66, 042201R (2002).

[6] H. Arenhoevel, E. M. Darwish, A. Fix, and M. Schwamb, Mod. Phys. Lett. A18, 190 (2003),nucl-th/0209083.

[7] M. Schwamb and H. Arenhovel, Nucl. Phys. A696, 556 (2001), nucl-th/0105033.

[8] M. Schwamb and H. Arenhovel, Nucl. Phys. A690, 647 (2001), nucl-th/9912017.

[9] R. Schiavilla, Phys. Rev. C72, 034001 (2005), nucl-th/0505066.

[10] P. Rossi et al., Phys. Rev. Lett. 94, 012301 (2005), hep-ph/0405207.

[11] S. J. Brodsky and B. T. Chertok, Phys. Rev. Lett. 37, 269 (1976).

[12] S. J. Brodsky and B. T. Chertok, Phys. Rev. D 14, 3003 (1976).

[13] S. J. Brodsky and G. R. Farrar, Phys. Rev. Lett. 31, 1153 (1973).

[14] V. A. Matveev, R. M. Muradian, and A. N. Tavkhelidze, Nuovo Cim. Lett. 7, 719 (1973).

[15] G. P. Lepage and S. J. Brodsky, Phys. Rev. D22, 2157 (1980).

[16] J. Polchinski and M. J. Strassler, Phys. Rev. Lett. 88, 031601 (2002), hep-th/0109174.

[17] S. J. Brodsky et al., Phys. Lett. B578, 69 (2004), nucl-th/0305068.

[18] I. Pomerantz et al., Phys. Lett. B684, 106 (2010).

[19] M. M. Sargsian and C. Granados, Phys. Rev. C80, 014612 (2009), 0812.4590.

[20] E03-101, http://hallaweb.jlab.org/experiment/E03-101.

[21] J. M. Laget, Phys. Lett. B151 (1985) 325.

[22] H. J. Besch, F. Krautschneider, K. P. Sternemann, W. Vollrath, Z. Phys. C16 (1982) 16.

[23] P. Benz, et al., Nucl. Phys. B65 (1973) 158209.

[24] L. Y. Zhu, et al., Phys. Rev. C71 (2005) 044603.

[25] J. M. Laget, private communication.

[26] V. Y. Grishina et al., Eur. Phys. J. A10, 355 (2001), hep-ph/0101129.

[27] V. Y. Grishina et al., Eur. Phys. J. A18, 207 (2003), nucl-th/0209076.

[28] L. L. Frankfurt, G. A. Miller, M. M. Sargsian, and M. I. Strikman, Phys. Rev. Lett. 84, 3045 (2000), hep-ph/9904222.

[29] S. J. Brodsky, J. R. Hiller, Phys. Rev. C28 (1983) 475.

[30] M. M. Sargsian, T. V. Abrahamyan, M. I. Strikman, L. L. Frankfurt, Phys. Rev. C71 (2005) 044615.

[31] R. Schiavilla, R. B. Wiringa, S. C. Pieper, J. Carlson, Phys. Rev. Lett. 98 (2007) 132501.

[32] M. Alvioli, C. Ciofi degli Atti, H. Morita, Phys. Rev. Lett. 100 (2008) 162503.

[33] E. Piasetzky, M. Sargsian, L. Frankfurt, M. Strikman, J. W. Watson, Phys. Rev. Lett. 97 (2006) 162504.

[34] R. Shneor, et al., Phys. Rev. Lett. 99 (2007) 072501.

[35] R. Subedi, et al., Science 320 (2008) 14761478.

[36] V. Isbert et al., Nucl. Phys. A578, 525 (1994).

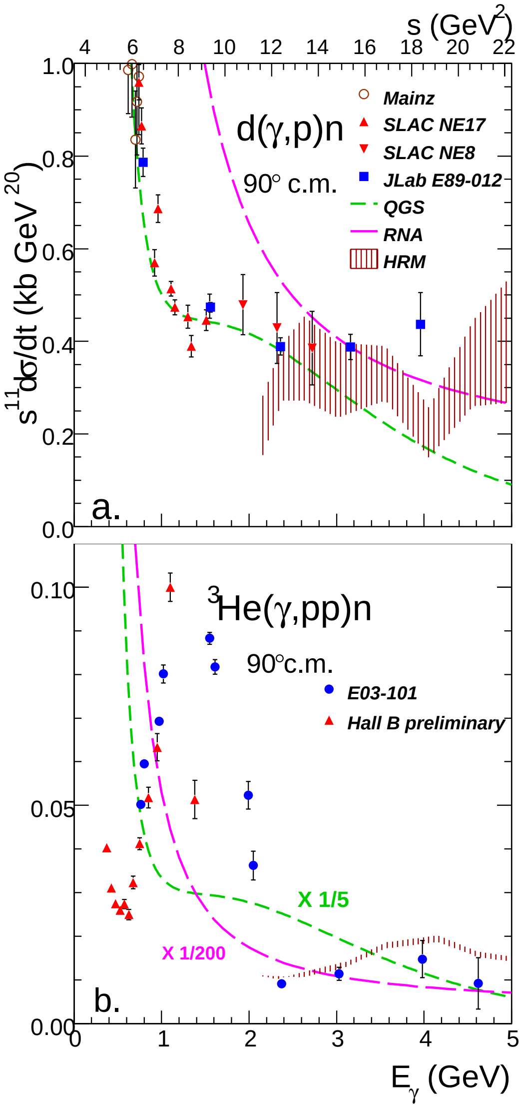

Figure 11: The d(γ,p)n (a) and ^{3}He(γ,pp)n (b) invariant cross section scaled by s^{11}. ^{3}He(γ,pp)n events were selected with $p_n < 100$ MeV/c. Up to 2.1 GeV, the photon energy bins are 70 MeV, and above it 140 MeV. Model predictions are taken from [17, 19]. In (b), RNA is divided by a factor of 200 and QGS by a factor of 5 to be shown on this scale. Error bars represent statistical uncertainties.

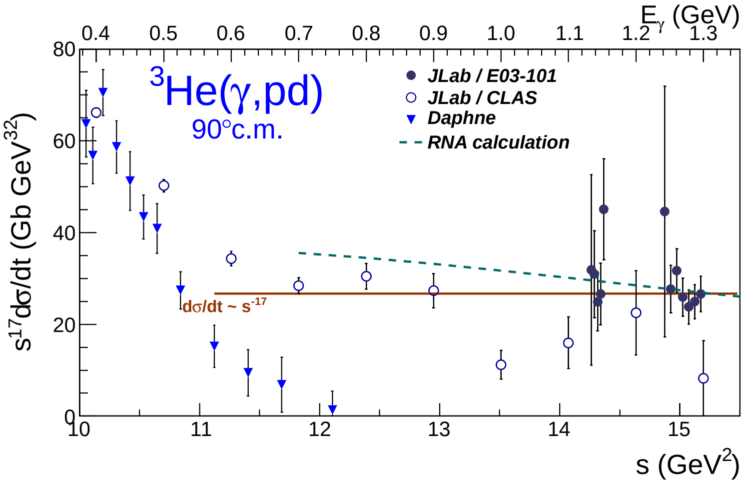

Figure 12: The invariant cross section $d\sigma/dt$ multiplied by s^{17} to remove the expected energy dependence. Results from E03-101 and CLAS are preliminary. The DAPHNE data are taken from [36].The horizontal line indicates the scaling predicted by the CCR.

3.2 C12-10-009

An Electron Fixed-Target Experiment to Search for a New Vector Boson A' Decaying to e^+e^-

Rouven Essig, Philip Schuster, Natalia Toro, Bogdan Wojtsekhowski
and the Hall A Collaboration

3.2.1 Introduction

The development of the Standard Model of particle interactions is the culmination of a century of searches and analyses with fixed-target and colliding-beam experiments. Interactions with new forces beyond the Standard Model are currently limited by well-tested gauge symmetries to a handful of possibilities. One of the few remaining ways for interactions with new sub-GeV vector-like forces to arise is for charged particles to acquire millicharges, ϵe, under these forces. This occurs through a simple and generic mechanism proposed by Holdom [1], in which a new vector particle A'_μ mixes via quantum loops with the Standard Model photon. MeV–GeV masses for the A' gauge boson are particularly well-motivated in this context. Such sub-GeV forces are a common feature of extensions of the Standard Model, but existing constraints are surprisingly weak, with limits at $\epsilon e \lesssim (0.3 - 1) \times 10^{-2} e$.

Fixed-target experiments with high-intensity electron beams and existing precision spectrometers are ideally suited to explore sub-GeV forces by probing reactions in which a new A' vector particle is produced by radiation off an electron beam [2, 3]. The A' can decay to an electron and positron pair and appears as a narrow resonance of small magnitude in the invariant mass spectrum. In [2], several fixed-target experimental strategies were outlined to search for new sub-GeV vector interactions.

The C12-10-009 experiment is a concrete plan for an A' search using the CEBAF accelerator and the High Resolution Spectrometers (HRS) in Hall A [4]. This experiment, the *A' Experiment* (APEX), can probe charged particle couplings with new forces as small as $3 \times 10^{-4} e$ and masses between 65 MeV and 525 MeV — an improvement by more than two orders of magnitude in cross section sensitivity over all previous experiments.

Fixed-target experiments of this form are particularly timely in light of a series of recent anomalies from terrestrial, balloon-borne, and satellite experiments that suggest that dark matter interacts with Standard Model particles. Much of this data hints that dark matter is directly charged under a new force mediated by an A' and not described by the Standard Model. Theoretical as well as phenomenological expectations suggest an A' mass $m_{A'} \lesssim 1\,\mathrm{GeV}$ and $\epsilon e \lesssim 10^{-2} e$.

3.2.2 Expected reach and impact

APEX will be sensitive to new gauge bosons with couplings as small as $\epsilon^2 \equiv \alpha'/\alpha \sim 9 \times 10^{-8}$ and masses in the range $65 - 525\,\mathrm{MeV}$ (here α (α') is the coupling of the photon (A') to electrically charged matter). This is about a factor of $3 - 35$ times lower in ϵ than existing constraints (which assume that the A' couples also to muons), and corresponds to $\sim 10 - 1000$ times smaller cross sections.

The precise mass range probed by this type of experiment can be varied by changing the spectrometer angular settings and/or the beam energies, see the APEX plan in Fig. 13. The parameter range probed by APEX is interesting for several reasons. This region of mass and coupling is compatible with A''s explaining the annual modulation signal seen by the dark matter direct detection experiment DAMA/LIBRA, and also with dark matter annihilating into A's, which explains a myriad of recent cosmic-ray and other astrophysical anomalies. In addition, and independently of any connection to dark matter, the APEX experiment would be the first to probe A's of mass $\gtrsim 50\,\mathrm{MeV}$ with gauge kinetic mixing below $\epsilon \sim 10^{-3}$, the range most compatible if the Standard Model hypercharge gauge force is part of a Grand Unified Theory.

The importance for fundamental physics of precision searching for new forces near the GeV scale cannot be overstated.

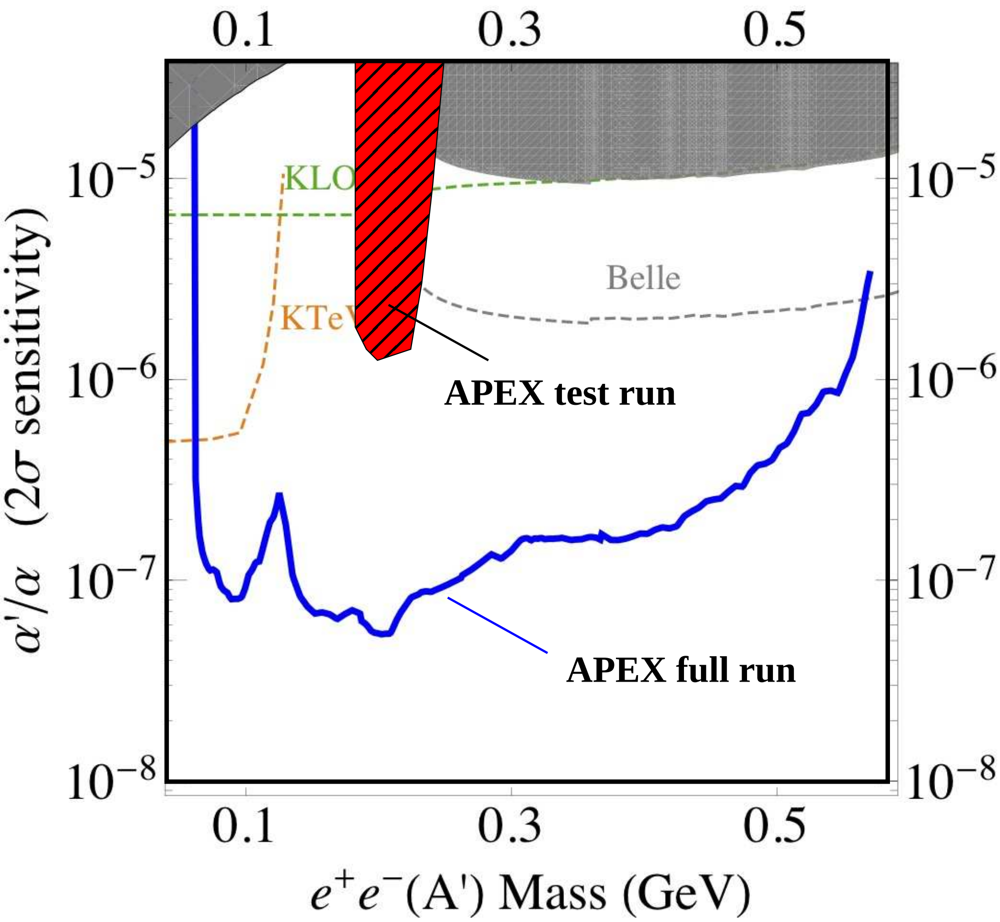

Figure 13: The reach of the APEX experiment (blue contour), the APEX test run (red hatched region) and existing constraints (gray shaded regions).

3.2.3 Concept

In the APEX experiment, we are interested in collecting as many true e^+e^- coincidence events as possible, since the A' is expected to decay to e^+e^- pairs. A large background of such true coincidence events is expected from Standard Model QED Bethe-Heitler and radiative trident processes, but the A' would appear as a narrow spike on top of this large Standard Model background. A further background is caused by accidental e^+e^- coincidences from two distinct scattering events, in which an electron scatters into the L-HRS from one event, while a positron scatters into the R-HRS in a second event within the timing window of the trigger. Lastly, there are both true and accidental $e^-\pi^+$ coincidence events. Rejection of these two backgrounds is key to the A' search and is achieved by means of a short trigger timing window and good particle identification (PID).

The other crucial factor in determining the sensitivity of this experiment is the optics, which determines the ultimate mass resolution of the experiment. Since we are looking for a narrow spike on top of a large, smooth QED background, excellent mass resolution is essential to achieve the best possible sensitivity to an A'. In the APEX experiment it is crucial to take into account all above considerations.

Figure 14 shows the lay-out of the APEX experiment. The central momenta of both spectrometers are set to half the beam energy. At such a setting the background rates are minimized, while at the same time most of A' events will be detected in spite of the small momentum bite of the HRSs.

Our *coincidence trigger* is defined as a signal in the S2m of both the left HRS *and* the right HRS, *and* a signal in the Gas Cherenkov counters of the right HRS. The coincidence trigger based on these three signals allows us to collect true coincidence events with high efficiency and acceptable DAQ dead time. Such events

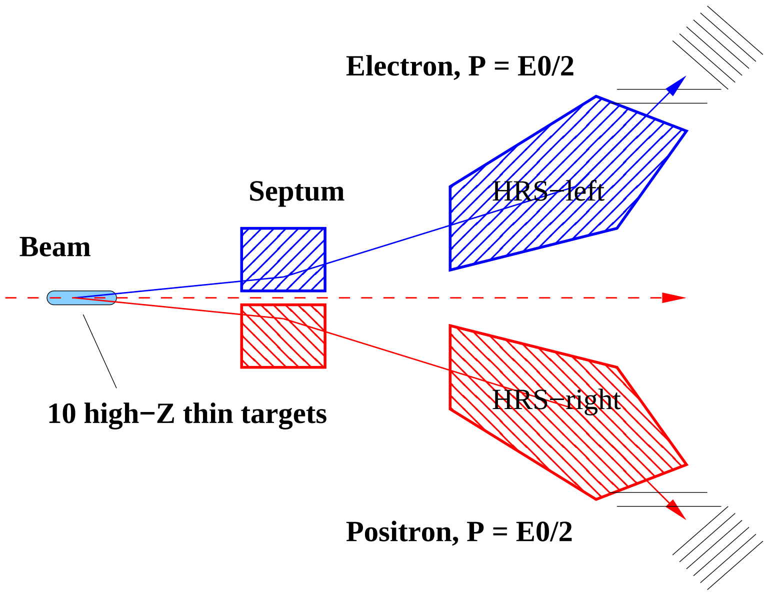

Figure 14: The lay-out of the APEX experimental setup.

are candidates for true coincident e^+e^- signal events.

The design of the target for the APEX experiment shown in Fig. 15 has a number of interesting ideas including the concept of narrow ribbons, a tension mechanism, and alignment and calibration target sets.

3.2.4 PAC35 report and concerns

PAC35 conditionally approved the APEX experiment (proposal PR12-10-009). The APEX collaboration was given a test run to address some of the PAC concerns:

1. Run with the zig-zag mesh design of the tungsten target and prove that it allows the requested vertex resolution.
2. Prove that it is possible to reach the uncertainty of 0.1 mrad in determining the central scattering angle between the two spectrometers.
3. Prove that it is possible to use the gas Cherenkov counters in the trigger to help clean up pions. In fact, the TAC report claims that this would not be possible with total rates/PMT at the level of a few hundred Hz to MHz. Also prove that an off-line rejection of 10,000:1 can be achieved.
4. Provide a detailed description of the different contributions to background and their importance (how assumptions and/or approximations can influence the predictions) and a comparison with measurement.
5. Prove that a 20 ns (S0-S0) and 40 ns (S0-S0-C) timing window can be achieved.
6. Prove that the vertical drift chambers (VDCs) can operate at a rate higher than 20 kHz/wire (that, according to the TAC report, is the maximum Hall A has operated until now).
7. If possible, set the septum magnets at higher fields to prove that also at energies higher than 2 GeV the field uniformity requested for the experiment can be achieved).

3.2.5 The results of the test run and the future plans

The test run suggested by the PAC35 report was prepared and realized after the PREX experiment in June 2010. The detectors were tested in all the extreme conditions expected during the APEX production run.

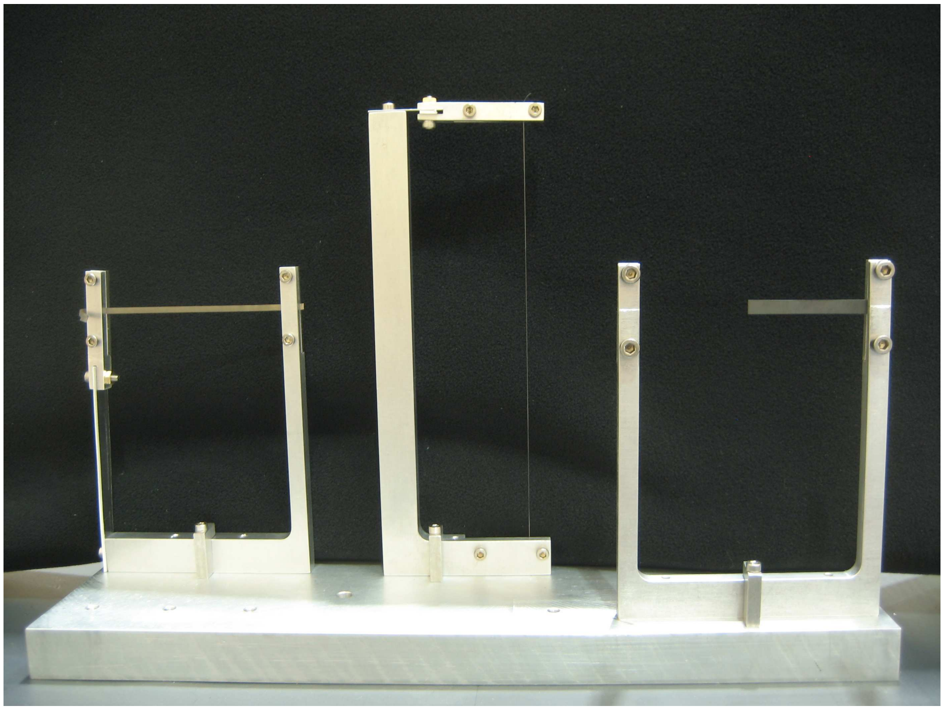

Figure 15: The components of the target for the APEX experiment.

The data were analyzed and preliminary results were presented at the A'-boson workshop [5] at JLab in September 2010. Its web page has the reports on each subsystem of the experiment and the data analysis. The observed detector performance was found to be in compliance with the APEX requirements. Several results of general interest for the Hall A collaboration are: a 15 ns coincidence time window, a 5 MHz rate capability of the VDC chambers, a target with a set of narrow ribbons for reduction of the multiple scattering, and an observation that pion rate for small angle configuration with 2.2 GeV beam is much lower than one could calculate using the commonly used code by Wiser.

The updated proposal was resubmitted to PAC37 on December 1, 2010. The e^+e^- data collected during the test run will be analyzed for a possible signal of the A' boson in the mass range 170-240 MeV. The sensitivity of this test run data goes well beyond the currently existing constraints in this mass range, but is well below that achievable in the full APEX experiment and, of course, also covers a much smaller mass range.

References

[1] B. Holdom, Phys. Lett. **B166** (1986) 196.

[2] J. D. Bjorken, R. Essig, P. Schuster, and N. Toro, Phys. Rev. **D80** (2009) 075018, [`0906.0580`].

[3] M. Reece and L.-T. Wang, *Searching for the light dark gauge boson in GeV-scale experiments*, [`0904.1743`].

[4] A New Proposal to Jefferson Lab PAC35: *Search for a New Vector Boson A' Decaying to e^+e^-*, “http://hallaweb.jlab.org/collab/PAC/PAC35/PR-10-009-Dark-Matter-Search.pdf.”

[5] The Workshop ”Searching for a New Gauge Boson at JLab”, September 20-21, 2010,“http://conferences.jlab.org/boson2010/index.html.”

3.3 E06-014

Precision Measurement of d_2^n: Probing the Lorentz Color Force

S. Choi, X. Jiang, Z.-E. Meziani, B. Sawatzky, spokespersons,
and
the d_2^n and Hall A Collaborations,
contributed by D. Parno, L. El Fassi, D. Flay, M. Posik, and Y. Zhang

3.3.1 The Experiment

Experiment E06-014 ran in Hall A from February 7 to March 17, 2009, at production beam energies of 4.73 and 5.89 GeV, on a polarized ^{3}He target. The left HRS (LHRS) and BigBite were deployed as independent detectors, each oriented at an angle of 45° to the beam line. Each detector effectively operated as a single-arm experiment, with the LHRS measuring the unpolarized scattering cross section and BigBite measuring double-spin asymmetries in scattering between a longitudinally polarized electron beam and longitudinally and transversely polarized ^{3}He gas. The experiment was designed to provide extensive coverage of the deep-inelastic scattering region, over ranges of $0.2 \leq x \leq 0.7$ and $2\ \text{GeV}^2 \leq Q^2 \leq 6\ \text{GeV}^2$.

This experiment ran immediately after E06-010, which used a similar configuration, and some calibration runs were shared between the two experiments. E06-014 was the commissioning experiment for a gas Čerenkov detector in the BigBite stack, as well as for a new photon detector and integrating data-acquisition system for the Compton polarimeter. Beam-line calibrations have been completed, and detector calibrations are well underway.

Measurement of d_2^n The primary purpose of E06-014 is the measurement of the quantity d_2^n, a probe of the strong force that is formed by taking the second moment of a linear combination of the polarized structure functions g_1 and g_2, as follows:

$$d_2^n\left(Q^2\right) = \int_0^1 x^2 \left[2g_1^n\left(x,Q^2\right) + 3g_2^n\left(x,Q^2\right)\right] dx \tag{4}$$

In addition to the access it gives to quark-gluon correlations through its dependence on g_2^n, d_2^n is of physical interest in its own right. A precision measurement of this quantity can be used to test lattice QCD predictions. At low values of Q^2, d_2^n can be associated with spin polarizabilities within the nucleon [1, 2]. At high values of Q^2, d_2^n is best interpreted as a measure of the transverse color Lorentz force on a struck quark, averaged over the nucleon as a whole [1, 3].

E06-014 sought to accomplish the measurement of d_2^n in the deep-inelastic scattering region by combining measurements of three quantities. With the LHRS we took data for the measurement of the unpolarized total cross section σ_0. In BigBite we took data for measuring two asymmetries formed between opposite target-beam spin configurations: $A_\parallel$, formed when both beam and target are polarized longitudinally, and $A_\perp$, formed when the target is polarized transverse to the longitudinal beam polarization. $A_\parallel$ and $A_\perp$ are typically measured as asymmetries in the counting rates for each spin configuration:

$$A_\parallel = \frac{N^{\downarrow\Uparrow} - N^{\uparrow\Uparrow}}{N^{\downarrow\Uparrow} + N^{\uparrow\Uparrow}} \quad \text{and} \quad A_\perp = \frac{N^{\downarrow\Rightarrow} - N^{\uparrow\Rightarrow}}{N^{\downarrow\Rightarrow} + N^{\uparrow\Rightarrow}}$$

Our independent measurements of σ_0, $A_\parallel$ and $A_\perp$ may then be combined into a measurement of d_2^n:

$$d_2^n = \int_0^1 \frac{MQ^2}{4\alpha^2} \frac{x^2y^2}{(1-y)(2-y)} \sigma_0 \left[\left(3\frac{1+(1-y)\cos\theta}{(1-y)\sin\theta} + \frac{4}{y}\tan\left(\theta/2\right)\right) A_\perp + \left(\frac{4}{y} - 3\right) A_\parallel\right] dx \tag{5}$$

where we used the kinematic variables $x = Q^2/2M\nu$ (the Bjorken x variable), $\nu = E - E'$ (the energy transfer from electron to target), θ (the scattering angle of the electron), and $y = \nu/E$ (the fractional energy transfer from electron to target). This expression of d_2^n, in terms of directly measurable quantities rather than structure functions, allowed us to divide our allocated beam time to minimize the error on the d_2^n measurement itself, rather than the error on the measurements of g_1 and g_2. Our expectation is that the

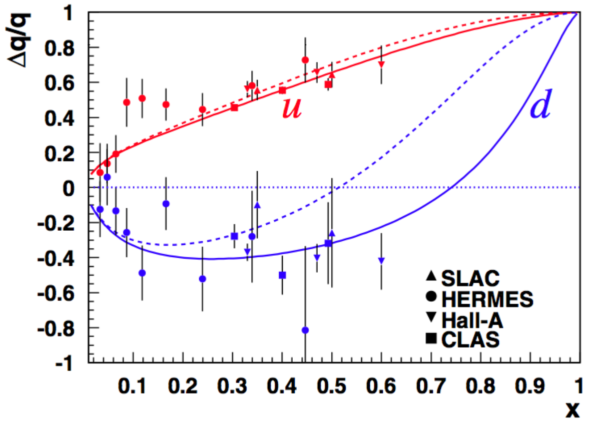

Figure 16: $\Delta q/q$ as a function of x, reproduced from Avakian *et al.* [11]. Dashed lines show the predictions of LSS(BBS) parameterizations, which use leading-order perturbative QCD with hadron helicity conservation [12]. Solid lines show predictions that explicitly include a non-zero term for the orbital angular momentum of valence quarks.

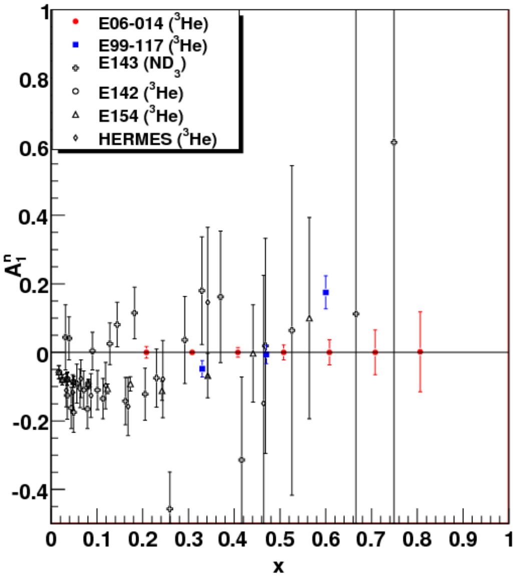

Figure 17: Projected statistical errors for E06-014's A_1^n measurement with a 5.89 GeV beam are shown in red, along with results from previous experiments [7, 13, 14, 15, 16, 17]. The x bins are chosen to have a uniform width of 0.1.

E06-014 measurement will represent a four-fold improvement in precision from previous world data [4], in advance of an approved 12 GeV experiment in Hall C that should push the precision and kinematic range still higher [5].

Measurement of A_1^n The data taken for the d_2^n measurement will also allow us to measure the longitudinal virtual photon-nucleon asymmetry for the neutron, A_1^n. When the nucleon and the virtual photon it exchanges with a lepton are both longitudinally polarized, the cross section of the process can be denoted $\sigma_{1/2(3/2)}$, where the subscript gives the projection of the total spin along the virtual photon's momentum direction when the spins are anti-parallel (parallel). A_1 is then defined as:

$$A_1\left(x, Q^2\right) \equiv \frac{\sigma_{1/2} - \sigma_{3/2}}{\sigma_{1/2} + \sigma_{3/2}} \approx \frac{g_1\left(x, Q^2\right)}{F_1\left(x, Q^2\right)} \text{ for high } Q^2 \tag{6}$$

We may also express A_1 in terms of the parallel and perpendicular asymmetries $A_\parallel$ and $A_\perp$:

$$A_1 = \frac{1}{D\left(1+\eta\xi\right)}A_\parallel - \frac{\eta}{d\left(1+\eta\xi\right)}A_\perp \tag{7}$$

where D is the virtual photon polarization factor and η, ξ, and d are quantities set by kinematics and by the virtual photon polarization vector.

Measuring A_1^n on an effective polarized neutron target (such as ^{3}He), when combined with measurements of A_1^p on a polarized proton target, gives access to the polarized-to-unpolarized parton distribution function

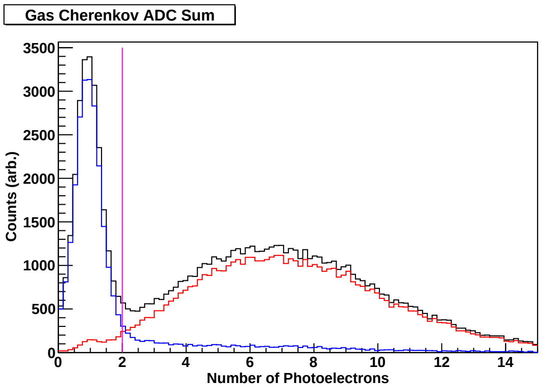

Figure 18: PID efficiency of LHRS gas Čerenkov. Pions are shown in blue and electrons in red, as determined by the pion rejectors. The magenta line shows the location of the proposed gas Čerenkov pion rejection cut, which gives a pion rejection factor of 600 while retaining 96% of electrons.

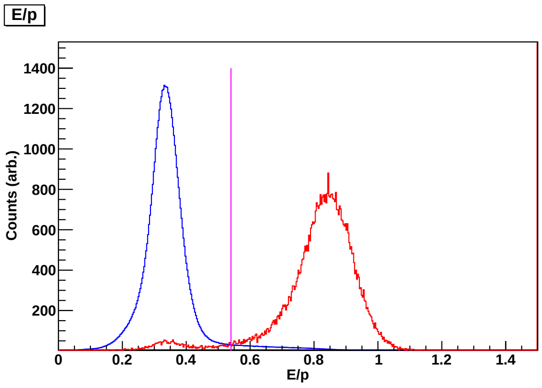

Figure 19: Pion and electron spectra in LHRS pion rejectors. The pion E/p spectrum is shown in blue and the electron spectrum in red, with these preliminary identifications determined by the gas Čerenkov; the spectra are normalized to have equal areas. The magenta line shows the location of the proposed pion rejector cut, which gives a pion rejection factor of 680 while retaining 99% of electrons.

ratios $\Delta u/u$ and $\Delta d/d$. Recent results from Hall A [6, 7] and from CLAS [8] showed a significant deviation of $\Delta d/d$ from the predictions of perturbative QCD, which have that ratio approaching 1 in the limit of $x \to 1$ (Fig. 16). As part of the 12 GeV program, two approved experiments (one in Hall A [9] and one in Hall C [10]) will extend the accuracy and x range of this measurement, but a measurement of A_1^n at E06-014's kinematics will provide valuable support (or refutation) of prior Jefferson Lab results, while producing additional input for theoretical models in advance of the coming experiments at 12 GeV. Figure 17 shows existing world A_1^n data, as well as the projected statistical errors for the E06-014 measurement using a 5.9 GeV beam. (Projections for the $E_e = 4.7$ GeV data set are not shown.)

3.3.2 Analysis Progress: Left HRS

Data from the LHRS will be used to compute the total unpolarized cross section σ_0, which will contribute to our measurement of d_2^n. Here, we discuss our analysis progress on the LHRS data over the past year. In addition to the major points discussed below, we have confirmed that the E06-010 optics are suitable for the needs of this experiment, and have begun to study data quality over our six weeks of running.

Particle Identification Particle identification (PID) in the LHRS relies primarily on the gas Čerenkov and pion rejectors, whose efficiencies must be known to high precision in order to measure a cross section. Fortunately, the two detectors may be used to calibrate one another.

Figure 18 shows the gas Čerenkov ADC sum, in photoelectrons, at a typical kinematic setting. The blue histogram contains events labeled as pions by the pion rejector, while the red histogram contains events labeled as electrons. (The black spectrum is the sum of the two.) If a cut is placed at two photoelectrons (magenta line), 96% of electrons are kept with a pion rejection factor of about 600. These results are typical across the whole kinematic range.

The results of a pion rejector PID study are shown in Fig. 19. Here, the pions (blue) and electrons (red) are selected according to readings in the gas Čerenkov. These distributions are cleanly separated in E/p: a cut at $E/p = 0.54$, corresponding to the magenta line, accepts 99% of electrons while giving a pion rejection factor of about 680.

The combined pion rejection factor from both detectors is expected to be on the order of at least 10^4 pions.

Trigger Efficiency The primary LHRS trigger for E06-014 was the T3 trigger, formed by requiring a hit in both the S1 and S2m scintillator planes; in effect, this requires that one paddle in each scintillator plane record a hit on both its left and its right photomultiplier tubes. The T4 trigger, formed by requiring a hit in two out of three detectors (the S1 scintillator plane, the S2m scintillator plane, and the gas Čerenkov, excluding an S1-S2m coincidence), allows for a check on the T3 efficiency.

In order to determine the T3 trigger efficiency, we start from the equation:

$$\varepsilon_{T3} = \frac{N_{T3}}{N_{T3} + N_{T4}}, \tag{8}$$

where $N_{T3(4)}$ is the number of T3(4)-type events adjusted for prescaling, defined as follows:

$$N_{T3(4)} = ps_{T3(4)} \times \text{bit}_{T3(4)}, \tag{9}$$

where $ps_{T3(4)}$ is the prescale value for the T3(4) trigger and $\text{bit}_{T3(4)}$ is the number of times the bit pattern was set – that is, the number of events that passed the prescale condition. The reason for using this definition for $N_{T3(4)}$ is to avoid a possible situation where some T4 triggers do *not* pass the prescale condition. This would imply (based on Eq. 8) that the T3 trigger efficiency is better than it actually is.

Table 4 shows the results binned by LHRS momentum setting. The trigger efficiency proved to be better than 99.9% across the whole kinematic range.

p [GeV]	E [GeV]	ε_{T3} [%]	ε_1 [%]
1.23	1.23	99.992 ± 0.001	98.981 ± 0.192
0.60	4.73	99.949 ± 0.021	99.282 ± 0.592
0.60	5.89	99.959 ± 0.022	99.339 ± 0.430
0.80	4.73	99.934 ± 0.038	99.209 ± 0.843
0.90	5.89	99.948 ± 0.032	99.293 ± 0.796
1.13	5.89	99.928 ± 0.053	99.228 ± 1.037
1.20	5.89	99.978 ± 0.022	99.213 ± 1.307
1.27	5.89	99.937 ± 0.045	99.172 ± 0.967
1.42	4.73	99.952 ± 0.041	99.189 ± 1.235
1.42	5.89	99.926 ± 0.064	98.810 ± 1.176
1.51	4.73	99.919 ± 0.049	99.104 ± 1.149
1.51	5.89	99.962 ± 0.031	99.172 ± 1.326
1.60	4.73	99.959 ± 0.040	98.953 ± 1.421
1.60	5.89	99.956 ± 0.041	98.832 ± 1.413
1.70	5.89	99.956 ± 0.039	98.620 ± 1.924

Table 4: The T3 trigger efficiency ε_{T3} and the VDC one-track efficiency ε_1 for each LHRS kinematic setting.

VDC One-Track Efficiency The inefficiency of the VDCs (Vertical Drift Chambers) is dominated by mistakes in the software computation of tracks, usually as a result of multi-track events or no-track events. In multi-track events, many particles cross the VDC planes simultaneously, resulting in a large number of possible trajectories. Therefore, we retain only one-track events in our analysis of the various physics quantities of interest; however, we need to be aware that such a requirement will discard any good tracks that arrive in multi-track events. To understand the effect of the one-track event requirement, we examine the zero-, multi-, and one-track efficiencies, taking zero- and multi-track efficiencies as the *inefficiency* of the VDC tracking detector [18].

We define the *one-track efficiency* ε_1 as follows: we count the number of one-track events and compare this sum to the sum of all zero-, one-, and multi-track events. Mathematically, we have:

$$\varepsilon_1 = \frac{N_1}{\sum\limits_{i=0}^{4} N_i}, \tag{10}$$

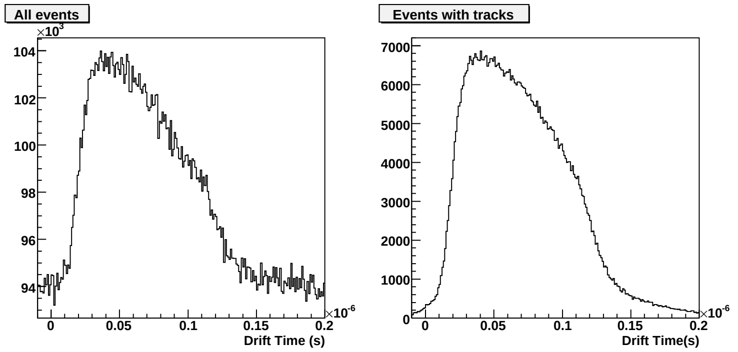

Figure 20: Calibrated t_0 spectrum for the second v plane of the first MWDC in BigBite, shown for all hits (left) and for hits that are determined by software to be part of tracks.

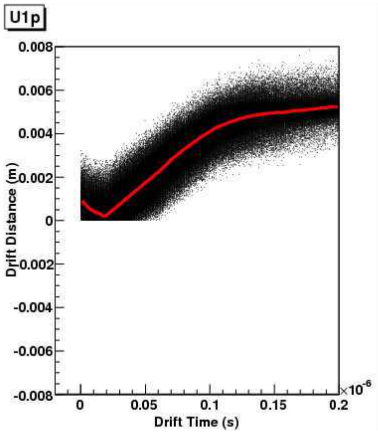

Figure 21: Data (black dots) and parameterization (red line) for time-to-distance conversion in the second u plane of the first MWDC in BigBite.

where N_1 is the number of one-track events, and N_i is the number of i-track events ($i = 0, \ldots, 4$). (The software reconstructs a maximum of up to four tracks per event [19, 20].) Similarly, we may determine the other j-track efficiencies ($j \neq 1$) as:

$$\varepsilon_j = \frac{N_j}{\sum\limits_{i=0}^{4} N_i}. \tag{11}$$

We measured one-track efficiencies ε_1 in excess of 99% across our entire kinematic range, as shown in Table 4.

3.3.3 Analysis Progress: BigBite

Data from BigBite will be used to compute the parallel and perpendicular asymmetries $A_{\parallel}$ and $A_{\perp}$, which will contribute to our measurement of d_2^n and to our measurement of A_1^n. Since BigBite is not being used to measure a cross section, absolute efficiencies are less important than they are for the LHRS. Here, we discuss our analysis progress on the BigBite data over the past year. In addition to the topics described below, we have begun to study data quality and compute preliminary asymmetries.

Multi-Wire Drift Chambers In order to improve our understanding of the behavior and locations of the wires in the BigBite Multi-Wire Drift Chambers (MWDCs), we have completed a t_0 timing calibration for all planes. This allows us to effectively separate the timing of electrons in the wire chamber from time-of-flight to the shower, and from the timing of the trigger electronics. The results of this calibration are shown in Fig. 20; the rising edge of the drift time spectrum shows the t_0 calibration. We then parameterized the relationship between drift time and drift distance (Fig. 21) for each plane, which in turn allowed us to calculate the actual wire positions empirically.

Armed with accurate positions for the wires in the MWDCs, we find track residuals for all planes to range from 190 to 265 μm. Figure 22 shows representative residual plots for the six u planes.

Optics We took as a starting point the BigBite optics package for E06-010 [21], which allowed us to rapidly achieve an excellent vertex reconstruction (Fig. 23) with centimeter-level resolution.

For our momentum reconstruction, we deviated from the E06-010 approach. We adapted its first-order optics model, which places the proton peak from our 1.232-GeV, elastic H_2 calibration data at $W = 0.938$ GeV/c^2. For particles with very low momenta, at the edge of the BigBite acceptance, a further correction factor is then necessary in order to place the Δ peak at $W = 1.232$ GeV/c^2; we therefore applied the E06-010

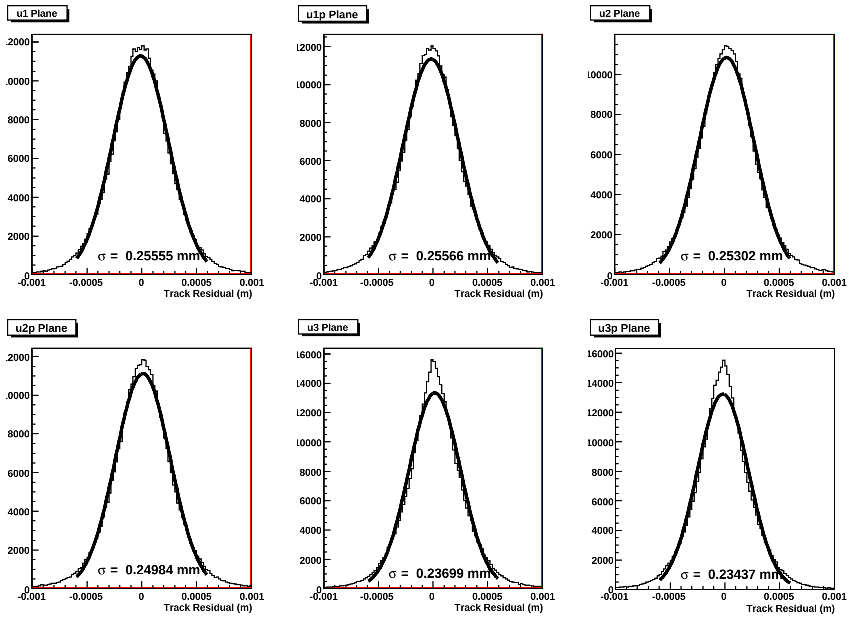

Figure 22: Track residuals for u planes in the multi-wire drift chambers.

optics package's linear correction at low momenta. This correction, however, is not continuous in the first derivative with the uncorrected momentum, resulting in a sharp discontinuity in the momentum spectrum at 0.9 GeV/c (Fig. 24). To restore continuity to our momentum reconstruction, we derived a quadratic function that smoothes the transition between the low-momentum region and the rest of the spectrum. With $p^{(1)}$ the first-order momentum, the final reconstructed momentum p is then of the form

$$p = \begin{cases} p^{(1)} & \text{for } p^{(1)} > 0.95 \text{ GeV} \\ p^{(1)} - 3.7\left(p^{(1)} - 0.95 \text{ GeV}\right)^2 & \text{for } 0.85 \leq p^{(1)} \leq 0.95 \text{ GeV} \\ p^{(1)} + 0.148\left(p^{(1)} - 0.9 \text{ GeV}\right) & \text{for } p^{(1)} < 0.9 \text{ GeV} \end{cases} \tag{12}$$

Figure 25 shows the resulting invariant-mass spectrum for elastic scattering from hydrogen atoms. Figure 26 shows a momentum resolution of 1.1% for the same data.

Shower and Preshower The preshower and shower detectors in BigBite are arrays of lead-glass blocks designed to capture the energy of an incident particle. The 54 preshower blocks are arranged in a 2×27 array, and the 189 shower blocks form a 7×27 array. Each block is mated to a photomultiplier tube (PMT). The signals from a cluster of adjacent blocks are summed to determine the energy of the particle that produced the signal.

The energy E_i deposited in the i^{th} shower or preshower block is related to the signal amplitude A_i and pedestal P_i according to

$$E_i = C_i \left(A_i - P_i\right) \tag{13}$$

The coefficients C_i must be determined via calibration of the total shower and preshower signal to the corresponding track momentum, reconstructed using the BigBite optics. We compute the 243 total coefficients using a linear fit to minimize χ^2, the square of the difference between the reconstructed momentum p and the total energy reported by both the preshower and the shower. Over M good electron tracks, χ^2 is given by

$$\chi^2 = \sum_{i=1}^{M} \left[p_i - \sum_{j=1}^{N^{ps}} C_{ij}^{ps} \left(A_{ij}^{ps} - P_j^{ps}\right) - \sum_{k=1}^{N^{sh}} C_{ik}^{sh} \left(A_{ik}^{sh} - P_k^{sh}\right) \right]^2 \tag{14}$$

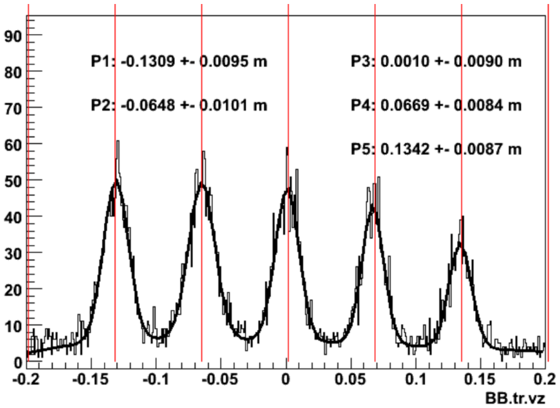

Figure 23: Vertex reconstruction for tracks belonging to negatively-charged particles issuing from a carbon-foil target in a five-pass run. The measured peak locations are compared to the surveyed foil positions, marked in red.

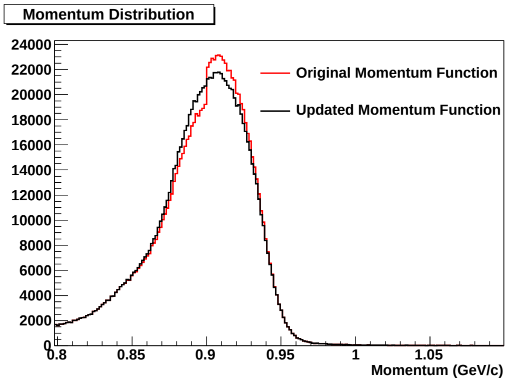

Figure 24: Momentum spectrum for negatively charged particles in data taken with a beam energy of 1.232 GeV and an H_2 target. The red histogram shows the momentum spectrum resulting from the linear low-momentum correction in the E06-010 optics package. The black histogram makes use of the correction described by Eq. 12.

where N^{ps} and N^{sh} are the number of blocks in a preshower cluster and in a shower cluster, respectively [22].

We have completed a shower and preshower calibration using several four-pass production runs, taken relatively late in the E06-014 experiment. Figure 27 shows E plotted against p; the densely populated region along $E \approx p$ corresponds to the expected value for electrons.

E06-014 ran for six weeks, during which radiation damage slowly yellowed the lead-glass preshower and shower blocks. Consequently, the quality of this calibration must be checked over a wide time range, and the run period will likely be divided into successive time windows, each with its own energy calibration.

Gas Čerenkov E06-014 was the commissioning experiment for the BigBite gas Čerenkov, which was placed in the detector stack between the multi-wire drift chambers and the preshower. Its purpose was to aid in removing pion contamination, both in the on-line trigger and in off-line analysis. We have completed an LED calibration and preliminary pion rejection and electron efficiency calculations, treating the two sides (beam side and RHRS side) separately due to the fact that their rates differed by an order of magnitude.

The twenty PMTs of the gas Čerenkov, each with coverage of a slightly different region of the detector, are calibrated using LED runs. Figure 28 shows a representative ADC spectrum from such a run. We used a convolution of Gaussian and Poisson functions to fit the pedestal and the single-photoelectron peak, allowing us to adjust our settings to place the single-photoelectron peak at thirty ADC channels above the pedestal.

Figures 29 and 30 show the ADC signal spectra in the gas Čerenkov for accidentals (in blue) and for particles coincident with the trigger (in red), for both high-rate (beam side) and low-rate (RHRS side) parts of the detector. Here, accidentals are defined as events where the Čerenkov TDC timing fell outside the T2 trigger timing window; particles coincident with the trigger have timing within that window.

To compute preliminary pion rejection factors and electron efficiencies, we applied cuts on preshower energy and E/p in order to select a pion sample (Fig. 31) and an electron sample (Fig. 32). The E/p value for each event comes from the total energy (shower and preshower) and the reconstructed momentum for the track.

Our first task is to determine how efficiently we can reject pions using a cut on the ADC signal corresponding to the particular PMT that should have detected the pion track. We define the pion rejection factor ϵ_π as

$$\epsilon_\pi = \frac{N_\pi^{total}}{N_\pi^{accept}} \tag{15}$$

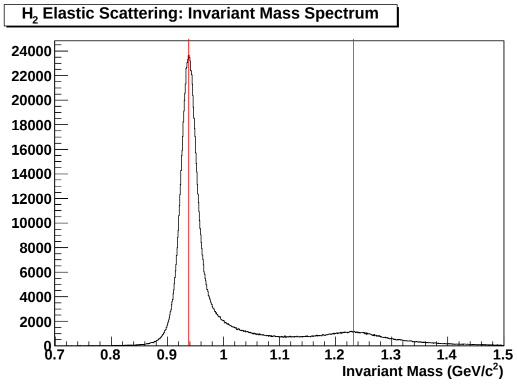

Figure 25: Reconstructed invariant mass spectrum for H$_2$ elastics data in BigBite. The red lines mark the known masses of the proton and of the $\Delta(1232)$.

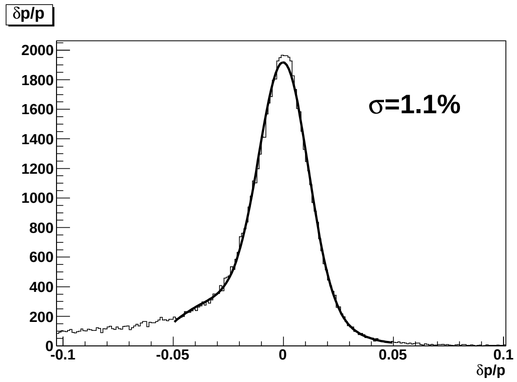

Figure 26: Momentum resolution for BigBite negative optics, plotted as $\delta p/p = (p - p_{elas})/p$.

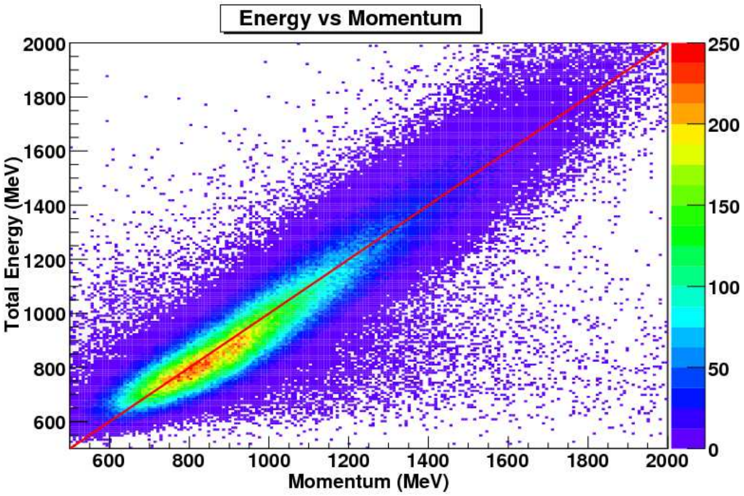

Figure 27: Distribution of E vs p for calibrated preshower and shower. The red line at 45° highlights the ideal condition in which the reconstructed momentum and energy are equal.

where N_π^{total} is the total number of events in the pion sample (as selected from shower and preshower data) and N_π^{accept} is the number of those events that pass the Čerenkov ADC cuts and are thus misidentified as electrons. We calculated ϵ_π independently for several choices of cut threshold; the preliminary results, averaged over each side of the detector, are shown in Fig. 33. At best, we see a pion rejection factor of about 200 on the small-angle side, while the large-angle side sees a pion rejection factor closer to 900; we believe this discrepancy is due to hardware issues associated with the rate difference between the two sides.

We have also made preliminary determinations of the detector's electron efficiency – that is, the degree to which electrons pass the Čerenkov ADC cuts rather than being misidentified as pions –. We began with an electron sample determined by shower and preshower data (Fig. 32). Where N_e^{total} is the number of events in this electron sample, we define the electron efficiency ϵ_e as

$$\epsilon_e = \frac{N_e^{accept}}{N_e^{total}} \tag{16}$$

where N_e^{accept} is the number of events in the electron sample that pass the ADC cuts. We computed ϵ_e in three ways for each PMT. First, we calculated the efficiency for a zero-photoelectron ADC cut, i.e. the

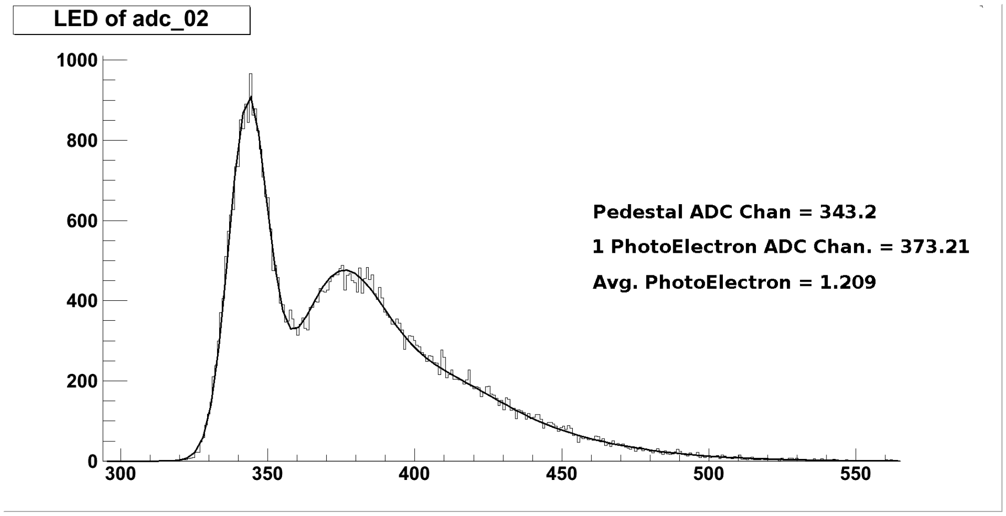

Figure 28: Calibrated spectrum of a BigBite gas Čerenkov PMT for an LED run. Fits to the pedestal and single-photoelectron peak allowed the latter to be aligned at the 30-channel mark.

detection efficiency. Second, we repeated the calculation for a three-photoelectron ADC cut. Finally, in order to account for the statistical fact that real electrons will not always produce three or more photoelectrons even under ideal circumstances, we fit a Poisson distribution to the ADC spectrum of each PMT. This allowed us to compute the expected electron efficiency for a three-photoelectron cut.

Figure 34 shows preliminary ϵ_e values for the small-angle side of the detector; preliminary results for the large-angle side are shown in Fig. 35. With the exception of PMTs 1 and 8, which are on the upper and lower edges of the acceptance, we measured a detection efficiency greater than 90% in all PMTs. The expected efficiencies for a three-photoelectron cut are generally consistent with the detection efficiencies, but the efficiencies for the empirical three-photoelectron cut drop as low as 50% for PMTs at the top and bottom of the acceptance on the high-rate, small-angle side. In general, as with pion rejection, we measured significantly better performance on the large-angle side, where rates were lower; here, even empirical three-photoelectron cuts routinely resulted in better than 90% electron efficiencies.

3.3.4 Analysis Progress: Target

E06-014 used the standard Hall A polarized ^{3}He target with two holding field directions: longitudinal and transverse in-plane with respect to the beam direction. To extract the target polarization, we have conducted several measurements to calibrate different target system components.

Target Density Knowledge of the ^{3}He target density is crucial for the extraction of the target polarization and the cross sections. The target's cell density is measured by observing the collisional absorption broadening of the D1 and D2 resonance lines of the alkali metal rubidium (Rb) in the presence of the ^{3}He gas [23]. We have measured and fit the absorption spectra to compute an ^{3}He density, including its pressure broadening (PB), of 8.099 ± 0.032 amg, where an amagat (amg) is 2.687×10^{25} m^{-3}.[7]

Thickness of Target Cell The cell's glass entrance-window and side-wall thicknesses are essential input parameters in the calculation of radiative corrections and in the extraction of cross sections. The determination of a transparent thin-film thickness can be performed by taking advantage of the interference of the reflected light from the front surface of the film and the reflected/refracted light from its back internal surface, as is shown in Fig. 36. This interference depends on the difference of the two optical path lengths, and hence on the relative phase of the interacting waves [24].

---

[7] For reference, a comparable measurement of the ^{3}He density in this cell was performed at the University of Virginia before the experiment. The result, including PB, was 7.99 ± 0.01 amg.

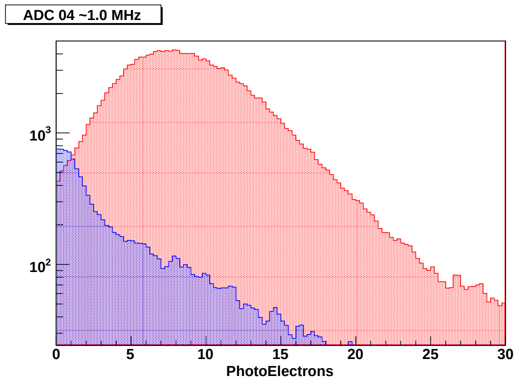

Figure 29: BigBite gas Čerenkov ADC signal spectra for a beam-side PMT with a rate of about 1 MHz. Particles in the blue histogram are accidentals while particles in the red histogram could have caused the trigger, as determined by their TDC timing relative to the trigger window.

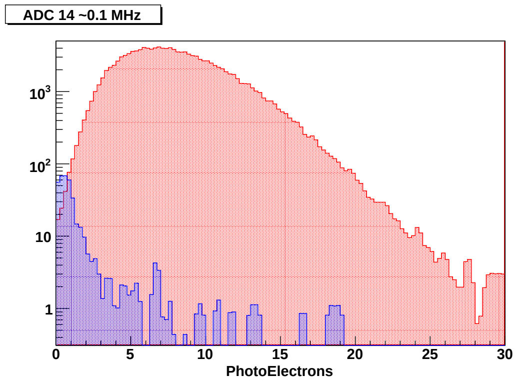

Figure 30: BigBite gas Čerenkov ADC signal spectra for a RHRS-side PMT with a rate of about 0.1 MHz. Particles in the blue histogram are accidentals while particles in the red histogram could have caused the trigger, as determined by their TDC timing relative to the trigger window.

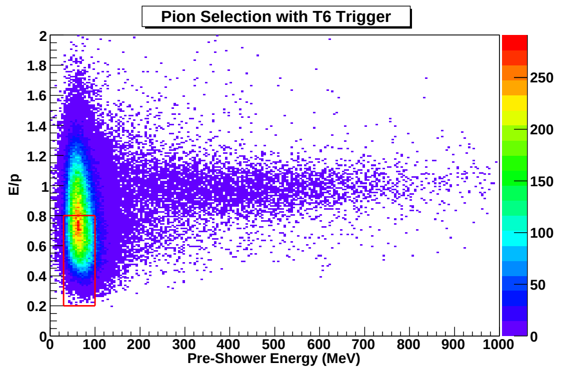

Figure 31: Pion selection for BigBite gas Čerenkov studies.

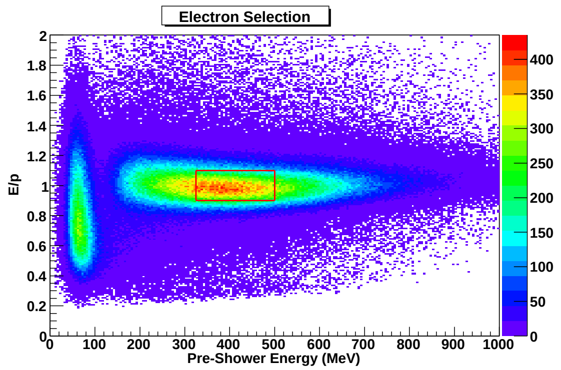

Figure 32: Electron selection for BigBite gas Čerenkov studies.

We have performed several data scans to measure the glass thickness of the polarized ^{3}He and reference cells, called Samantha and GMA respectively. Tables 5 and 6 summarize the side wall and window thicknesses of the two cells. The statistical uncertainty of each measurement is about 2%. The main systematic uncertainty (of $< 1\%$) comes from the determination of the tilt angle between the incident laser and the glass.

Electron Paramagnetic Resonance A measurement of an electron paramagnetic resonance (EPR) uses the stimulated light emission from the target's alkali metals as a magnetometer. This allows us to measure the net change in the magnetic field magnitude seen by the Rb atoms in the pumping chamber when the ^{3}He nuclei are polarized in alignment with the external holding field, compared to when their spins are anti-aligned with the same holding field. A summary of the EPR polarization extracted from the measurements taken during the E06-014 running period is shown in Figure 37. Figure 38 shows preliminary polarization measurements for the whole E06-014 running period, based on roughly calibrated NMR measurements and an interpolation of the pumping chamber polarization from the EPR measurements.

Nuclear Magnetic Resonance A water calibration study is in progress and will allow us to determine the target's polarization using the adiabatic fast passage (AFP) nuclear magnetic resonance (NMR) mea-

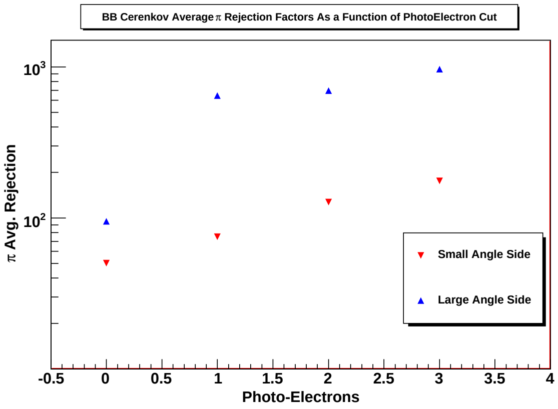

Figure 33: Average pion rejection factors for the BigBite gas Čerenkov, plotted as a function of the threshold of the Čerenkov ADC cuts. Small- and large-angle averages are plotted separately due to the rate difference between the sides. PMTs 9, 10, 19 and 20 (at the bottom of the detector stack) were not included in the calculation because they are outside our acceptance.

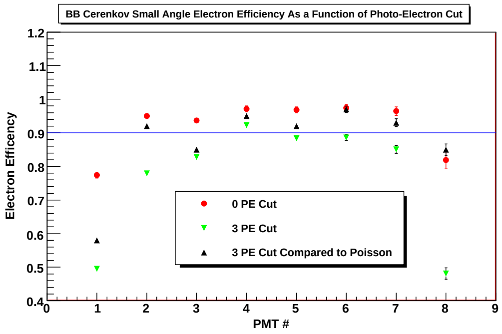

Figure 34: BigBite gas Čerenkov electron efficiency (small-angle side). We have drawn a line at 90% to guide the eye. PMTs 9 and 10 are outside our acceptance.

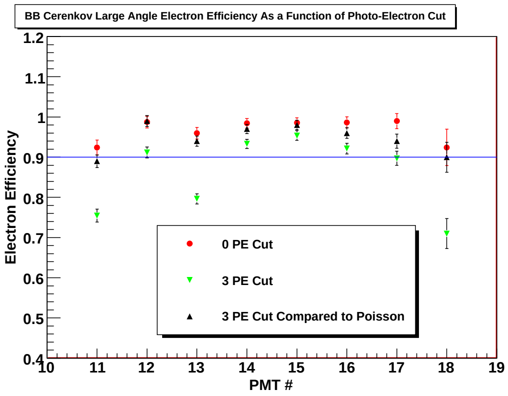

Figure 35: BigBite gas Čerenkov electron efficiency (large-angle side). We have drawn a line at 90% to guide the eye. PMTs 19 and 20 are outside our acceptance.

surements taken during the experiment. Since these measurements were performed only three times a day, we will need to interpolate the results in time in order to arrive at a target polarization for each production run. The final target chamber polarization number for each run will be an average of the interpolated NMR result with the interpolated EPR result.

References

[1] M. Burkardt, hep-ph/0905.4079v1 (2009).

[2] E. Stein *et al.*, Phys. Lett. B **343**, 369 (1995).

[3] M. Burkardt, AIP Conference Proceedings **1149**, 62 (2008), hep-ph/0902.0163v1.

[4] S. Choi, Z.-E. Meziani, X Jiang, B. Sawatzky, *et al.*, Jefferson Lab PAC PR-06-014 (2005).

[5] T. Averett, W. Korsch, Z.-E. Meziani, B. Sawatzky*et al.*, Jefferson Lab PAC E1206121 (2010).

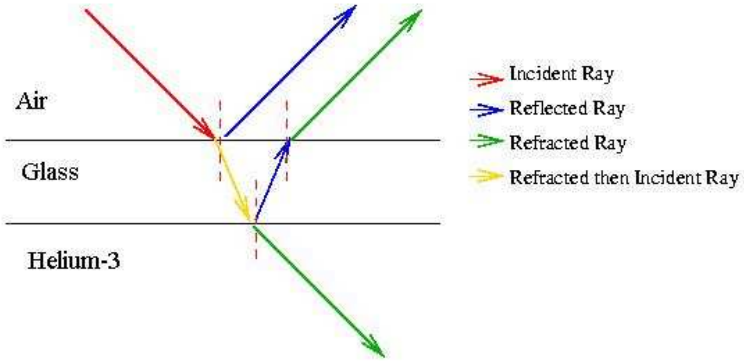

Figure 36: Illustration of the interference phenomenon in glass-thickness measurements.

Point	Position [cm]	Glass Thickness [mm]
A	2.5→W1	1.81
B	12.5→W1	1.69
C	20.3→W1	1.74
D	23.4→W1	1.75
E	36.4→W1	1.73
F	3.0→W2	1.72
G	9.0→W2	1.68
H	20.0→W2	1.64
I	28.4→W2	1.66
J	37.4→W2	1.70
W1	-	0.13
W2	-	0.13

Table 5: Fit results for the thickness of the reference cell (GMA). The positions of each measurement point are given with respect to W1 and W2, the upstream and downstream cell windows. Points A-E are on the beam right side of the target and points F-J are on beam left.

[6] X. Zheng *et al.*, Phys. Rev. Lett. **92**, 012004 (2004).

[7] X. Zheng *et al.*, Phys. Rev. C **70**, 065207 (2004).

[8] K. V. Dharmawardane *et al.*, Phys. Lett. B **641**, 11 (2006).

[9] G. Cates, N. Liyanage, Z.-E. Meziani, G. Rosner, B. Wojtsekhowski, X. Zheng, *et al.*, Jefferson Lab PAC E1206122 (2006).

[10] G. Cates, J.-P. Chen, Z.-E. Meziani, X. Zheng *et al.*, Jefferson Lab PAC E1210101 (2010).

[11] H. Avakian, S.J. Brodsky, A. Deur, and F. Yuan, Phys. Rev. Lett. **99**, 082001 (2007).

[12] E. Leader, A. V. Sidorov, and D. B. Stamenov, Int. J. Mod. Phys. **A13**, 5573 (1998).

[13] D. Adams *et al.*, Phys. Lett. B **357**, 248 (1995).

[14] P. L. Anthony *et al.*, Phys. Rev. D **54**, 6620 (1996).

[15] K. Ackerstaff *et al.*, Phys. Lett. B **404**, 383 (1997).

[16] K. Abe *et al.*, Phys. Rev. Lett. **79**, 26 (1997).

[17] K. Abe *et al.*, Phys. Rev. D **58**, 112003 (1998).

Point	Position [cm]	Glass Thickness [mm]
A	2.5→W1	1.56
B	12.5→W1	1.56
C	20.3→W1	1.75
D	25.4→W1	1.70
E	35.6→W1	1.70
F	2.5→W2	1.70
G	11.4→W2	1.67
H	19.1→W2	1.67
I	26.7→W2	1.61
J	35.6→W2	1.68
W1	-	0.12
W2	-	0.13

Table 6: Fit results for the thickness of the polarized ^{3}He cell (Samantha). The positions of each measurement point are given with respect to W1 and W2, the upstream and downstream cell windows. Points A-E are on the beam right side of the target and points F-J are on beam left.

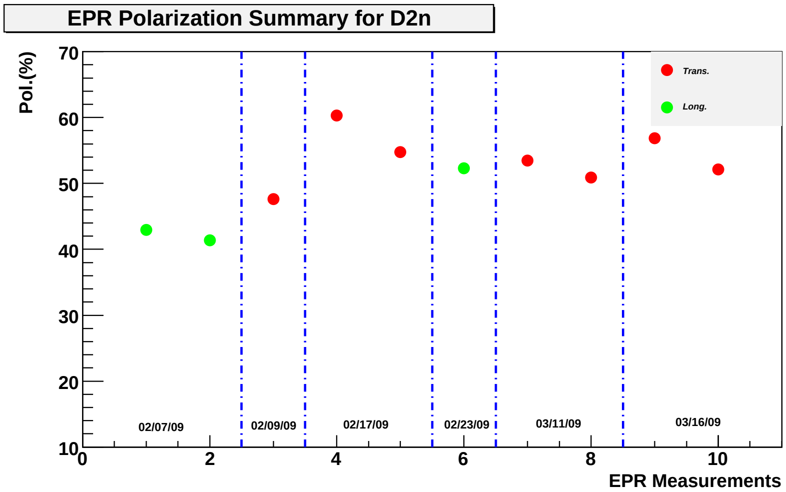

Figure 37: EPR measurements.

[18] P. H. Solvignon, PhD thesis, Temple University (2006).

[19] J. Alcorn *et al.*, Nucl. Instr. and Meth. in Phys. Res. A **522**, 294 (2004).

[20] A. Orsborn, *Report for DoE Science Undergraduate Laboratory Internship Program* (2005).

[21] X. Qian, PhD thesis, Duke University (2010).

[22] K. Allada, PhD thesis, University of Kentucky (2010).

[23] I. Kominis, PhD thesis, Princeton University (2001).

[24] E. Hecht, *Optics*, Addison-Wesley (2002).

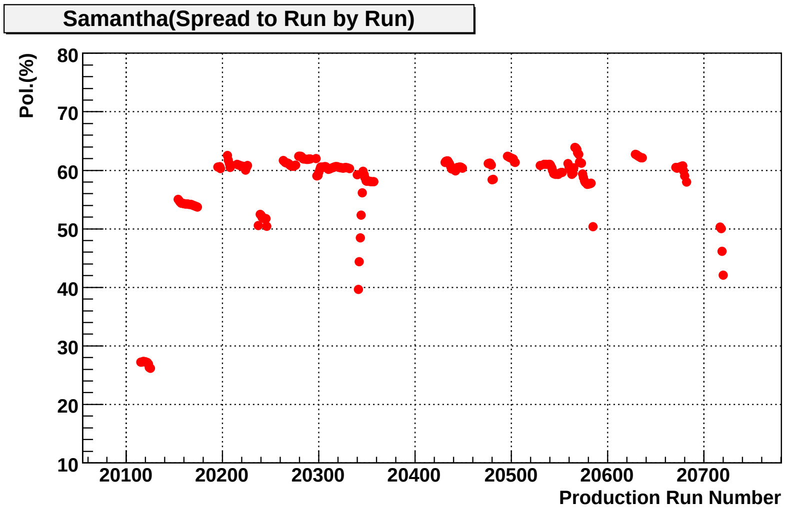

Figure 38: Preliminary pumping-chamber polarization, calibrated by the EPR measurements.

3.4 E07-007/E08-025

A. Camsonne, C. Hyde, M. Mazouz, C. Muñoz Camacho and J. Roche, spokespersons,
and
the Hall A Collaboration

3.4.1 Goals of the experiments

Deeply Virtual Compton Scattering (DVCS) experiments E07-007 and E08-025 aim to perform a Rosenbluth-like separation of the DVCS cross section on both the proton (E07-007) and the neutron (E08-025). By using different beam energies at the same virtual photon kinematics, it is possible to isolate the contribution of the $|\mathrm{DVCS}|^2$ term to the DVCS cross section from the term originating from the interference of DVCS with the Bethe-Heitler (BH) process. The Q^2-dependence of each term of the cross section will be measured in order to test the applicability of the twist-2 dominance and the formalism of Generalized Parton Distributions. An additional goal of both E07-007 and E08-025 is to perform an L/T separation of the π^0 electroproduction cross section, on both the proton and the neutron. Due to the low energy beam available during the running of Q-weak, the DVCS kinematics have been revised. Table 7 shows the new kinematics of the experiment, which differ from the original ones proposed and accepted by PAC31 [1] and PAC33 [2].

	KIN I		KIN II		KIN III	
Q^2 (GeV^2)	1.5		1.75		2.0	
x_B	0.36		0.36		0.36	
W^2 (GeV^2)	3.55		3.99		4.44	
q' (GeV)	2.22		2.59		2.96	
k (GeV)	5.552	3.356	5.552	4.454	5.552	4.454
k' (GeV)	3.332	1.136	2.962	1.864	2.591	1.494
θ_e (deg)	16.37	36.56	18.78	26.55	21.49	31.82
θ_q (deg)	-21.74	-15.47	-19.13	-16.64	-16.82	-13.89
θ_{Calo} (deg)	-19.39	-14.78	-16.79	-14.78	-14.78	-14.78

Table 7: Revised DVCS kinematics. Neutron DVCS runs at KIN II only.

The energy limitation has the following impact on the physics reach of the experiments:

- Reduced lever arm in Q^2: 1.5–2.0 GeV^2 (instead of 1.5–2.3 GeV^2).
- The first Q^2-setting (at 1.5 GeV^2) will be closer to the nucleon resonance region $W^2 = 3.55$ GeV^2 (it was planned at $W^2 = 3.78$ GeV^2).

3.4.2 Experimental status

The experiment started taking data in early October 2010 and is scheduled to finish by the end of December 2010. At the moment of writing, more than half of the statistics has been collected. A dedicated PbF_2 electromagnetic calorimeter and matching 1 GHz sampling custom electronics read-out system were constructed. The construction and test of the calorimeter started in February and the installation in the Hall took place during July and August. Figure 39 shows the DVCS arm. Figure 40 shows the energy resolution of the calorimeter at 3 GeV, obtained from an on-line analysis of elastic scattering on a hydrogen target (the proton is detected in the L-HRS and the electron in the calorimeter). Figure 41 shows some additional on-line results. The left histogram shows the invariant mass of events where two clusters are reconstructed in the calorimeter, showing a very clean peak around the π^0 mass. The plot on the right shows the missing mass squared for the $ep \to e\gamma X$ reaction, with DVCS events accumulating at around $M_X^2 = (0.938)^2\,\mathrm{GeV}^2$.

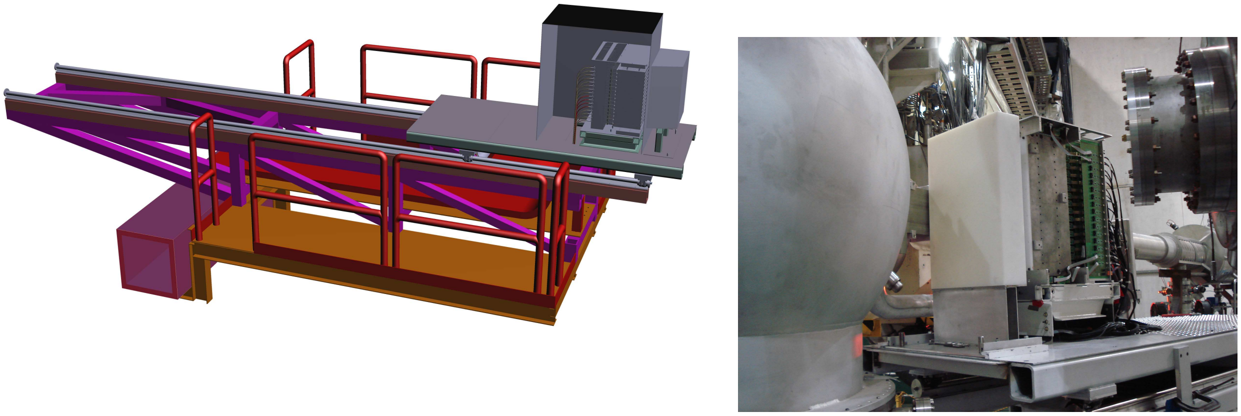

Figure 39: Left: DVCS stand. The calorimeter can slide between the data taking position (1.1 m from the target center) to the calibration position (5.5 m from the target). Right: Calorimeter in position in the hall. During data taking, an aluminum box covers the calorimeter.

Because the right HRS was unavailable during the experiment, the luminosity was monitored by lumi detectors that consist of lucite bars, mounted normal to the downstream beam line, and connected to PMTs. The lumi signals were converted to frequency and then read out by scalers. The PbF_2 block selection done at the Pocatello facility to eliminate "bad" blocks that are less radiation hard, turned out to be quite successful. The average gain variation was about 7% with only a few blocks having up to 30 % gain variation which could have been reduced if a larger pool of PbF_2 blocks had been available.

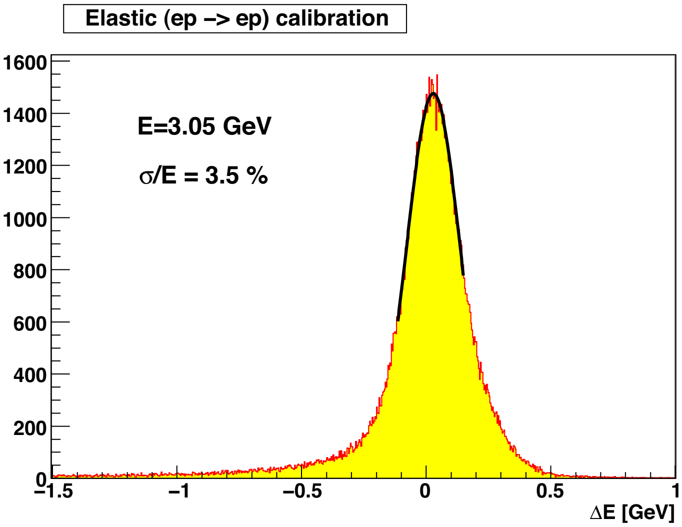

Figure 40: On-line result for the energy resolution of the DVCS calorimeter, as obtained from elastic scattering.

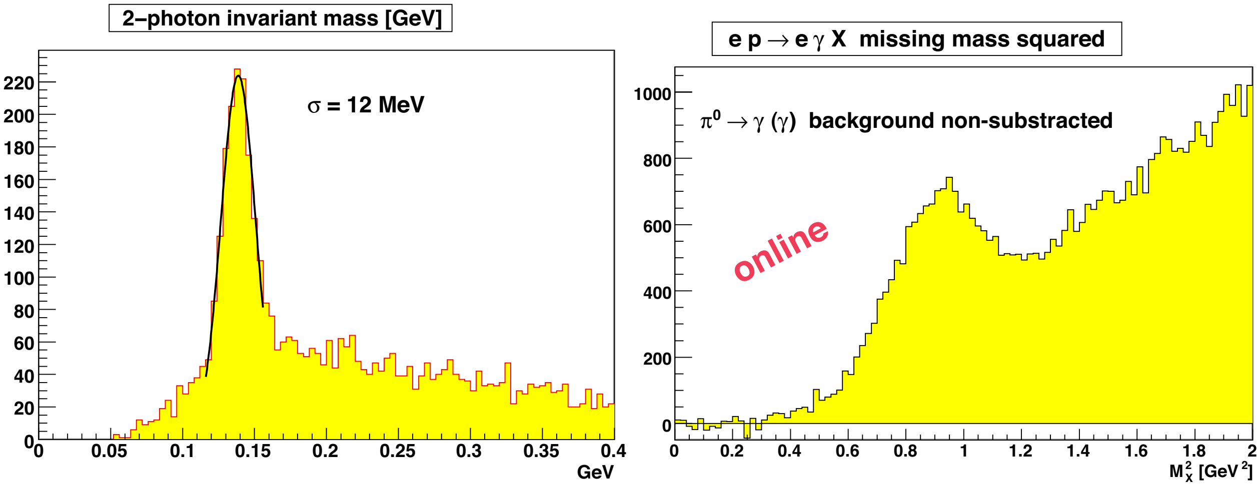

Figure 41: (Left) Invariant mass of two-cluster events in the calorimeter. (Right) $ep \rightarrow e\gamma X$ missing mass squared from on-line analysis.

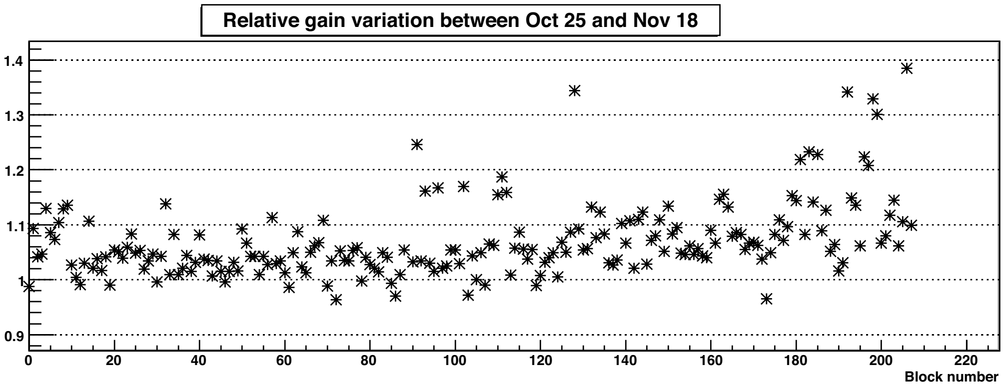

Figure 42: Calorimeter gain variation between two elastic calibrations for each calorimeter block

3.4.3 Data acquisition

The first DVCS experiment used a dedicated analog sampling electronics (Analog Ring Sample: ARS) to record the waveform of each calorimeter channel in order to treat pile-up events off-line. The first experiment deployed the system successfully though the dead time for the system was quite significant. In order to reduce the dead time a calorimeter trigger was used to set a threshold on the photon energy, even though the threshold generated a systematic error on the π^0 background. In order to improve this situation an upgrade of the electronics was planned which used buffering and a faster transfer protocol to run with a lower threshold. A calorimeter trigger was also developed to trigger on the sum of all blocks.

The first prototype board was delivered in January 2010 after having been tested in Clermont Ferrand with a Labview setup. The read-out was developed and tested with CODA in the Test Lab with a stand-alone VME set-up. Cosmics data showed some issues with the synchronization of the data. The full set-up was installed in the HRS in August implementing the full logic and TS supervisor although the synchronization issues had not been resolved. With the help of the JLab Electronics and CODA groups a test bench was set up in the DAQ Lab that allowed to independently test the electronics while taking data. The data synchronization problems were solved by modifying the firmware. The ARS electronics was first tested with buffering and finally using the VME2eSST protocol at half speed (160 Mbytes/s) allowing to take most of the data in single-arm mode while the trigger module was delayed. The data rate recorded was around 16 Mbytes/s at maximum dead-time values of around 30%. A larger dead time plagued the data for a few weeks until it was traced to the network switch. The dead time with buffering is higher than expected and still needs to be studied though it was sufficient for most of the data taking and the amount of data taken was 10 times larger than in the previous experiment at a similar value of dead time. The read-out of the full calorimeter mostly in singles mode will allow to have a cross check using deep-inelastic scattering and a more extensive study of the background. While data was taken in singles mode, the trigger module was being worked out, the calorimeter was put in production on December 15th allowing to run at the nominal current of 3 μA while the data taking was limited to 1 μA because of the dead time. Data is being checked but no major inefficiencies or problem in thresholds were seen. We wish to thank Chris Cuevas and Benjamin Raydo from the JLab Electronics Group and David Abbott and Ed Jastrzembski from the CODA group for their support.

3.4.4 Polarimetry and helicity

The beam polarization has been measured in a quasi-continuous way by the photon detector of the Compton polarimeter. The Møller polarimeter has been used to cross-check the Compton results, but used only occasionally since it required a significant downtime in order to cool the Møller magnet. Running simultaneously with the Q-weak experiment the beam spin direction at the target was only partially longitudinal (90% longitudinal at 3 pass, 91% at 4 pass and 94% at 5 pass). Moreover, Q-weak used high helicity-flip rates (up to 1 kHz) with delayed reporting. Since the DVCS DAQ rates were in all cases lower than 500 Hz, a new electronic scheme was developed that registered every helicity state without dead time and without artificially raising the DAQ rate to match the helicity-flip rate. This scheme relied on the use of a ring buffer available in the VME scalers used during the data taking [3]. Dedicated software was developed to read out the ring information.

References

[1] E07-007 experiment proposal: `http://www.jlab.org/exp_prog/proposals/07/PR-07-007.pdf`

[2] E08-025 experiment proposal: `http://www.jlab.org/exp_prog/proposals/08/PR-08-025.pdf`

[3] Hall A in Qweak Helicity Mode, R. Michaels,
`http://hallaweb.jlab.org/equipment/daq/qweak_helicity.html`

3.5 E06-002

PREX in 2010

The PREX Collaboration

The Lead Radius Experiment (PREX) ran from March 19 to June 20, 2010. Because of various problems the experiment took only ∼20% of the statistics required but was a major accomplishment as a first measurement of its kind and many milestones were met. We have formulated a request for a follow-up measurement with anticipated improvements to take data at a rate equivalent to the original proposal estimates.

The goal of the experiment is to measure the parity-violating asymmetry in elastic scattering $A = (\sigma_R - \sigma_L)/(\sigma_R + \sigma_L)$ from the ^{208}Pb nucleus. This asymmetry is sensitive mainly to the neutron radius R_n because the weak charge of the neutron is much larger than that of the proton [1]. In PWIA, the relationship between the asymmetry and the neutron form factor is given by Eq. 17

$$A_{LR} = \frac{G_F Q^2}{4\pi\alpha\sqrt{2}}\left[1 - 4\sin^2\theta_W - \frac{F_n(Q^2)}{F_p(Q^2)}\right] \tag{17}$$

where G_F is the Fermi constant, $\alpha = \frac{1}{137}$ is the fine-structure constant, θ_W is the Weinberg angle, and $F_n(Q^2)$ and $F_p(Q^2)$ are the neutron and proton form factor of the nucleus. Coulomb distortions are the largest correction and have been calculated by Horowitz[2].

The size of a heavy nucleus, or equivalently, the central density of nuclear matter ρ_0, is a fundamental property central to nuclear physics. Important applications include: 1) neutron-rich matter in Astrophysics; 2) understanding nuclear structure; 3) structure of neutron rich radioactive beams; 4) atomic parity-non-conservation (PNC) experiments. Two international workshops of the broad impact of PREX have been held, one at JLab in 2008 and the other in Trento in 2009.

PREX ran at a 1.063 GeV energy with the new warm-temperature septum magnets at 5° with 50 μA (and 4 days at 70 μA), 85% polarized beam at 120 Hz helicity reversal rate. Unfortunately, only about 20% of the required statistics were obtained. Problems with radiation degrading the vacuum seals in the scattering chamber, and the controls systems for the HRS magnets, caused major losses in running time. However, we did accomplish a large number of milestones that are critical to the future of the parity program in general and a potential future run of PREX in particular.

To obtain the necessary statistical precision, our cumulative pulse-pair width (in 30 ms) had to be $\ll$ 200 ppm. To achieve the necessary electronic noise requirement, custom 18-bit ADCs were built (Fernando Barbosa, Ed Jastrzembski). In addition, running at a higher rate of helicity flipping helped. We had the option to run at 240 Hz, but found 120 Hz more convenient. To achieve a narrow width from the integrating detector for 1 GeV, new quartz detectors were developed by UMass and Smith College.

An indication of the quality of our data can be seen from Figs. 43, 44 and 45. These are *preliminary* and *blinded* asymmetries. The blinding includes both the "usual" blinding method (see below) plus an offset for presentation purposes to arbitrarily set the average of our entire data set to 1.0 (the units being of order ppm). All of our "good" runs are plotted, i.e. those runs that came after we fixed a major systematic error in the Pockel Cell set-up which affected the first week of running; those data will require substantial corrections. Blinding is a standard methodology used for parity experiments in which we add to the asymmetry a blinding factor which is an unknown offset of order 1σ, which remains until all the analyses of systematic errors and normalization factors have been completed. We anticipate unblinding (removing the offset to find the final result) sometime in the Spring of 2011.

The new room-temperature septum magnets worked well. The survey reports and auxiliary measurements showed that the geometry downstream of the target was correct at the 1 mm level, which is adequate. A problem found after the experiment was that the septum magnet setting was too low; we ran at 729 A, but 775 A would have been better. Figure 46 (left) shows the angle distribution of the data compared to simulation, where the simulation was performed at the correct septum field integral. Nilanga Liyanage and his student Kiadtisak Saenboonruang analyzed the PREX optics data without the offset correction to the central hole; this way one can see the entrance angle into the HRS by back-tracking using matrix elements from a standard HRS experiment. This was done for the RHRS only because for the left the VDCs had been moved and not properly seated prior to our run. It was found that the deflection by the septum field was ∼5 mrad less than expected, meaning we were losing 5 mrad on the small-angle side of the acceptance.

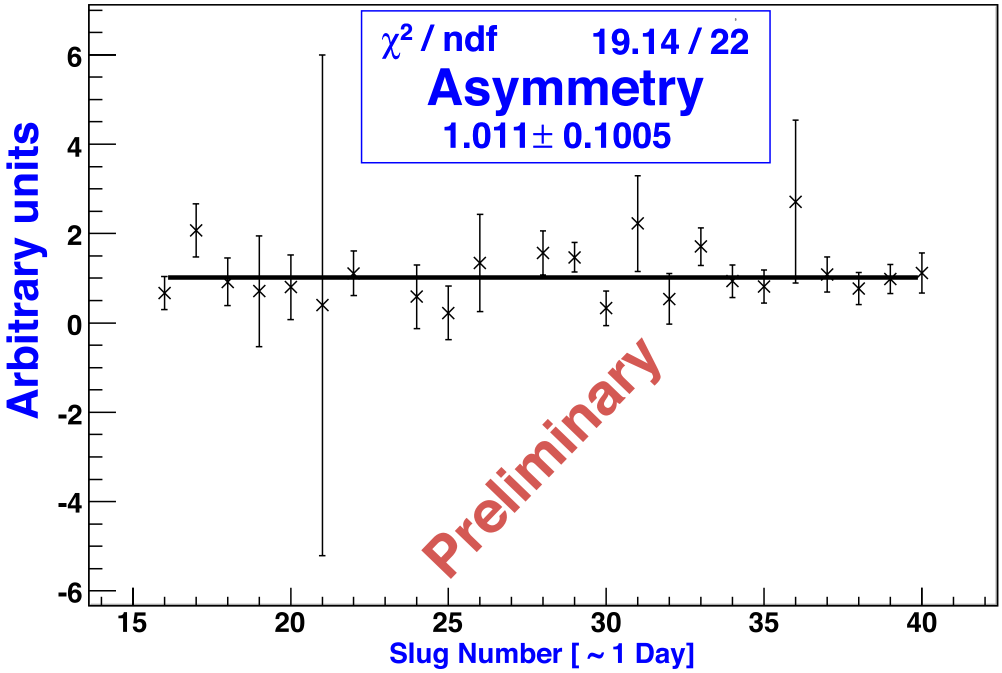

Figure 43: The slug plot for PREX asymmetry. This is the combination of data from figs 44 and 45, i.e. shifted to an average of 1.0 (units are approximately ppm). Each slug is ∼1 day of running and represents a flip of the half-wave plate or Wien filter. The data have been sign-corrected for the product of half-waveplate and Wien filter. The χ^2/dof is reasonable, i.e. the data behaves statistically.

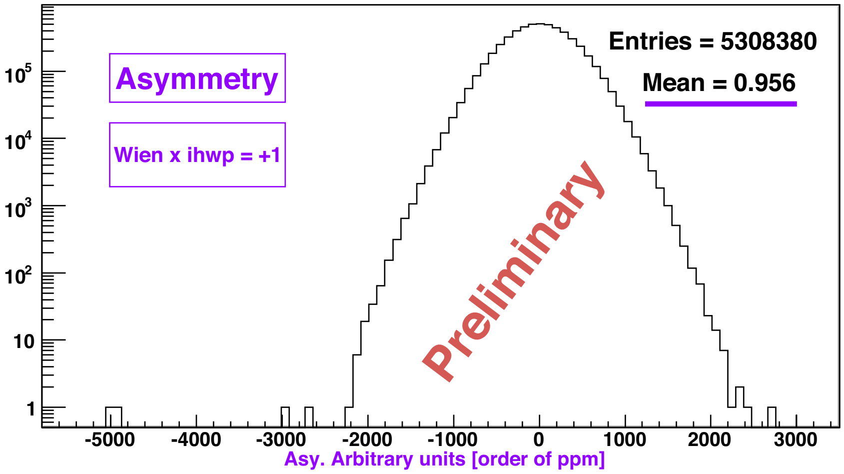

Figure 44: Shifted, blinded asymmetry for PREX in 2010 for a positive product of half-waveplate and Wien filter (the two ways of flipping the sign). For this preliminary result, the data have been shifted by a small amount such that the average of the entire experiment appears at 1.0. The units are on the order of parts-per-million (ppm). The data is a fairly clean Gaussian over 6 orders of magnitude. Outliers have not been suppressed by the choice of X-axis.

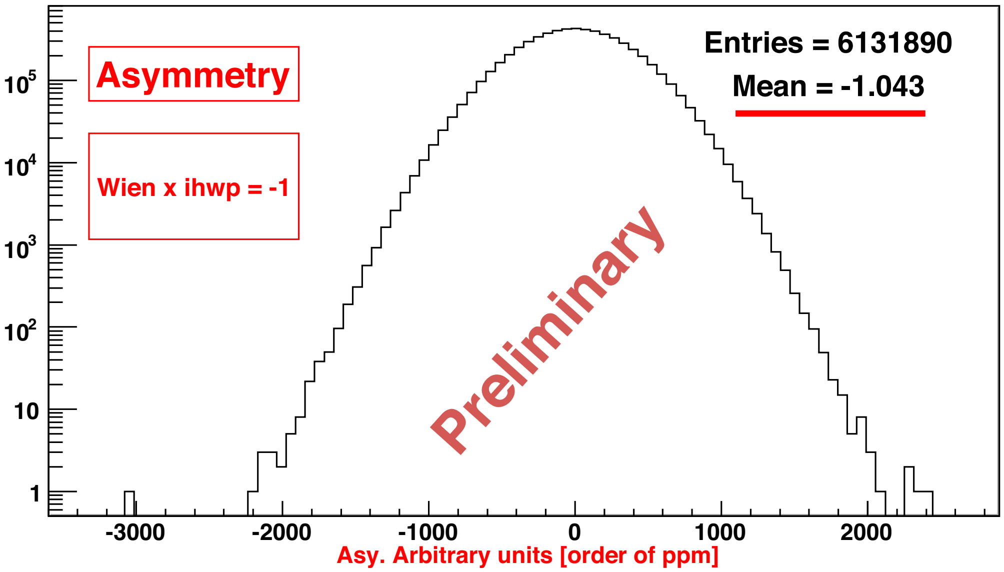

Figure 45: Same as figure 44 except for a negative product of half-waveplate and Wien filter. The sign should flip, and it does.

This conclusion was in agreement with the observed discrepancy between data and MC (see the right panel of Fig. 46). An analysis of the septum current scan shows we could have gotten the full acceptance at the correct Q^2 by running the septa at 775 A together with moving the PREX detector to one side (in Y) by 2.5 cm. We will be better prepared to adjust the setup if we run again.

A major concern was developing a Pb target that could operate at high beam currents without melting. We successfully accomplished this to beam currents exceeding 70 μA; however, we observed a new problem, namely that the thickness of the target became non-uniform, resulting in unacceptable degradation of our pulse-pair width and thus our instantaneous statistical precision, due to use of a raster. During the run, we took over the raster electronics and developed a precision lock for the raster which completely eliminated the noise. For a future run (25 PAC days, discussed below) we envision having 8 targets, four of which use diamond to sandwich lead, and another four that use carbon instead of diamond because graphite is more robust than diamond.

A new "double-Wien filter" has been fabricated and installed at the injector beam line in Jan 2010 by the Polarized Injector Group (Joe Grames, *et al.*). This device allowed us to flip the helicity (about once a week) using an arrangement of solenoids that, to a good approximation, flip the helicity without changing any other parameter of the beam. This is important for understanding and canceling subtle higher-order effect in the asymmetry such as a possible helicity-correlated change in the spot size. The Qweak experiment is also benefiting from this new device.

We were concerned about possible systematic errors resulting from the product of transverse polarization of the beam and vector analyzing power for transverse asymmetry in elastic e-^{208}Pb scattering. Two important findings during the run eliminated this problem. First, the transverse asymmetry was measured to be less than 2 ppm. Second, we were able to find a location in the HRS focal plane to place an auxiliary detector which is sufficiently sensitive to a transverse asymmetry, due to higher-order terms in the HRS.

The Compton and Møller polarimeters, which will be discussed elsewhere in the annual report, made major advances, allowing us to achieve a ∼1.5% accuracy in beam polarization during the run. Incremental improvements in a follow-up run should allow us to approach the 1% level.

To improve our measurement of Q^2 in the high-rate environment of forward elastic scattering from Pb, new electronics for low-current (nA) operation of the cavity position monitors were developed and new GEM detectors were deployed and tested to cross-check the VDCs.

Using a more optimal setting of the septum magnet and a slightly lower energy we can project the accuracy of a future run. In figure 47 we show how the rate varies with the septum current and Q^2. As

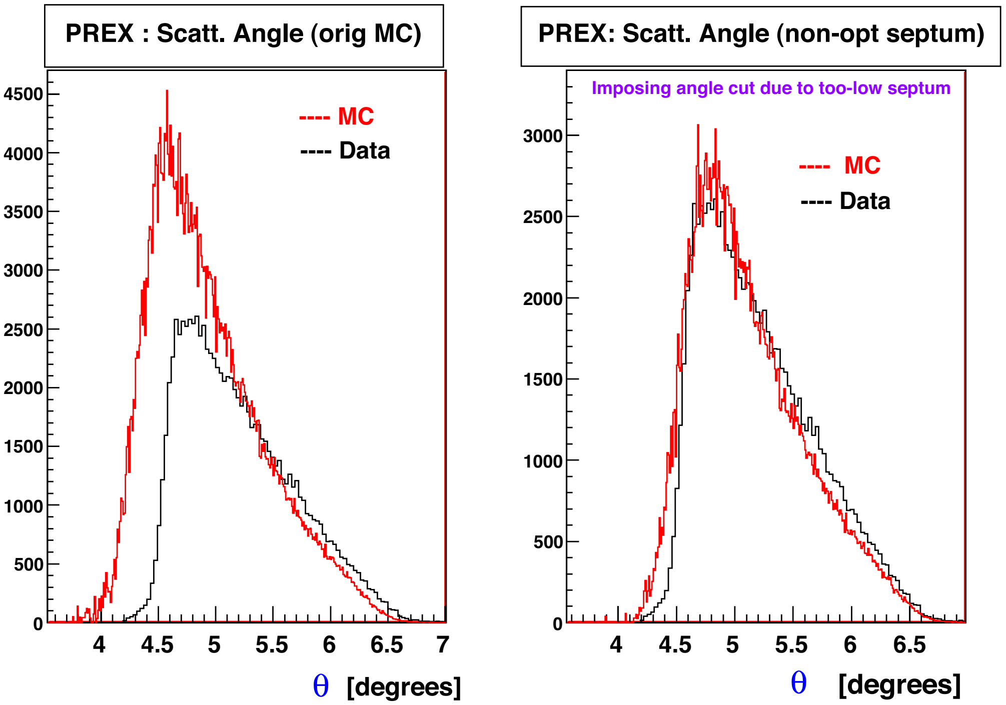

Figure 46: Simulated and reconstructed scattering angle. The data are compared to the original simulation (left) and a corrected simulation (on the right), where the correction takes into account that the septum current was set too low by 5% such that the scattering angle cutoff was too high by ∼4 mrad.

explained in the proposal, the optimum kinematics is one that minimizes the error in R_N. The result of this optimization procedure is shown in fig 48. Note that both the asymmetry and the sensitivity to R_N grows with Q^2, and the rates drop with Q^2. This means that for the optimal Q^2 range we want to run at the higher end of Q^2 because all three factors tend to minimize the systematic error. For a 30 PAC-day run, the total error in R_N will be 1.2% including a beam polarimetry error of 1.5% which was achieved in the 2010 run. If the polarimetry error is further improved, the error in R_N can be 1.0%. Considering that we already have ∼5 PAC days of good data, we have requested 25 more PAC days to complete the experiment.

To ensure the success of a follow-up run, a significant amount of engineering and physicist effort will be required to redesign the beam line, vacuum system, and radiation hardness of the experiment. The beam line immediately downstream of the scattering chamber must be designed to withstand a large radiation dose. Careful choices of materials will have to be made, especially for vacuum seals. The challenge is not only radiation hardness but also durability due to significant thermal cycling. The collimation immediately downstream of the target must be revisited and the need for water cooling must be investigated. Once the beam line and collimation have been redesigned, a careful estimation of the sources of radiation and the total electromagnetic and neutron fluxes that might impact the HRS electronics and controls must be made. A comprehensive local shield "hut" might have to be designed in order to contain the radiation close to the beam line and avoid such radiation from reaching other parts of the Hall.

References

[1] T.W. Donnelly, J. Dubach, and I. Sick, Nucl. Phys. A**503**, 589 (1989).

[2] C. J. Horowitz, Phys. Rev. C **57**, 3430 (1998).

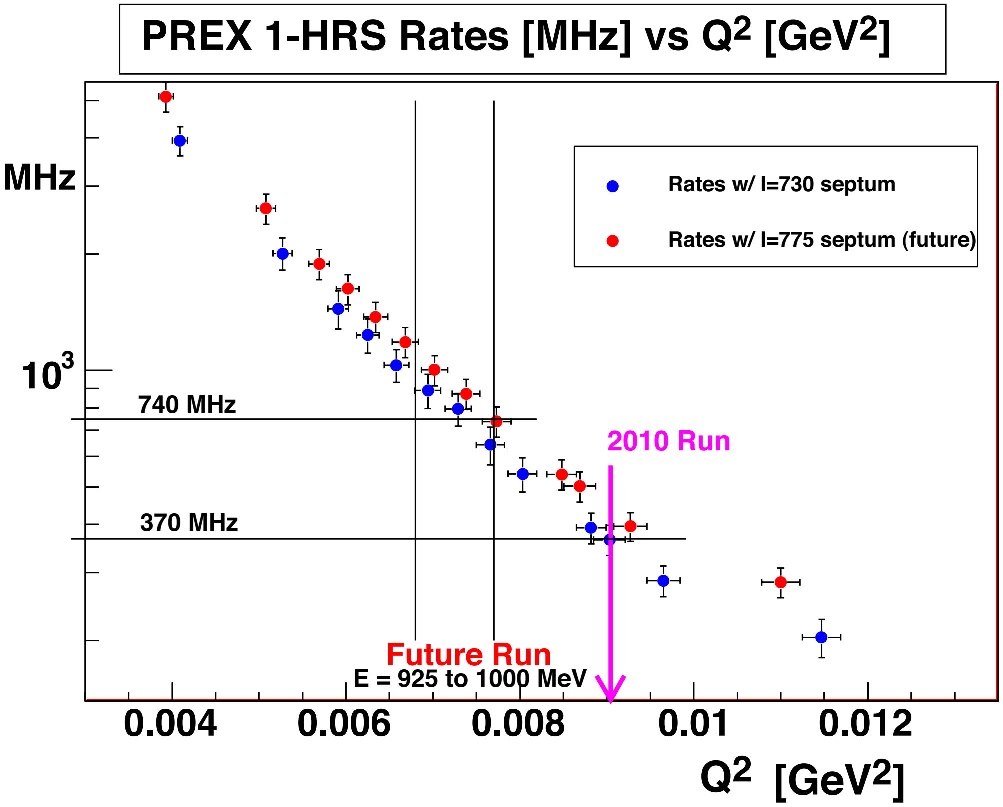

Figure 47: Simulated rates in one HRS versus Q^2 for two assumptions about septum current setting. For I=730 A (2010 run) the minimum scattering angle was 4.58° and was not optimal. For I=775 A (suggested future run point) the min angle will be 4.35°. By putting the septum there and reducing the energy to the range 925 to 1000 MeV, we expect to double the rate.

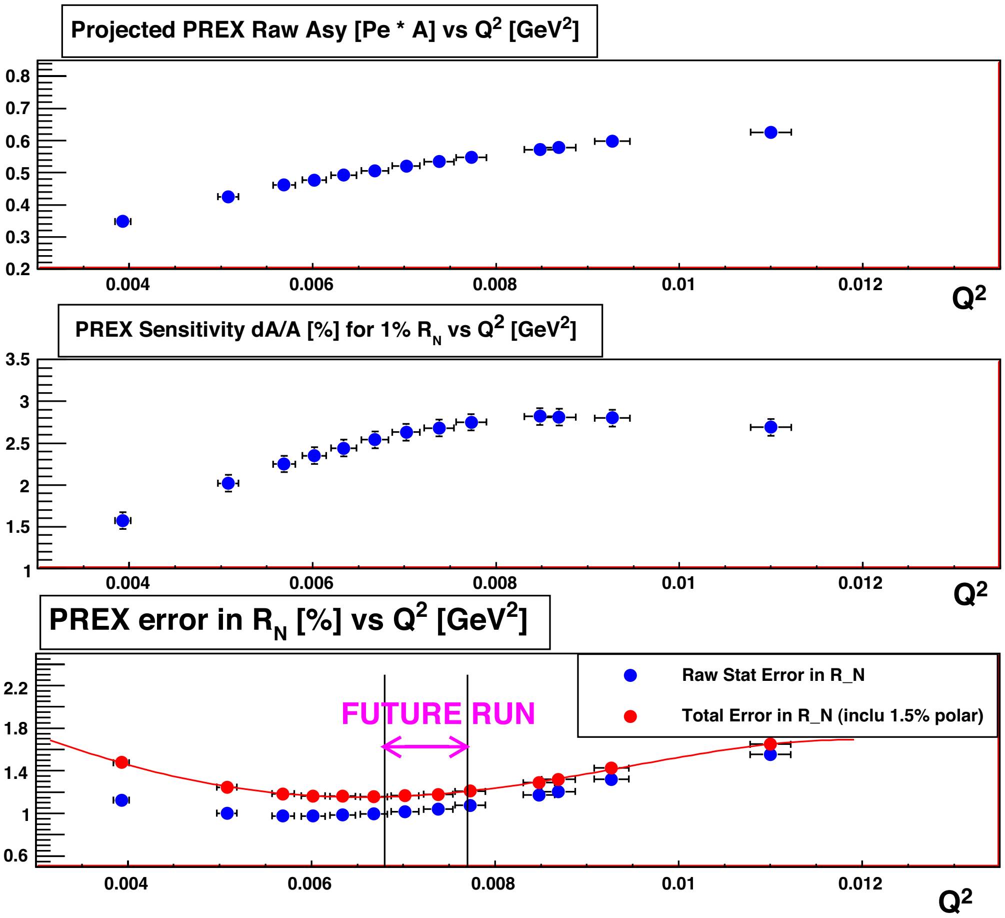

Figure 48: The raw asymmetry, sensitivity to R_N, and error in R_N as functions of Q^2 for the correct septum current (I=775 A). We'll want to run at an energy between 925 and 1000 MeV, which provides a statistical error in R_N of 1% in 30 days at 70μA.

3.6 E05-015

Measurement of the Target Single-Spin Asymmetry in Quasi-Elastic $^3\mathbf{He}^{\uparrow}(e, e')$

T. Averett, J.P. Chen and X. Jiang, spokespersons,
and
the Hall A Collaboration,
contributed by B. Zhao

3.6.1 Introduction

In the study of electron scattering in the past forty years, the one-photon exchange process was considered to be the dominant one, while two-photon exchange was assumed to provide a negligible contribution. However, with the new precision data available, it was found that two-photon exchange played an important role in some measurements, like the ratio of $\mu_p G_{E_p}/G_{M_p}$ [1].

The target single-spin asymmetry from inclusive electron scattering on a target polarized perpendicular to the scattering plane, A_y, is expected to be zero in the one-photon exchange approximation due to time-reversal invariance in elastic scattering. In recent calculations, A_y is expected to be non-zero from the interference between the single-photon exchange amplitude and the imaginary part of the two-photon exchange amplitude [2].

In another approach, it was recently shown that A_y is directly related to moments of the Generalized Parton Distributions (GPDs) [3]. A precise measurement of A_y will provide important information on the nucleon response during the two-photon exchange and will provide a new experimental constraint on GPD model input. However, a non-vanishing A_y has never been clearly observed in the past. This experiment E05-015 will clearly establish a non-zero A_y for the first time.

3.6.2 Experiment overview

This experiment E05-015 was run from April 24 to May 12 in 2009. Both Hall-A Left-arm High-Resolution Spectrometer (LHRS) and Right-arm High-Resolution Spectrometer (RHRS) were used to detect electrons. This meant that two sets of data were collected (left and right) at the same time, which allowed a cross-check of the A_y measurement and also provided a good estimate of the final systematic uncertainty caused by the spectrometers. In addition to this estimation of the systematic uncertainty, the important scalars, for example, trigger scalars, charge scalars, were also sent to the LHRS and RHRS. During the experiment, the left-arm and right-arm runs were synchronized to the same run time. The consistency of a scalar between left-arm reading and right-arm reading is a powerful proof of no false asymmetry for this A_y measurement.

The experimental data were collected in three different Q^2 kinematic regions, listed in the following Table 8, and about 100 million events for each Q^2 point to achieve $\sim 10^{-4}$ statistical uncertainty.

Table 8: E05-015 kinematics setting.

E_0(GeV)	E'(GeV)	θ_{spec} (Deg)	Q^2 (GeV^2)	$\lvert q\rvert$ (GeV)	θ_q (Deg)
1.25	1.22	17	0.13	0.359	71
2.43	2.18	17	0.46	0.681	62
3.61	3.09	17	0.98	0.988	54

3.6.3 Analysis

After the optics calibration (new database from Ge Jin) and detector calibrations, the raw experimental data were processed with Hall-A standard analysis software (ANALYZER) and saved in format of rootfiles for later analysis.

The Hall-A High-Resolution Spectrometers have provided a stable particle identification for many years. Moreover, the pion background was small in this quasi-elastic scattering experiment, so it was easy to identify good electrons using the Cerenkov Counter and the lead-glass calorimeter. However, it was a challenge to check the consistency of the scalars at the $\sim 10^{-4}$ level. For this purpose, for each type of scalar, the gated one (depending on the target spin state) and the ungated one from the LHRS were compared with those from the RHRS. The most stable one was then used to calculate the life time, charge and other variables. In this analysis, data taken during frequent beam trips were eliminated. The data were also discarded if the difference of a scalar between the two arms was $> 10^{-4}$.

The target analysis was done by Yawei Zhang, including the target density and polarization and the nitrogen dilution factor.

3.6.4 Results

The preliminary target single-spin asymmetry at $Q^2 = 0.98$ GeV^2 is shown in Fig. 49. As mentioned in section 3.6.2, the scattered electrons were detected on both sides of the beam line (LHRS and RHRS), so the target single-spin asymmetries calculated from left-arm data and right-arm data should have opposite sign due to the opposite scattering angles. In Fig. 49, the sign of asymmetry was flipped between left-arm data and right-arm data, which clearly indicated that the target single-spin asymmetry was non-zero. The analysis of the other two kinematic settings are ongoing and will be released soon.

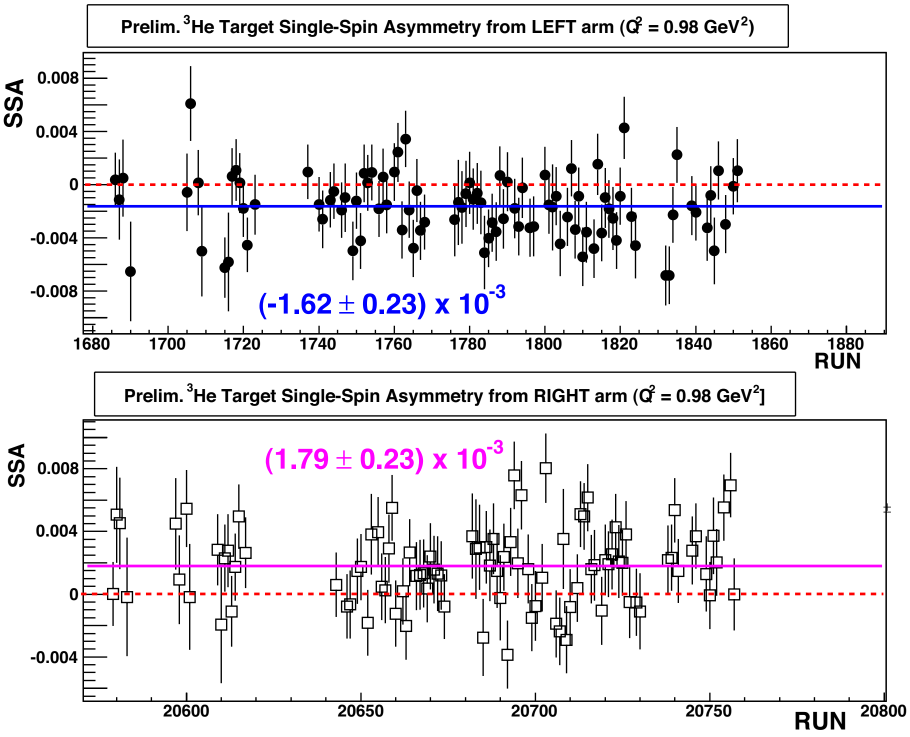

Figure 49: The preliminary ^{3}He target single-spin asymmetry from left-arm data (top plot) and right-arm data (bottom plot) at $Q^2 = 0.98$ GeV^2. The red dashed lines indicate the zero value. The solid lines indicate a constant fit to the target single-spin asymmetry of each run (blue: left-arm; pink: right-arm).

References

[1] J. Arrington, Phys. Rev. C **68**, 034325 (2003).

[2] A. Afanasev *et al.*, hep-ph/0208260.

[3] Y.C. Chen *et al.*, Phys. Rev. Lett. **93**, 122301 (2004).

3.7 E08-027

A. Camsonne, J.P. Chen, D. Crabb, K. Slifer, spokespersons,
and
the Hall A Collaboration,
contributed by K. Slifer

3.7.1 Introduction

The inclusive-scattering spin-structure functions g_1 and g_2 are fundamental spin observables which characterize the deviation of the nucleon's spin-dependent properties from point-like behavior. Historically, measurements of g_1 provided direct tests of QCD via the Bjorken sum rule, and also revealed that only a small fraction of the nucleon spin is carried by that of the valence quarks. In general, measurement of the spin structure functions (SSF) allow insight into QCD via sum rule predictions, provide benchmarks for chiral perturbation theory (χPT) and lattice gauge theory calculations, and are needed to quantify higher-twist effects and quark-hadron duality.

Recently, it has become apparent that poor knowledge of the SSFs (which are purely QCD quantities) at low Q^2 limits the precision of QED calculations of simple bound systems, such as the hydrogen-like atom [1, 2]. Energy levels in these systems can be measured to fantastic precision. As a result, the corresponding QED calculations have been pushed to a level where the finite size of the nucleon, as characterized by the structure functions and elastic form factors (FF), has become a leading uncertainty. Of particular interest, researchers from PSI [2] have obtained a value for the proton charge radius $\langle R_p \rangle$ via measurements of the Lamb shift in muonic hydrogen, which differs significantly from the value from elastic electron-proton scattering. The deviation in $\langle R_p \rangle$ would have many troubling consequences, such as requiring a sizable shift in the fundamental Rydberg constant, so all aspects of the PSI calculations are being re-examined. The main uncertainties in the PSI results originate from the proton polarizability and from the Zemach radius. These quantities are determined from integrals of the SSF and elastic form factors, which due to kinematic weighting, are dominated by the low Q^2 region. It is prudent to question whether these uncertainties are underestimated, since g_2^p is largely unmeasured, and g_1^p data extend only down to $Q^2 \approx 0.05$ GeV^2. The Zemach radius, is similarly dominated by the low Q^2 behavior of the proton elastic form factors G_E and G_M.

At low and moderate Q^2, data on the g_2^p structure function are conspicuously absent. The lowest momentum transfer that has been investigated is 1.3 GeV^2 by the RSS collaboration [3]. The absence of g_2^p data is also unsatisfying in light of the intriguing results found in the transverse neutron data: The SLAC E155 collaboration found their data to be inconsistent with the proton Burkhardt-Cottingham (BC) sum rule at $Q^2 = 5.0$ GeV^2, while the JLab E94-010 collaboration found that the neutron BC sum rule held below $Q^2 = 1.0$ GeV^2. Even more compelling, it was found that state-of-the-art next-to-leading order χPT calculations are in agreement with data for the generalized spin polarizability γ_0^n at $Q^2 = 0.1$ GeV^2, but exhibit a significant discrepancy [4] with the longitudinal-transverse polarizability δ_{LT}^n. This is surprising since δ_{LT} was expected to be more suitable than γ_0 to serve as a testing ground for the chiral dynamics of QCD [6, 7] due to it's relative insensitivity to resonance contributions. It is rare to find such striking disagreement with theory, and g_2^p data at low Q^2 will be invaluable in establishing the reliability and range of χPT. As discussed above, lack of knowledge of the g_2^p structure function at low Q^2 is also one of the leading uncertainties in calculations of the hyperfine splitting of the hydrogen atom [1], and the Lamb shift in muonic hydrogen [2]. In particular, the g_2^p contribution to these calculations is dominated by the region below 0.4 GeV^2 where no data currently exists and where E08-027 will measure.

3.7.2 The Experiment

E08-027 was approved by PAC33 with A$^-$ rating to run in JLab's Hall A. We will perform an inclusive measurement at forward angle of the proton spin-dependent cross sections in order to determine the g_2^p structure function and the longitudinal-transverse spin polarizability δ_{LT} in the resonance region for $0.02 < Q^2 < 0.4$ GeV^2. To reach the lowest possible momentum transfer, a pair of room temperature septum

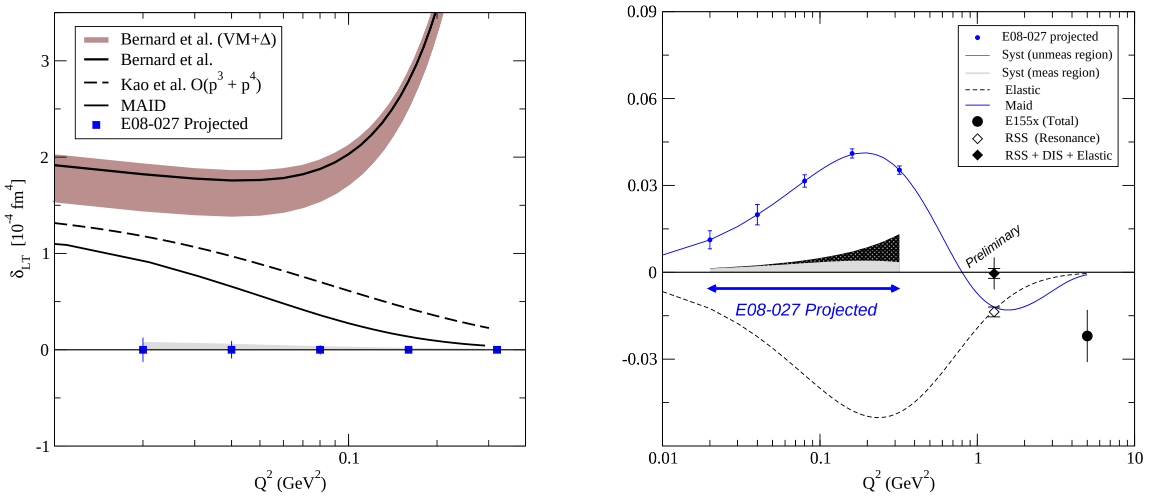

Figure 50: **Left:** Projected uncertainties for δ_{LT}. χPT predictions from Bernard *et al.* [6], and Kao *et al.* [7]. **Right:** Projected uncertainties for $\Gamma_2^p(Q^2)$. The light and dark bands on the horizontal axis represent the experimental systematic, and the uncertainty arising from the unmeasured ($x \to 0$, $x = 1$) contributions to Γ_2, respectively.

magnets will be used to allow detection of scattered electrons at 6°. Dynamical Nuclear Polarization (DNP) will be used to polarize a solid ammonia target maintained in a liquid helium bath at 1 K in a 5 T field. This will represent the first use of a DNP target in Hall A. See Fig. 50 for the expected uncertainties on the spin polarizability δ_{LT} and the first moment of g_2.

E08-027 complements two other related experiments : EG4 which will measure the proton g_1 structure function, and E08-007 which will measure the proton form factor ratio G_E/G_M in the same kinematic region as E08-027. Together, these experiments will provide definitive measurements of the proton structure at low Q^2. Because of the similarities in technique and equipment, the E08-027 and E08-007 collaborations are highly cooperative and the two experiments will run simultaneously. E08-007 will focus on elastic scattering, while E08-027 measures the inelastic data. Installation begins in May 2011, and the experimental run will extend into 2012.

References

[1] V. Nazaryan, C. E. Carlson and K. A. Griffioen, Phys. Rev. Lett. **96**, 163001 (2006).

[2] R. Pohl *et al.*, Nature **466**, 213 (2010).

[3] F. R. Wesselmann *et al.* [RSS Collaboration], Phys. Rev. Lett. **98**, 132003 (2007).

[4] M. Amarian *et al.* [Jefferson Lab E94010 Collaboration], Phys. Rev. Lett. **93**, 152301 (2004).

[5] K. Slifer *et al.* [Resonance Spin Structure Collaboration], Phys. Rev. Lett. **105**, 101601 (2010).

[6] V. Bernard, T. R. Hemmert and U. G. Meissner, Phys. Lett. B **545**, 105 (2002).

[7] C. W. Kao, T. Spitzenberg and M. Vanderhaeghen, Phys. Rev. D **67**, 016001 (2003).

3.8 E06-010 Transversity

Measurement of Single Target-Spin Asymmetry in Semi-Inclusive Pion Electroproduction on a Transversely Polarized ^{3}He Target

J.-P. Chen, E. Cisbani, H. Gao, X. Jiang, J.-C. Peng co-spokespersons,
and
the Hall A Collaboration

contributed by K. Allada, J. Huang, X. Jiang, A. Puckett, X. Qian, Y. Qiang, V. Sulkosky and Y. Zhang

3.8.1 Introduction

Experiment E06-010 [1] collected data in Hall A from Oct. 2008 to Feb. 2009 using a transversely polarized ^{3}He target in order to measure the target single-spin asymmetries (SSA) in $^3\text{He}(e, e'h)$ reaction (where $h = \pi^+, \pi^-, K^+$ or K^-). The BigBite spectrometer was set at 30° on beam right to detect scattered electron with $0.8 < E' < 2.2$ GeV, the left HRS was used on beam left to detect the fragmented hadron in coincidence at $p_h = 2.35$ GeV/c and 16°. The goal of this experiment is to extract the Collins and Sivers single-spin asymmetries in semi-inclusive DIS reactions on the neutron (^{3}He) in order to constrain quark transversity (quark transverse spin) and the quark Sivers distributions, which reflect the correlation between the quark's transverse momentum and the nucleon's transverse spin.

Recently, the COMPASS experiment [2] published Collins and Sivers SSA results on a transversely polarized proton target. While the proton Collins asymmetry of COMPASS, which is clearly non-zero, is consistent with that measured by HERMES [3], the Sivers asymmetry is smaller than those of HERMES [4] but non-vanishing.

Major progress has been made in the data analysis of experiment E06-010:

- The preliminary ^{3}He Collins and Sivers asymmetries have been released in the summer of 2010.
- The preliminary ^{3}He double-spin A_{LT} asymmetry has also been released in the summer of 2010.
- Significant progress has been made in determining the ^{3}He and N_2 density in the target chamber and ^{3}He to neutron dilution factors, as documented in this report.

Three Ph.D. theses were defended on experiment E06-010: Dr. Xin Qian (Duke, May 2010), Dr. Kalyan Allada (Kentucky, May 2010) and Dr. Chiranjib Dutta (Kentucky, May 2010). In addition, Dr. Joe Katich (William and Mary, Sept. 2010) defended his thesis on the inclusive ^{3}He target single-spin asymmetry in the DIS reaction with data taken parasitically during E06-010. At the time of this report, we are working on two paper drafts on the Collins and Sivers SSA and on the double-spin asymmetry (DSA) A_{LT}.

3.8.2 Summary of Pressure Curve Analysis in E06-010

In experiment E06-010, a high-pressure polarized ^{3}He gaseous target was used as an effective polarized neutron target to measure the Single-Spin-Asymmetry (SSA) of the neutron. This target had a 2-chamber structure as shown in Fig. 51. In the top chamber (also referred to as the pumping chamber), the ^{3}He nuclei were polarized with spin-exchange optical pumping (SEOP) [5]. The polarized ^{3}He nuclei diffuse to the bottom chamber (also referred to as the target chamber), where the electron beam passes through (red line in Fig. 51). For SEOP, the pumping chamber needed to be heated to about 250 °C, while the typical temperature of the target chamber was between 40°C to 120°C. This large temperature difference led to a non-uniform density distribution of the gas inside the cell. In the analysis, the effective density seen by the electron beam was calculated with the temperature information measured by RTDs using a temperature distribution model. The model calculation was checked with the dedicated pressure curve data taken with the first pass electron beam (1.236 GeV). In addition, a small amount of N_2 gas was filled into the cell in order to maintain the polarization of ^{3}He. The pressure curve data can also be used to extract the N_2 to ^{3}He ratio.

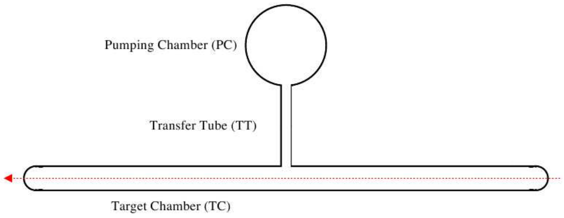

Figure 51: Schematic view of the ^{3}He glass cell

During the experiment, data were taken with a reference cell filled with different amounts of ^{3}He gas and ^{14}N gas. The left high resolution spectrometer (LHRS) was set at the elastic kinematics to detect the elastically scattered electrons. The measured yields were then compared with that of the production cell in order to calculate the density of the gas in the production cell. Various corrections, which include single-track efficiency, radiative corrections and cell-wall contamination, were taken into account in the analysis.

Yield Extraction

The raw data was first skimmed following the standard data-quality check procedure [6], in which the beam trip and other instrumental issues were removed. Charge C, which is the average of the signals from BCM u3 and d3, and computer live time L_t, defined as

$$L_t = \frac{N_{t3}}{S_{t3} - S_{edtp}}, \tag{18}$$

are calculated for the remaining good data. Here, S_{t3} stands for the number of T3 scaler counts, N_{t3} stands for the number of T3 events [8] and S_{edtp} represents the number of pulser scaler counts.

After skimming, several cuts were used to select good events.

- T3 event only
- standard LHRS acceptance cut [7]
- standard LHRS electron cuts [8]
- vertex-Z cut [9].

To identify the e-^{3}He and the e-N events, the missing-mass cuts are defined separately as shown in Fig. 53 and Fig. 54. In the ^{14}N case, we also included its first excited state to obtain enough statistics.

The extracted yield is then defined as:

$$Y^{raw}_{^3\mathrm{He}} = \frac{N_{^3\mathrm{He}}}{C \cdot L_t \cdot E_{single-track}} \tag{19}$$

$$Y_{^3\mathrm{He}} = Y^{raw}_{^3\mathrm{He}} \cdot (1 - R_{\mathrm{N}/^3\mathrm{He}} \cdot \frac{\rho_{\mathrm{N}_2}}{\rho_{^3\mathrm{He}}}) \tag{20}$$

$$Y_{\mathrm{N}} = \frac{N_{\mathrm{N}}}{C \cdot L_t \cdot E_{single-track}} \tag{21}$$

Here, $N_{^3\mathrm{He(N)}}$ stands for the number of good elastic events after all the cuts. $E_{single-track}$, which is defined as the ratio of number events with exactly 1 track to that of events with at least one track:

$$E_{single-track} = \frac{N_{t3\&exactly-1-track}}{N_{t3\&at-least-1-track}}, \tag{22}$$

---

[8] T3 is the name of single arm HRS trigger.

[9] In standard analysis the vertex Z cut is ±16.5 cm. Here, we chose the range as $[-15, -5] \cup [0, 10]$ cm to exclude the contamination of the glass cell window, excluding the range $(-5, 0)$ cm, where the wall thickness of the glass cell is not uniform, as shown in Fig. 52.

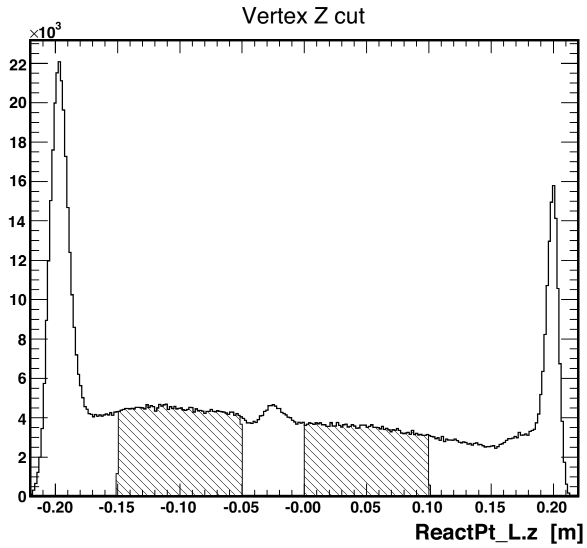

Figure 52: Vertex Z cut for the production cell. Only the shadowed region is selected.

is the single track efficiency (shown in Fig. 55), since we require the good event only contains one good track. Then we extract the yields of the reference cell ^{3}He runs as shown in Fig. 56 using Eq. 20.

In extracting the yield of ^{3}He from the production cell, the contamination from the N_2 needs to be subtracted. In Eq. 20, $R_{\mathrm{N}/^3\mathrm{He}}$ represents the ratio of number of events from ^{14}N and ^{3}He at the same density, and the ratio $\frac{\rho_{\mathrm{N}_2}}{\rho_{^3\mathrm{He}}}$ gives the density ratio of N_2 and ^{3}He in the production cell.

Simulation and Radiative Correction

In order to compare the yields from the reference cell to those from the production cell, radiative corrections need to be taken into account, since the wall thickness of the two cells are slightly different. In addition, since the temperature distributions in the reference and production cell are different, a vertex position dependent correction is also required. Both corrections are calculated using a Monte-Carlo simulation.

The simulation program used is SAMC [9]. Tables 9 and 10 show the materials the incident and scattered electrons pass through, respectively. Table 11 shows the average A (average number of nucleons), Z (average number of proton), density and effective radiation length for incident and scattered electron.

Description	Material	Thickness
Beam window	Beryllium	0.254 mm
^{4}He in target enclosure	He	31.6 cm at 1 atm
Cell window	GE180	0.142 mm (reference) 0.123 mm (production)
^{3}He in cell	^{3}He	20 cm; various pressure (reference) 10 atm (production cell)

Table 9: Table of materials traversed by an incident electron in the reference and the production cells.

Figure 57 shows a comparison of the missing-mass spectrum of the simulation (red) and the data (black). Here, the simulation has been scaled to that of the data for comparison. The applied elastic cut is shown as the two blue lines. In addition, an additional width of 480 keV was directly applied on the simulated missing-mass spectrum to incorporate the detector resolution. This 480 keV smearing is in general consistent with the estimated detector resolution from the HRS optics calibration [8]. As shown in Fig. 58, a choice of different smearing parameters (400 keV and 550 keV) leads to negligible effects on the results.

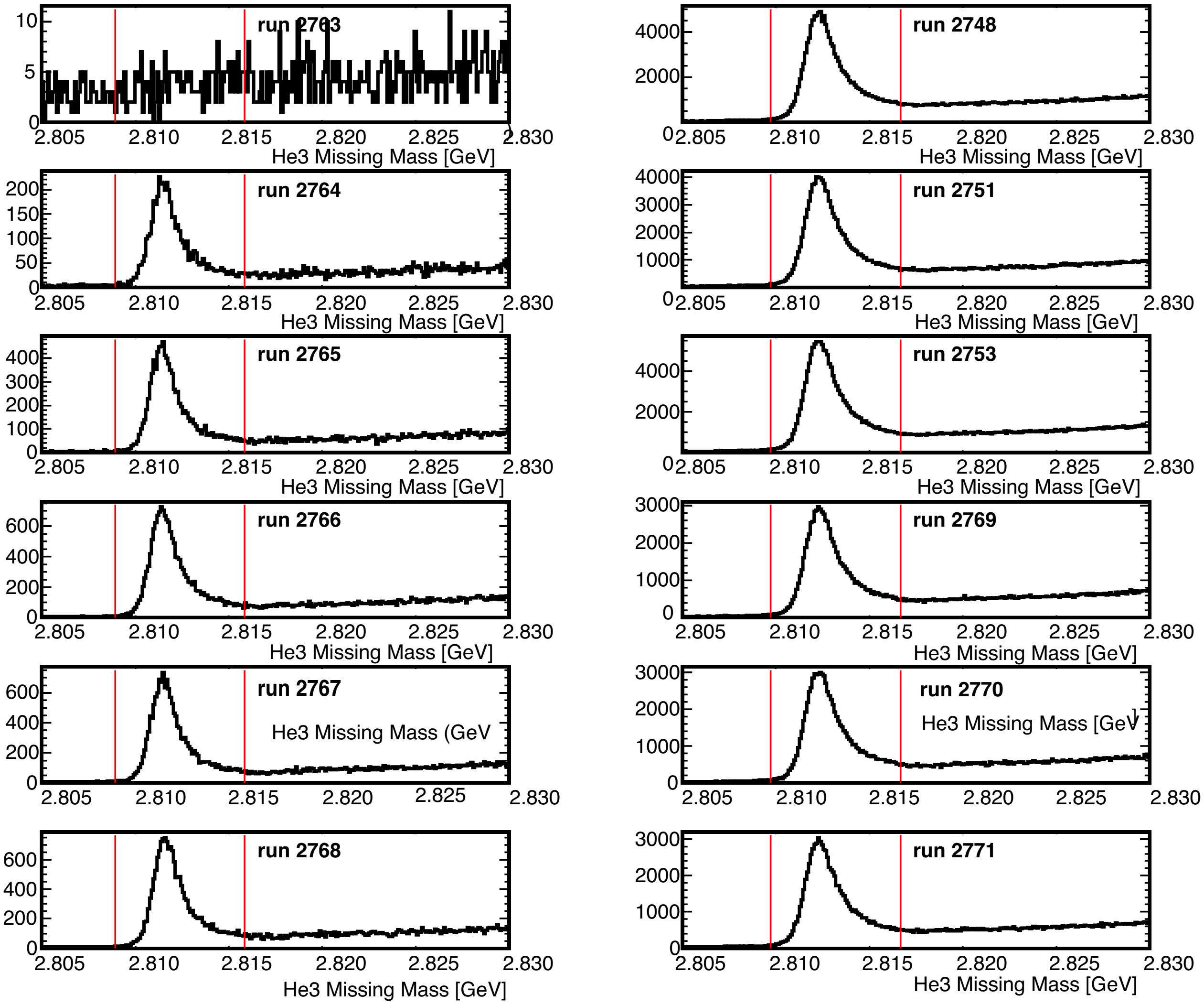

Figure 53: ^{3}He missing-mass spectrum of the reference-cell runs (left column) and the production-cell runs (right column). The ^{3}He elastic cuts are defined as the range between the two red solid lines. For reference cell runs the range is $[2.80893, 2.81586]$ GeV, while for production cell runs it is $[2.80973, 2.81666]$ GeV.

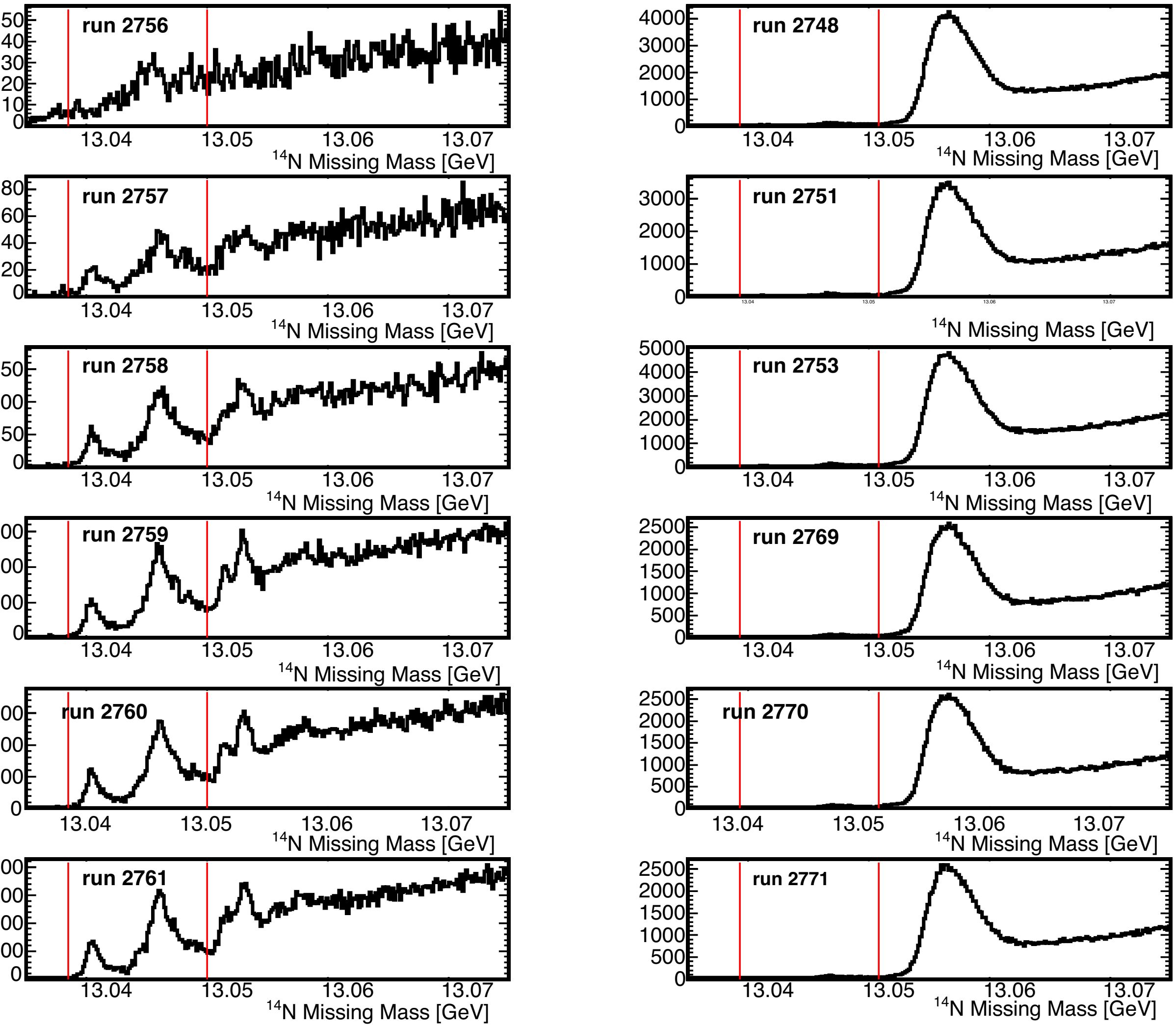

Figure 54: ^{14}N missing-mass spectrum of the reference-cell runs (left column) and the production-cell runs (right column). The ^{14}N elastic cuts are defined as the range between the two red solid lines. For the reference cell runs the range is $[13.0385, 13.05]$ GeV, while for the production cell runs it is $[13.0393, 13.0508]$ GeV.

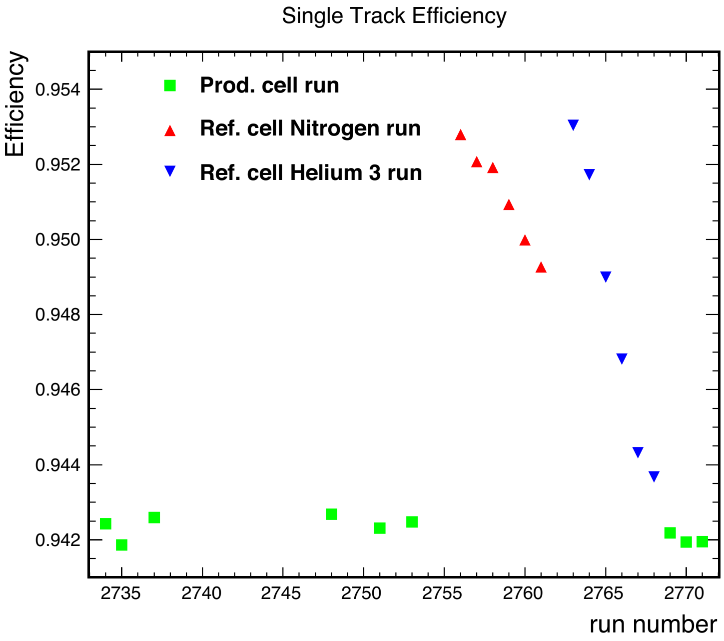

Figure 55: Single-track efficiency for each run. As the T3 rate mainly comes from the background, on which the single-track efficiency depends, this efficiency shows a weak dependence of the gas pressure in the target cells.

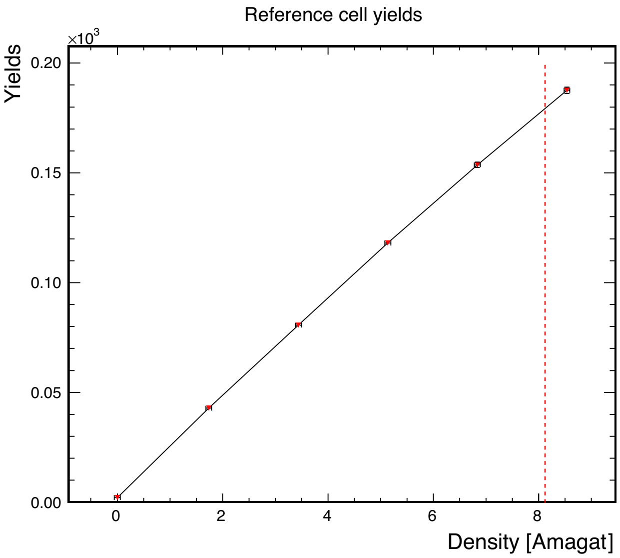

Figure 56: Yield vs. density for the reference-cell ^{3}He runs. The red dashed line represents the filling density of the production cell.

Vertex Correction

In the simulation, the events are uniformly generated through the entire target length. However, this is not the case in the experiment due to a non-uniform temperature distribution. In order to take this effect into account, each event is weighted by the density ratio $\rho(z)/\bar{\rho}$ of the calculated to the average density as shown

Description	Material	Reference Thickness	Production Thickness
^{3}He	^{3}He	calculated from pressure gauge	3.63 cm (10 atm)
cell wall	GE180	4.515 mm	6.062 mm
^{4}He in target enclosure	He	45.7 cm (1 atm)	45.7 cm (1 atm)
target enclosure	G11/Fr5	1 mm	1 mm
Air	Air	120 cm	120 cm
LHRS window	Kapton	0.3 mm	0.3 mm

Table 10: Table of materials traversed by a scattered electron in the reference and the production cells.

Material	Density [g·cm^{-3}]	Rad. Length [g·cm^{-2}]	Average A	Average Z
Be	1.85	65.19	9.012	4
Air	0.001205	36.66	14.5477	8.0562
GE180 glass	2.76	19.4246	25.4346	11.346
^{3}He (1 atm)	0.000125	71.07	3.016	2
^{4}He (1 atm)	0.000166	94.32	4.003	2
Kapton	1.42	40.612	9.8034	5.026
G11/Fr5	1.8	30.17	18.94	9.43

Table 11: Properties for all involved materials.

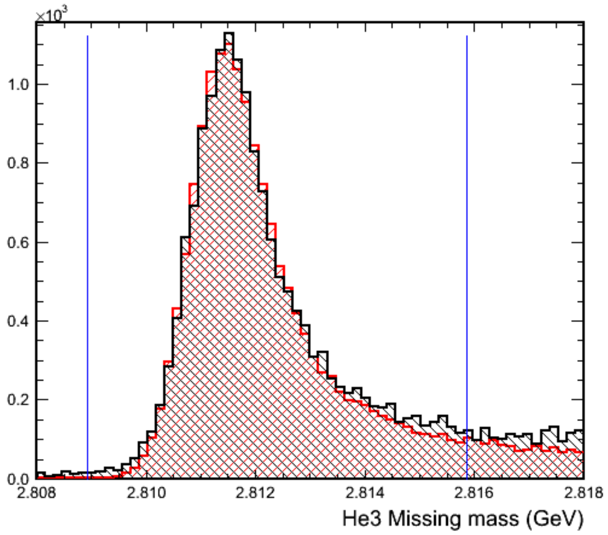

Figure 57: ^{3}He missing-mass spectrum of simulation (red) and data (black). The simulation has been smeared by 480 keV. The contribution at large missing mass, from the inelastic e-^{3}He scattering, has not been included in the simulation.

in Fig. 59 over the entire vertex range of interest. Here, $\bar{\rho}$ is calculated as:

$$\bar{\rho} = \frac{\int \rho(z)dz}{\int dz}. \tag{23}$$

This correction leads to about 0.3% reduction in the yield of the production cell, while it is negligible for the reference cell due to a more uniform temperature distribution. Finally, the ratios between the simulated yield of the reference-cell runs and that of the production-cell runs are shown in Fig. 58.

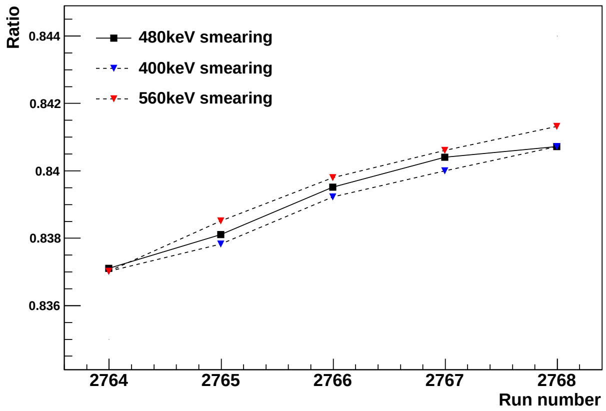

Figure 58: The ratio between the simulated yields of the reference-cell runs and the yields of the production-cell run is shown. The results are compared for different values of the smearing parameter. The effect of a different smearing parameter is negligible.

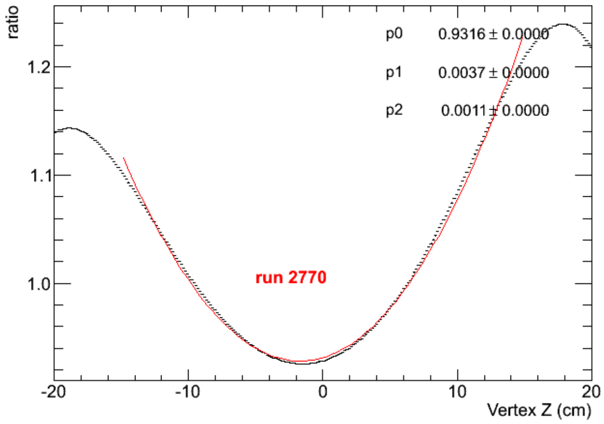

Figure 59: Vertex dependence of the density due to the temperature distribution. The red curve represents a second-order polynomial fit

Pressure Curve

In the pressure curve analysis, the reference cell yields are converted to that of the production cell:

$$Y_{prod}^{ref} = (Y_{ref}^{data} - Y_{ref}^{empty}) \cdot \frac{Y_{prod}^{MC}}{Y_{ref}^{MC}} + Y_{ref}^{empty} \tag{24}$$

Here Y_{ref}^{data} is the yield in Eq. 19 or Eq. 21, depending on whether the cell was filled with ^{3}He or ^{14}N, respectively, extracted from the reference-cell data. $\frac{Y_{prod}^{MC}}{Y_{ref}^{MC}}$ takes into account the radiative corrections and a vertex-dependent density correction from the simulation. Here, Y_{ref}^{empty} is the yield from the empty reference-cell runs calculated using Eq. 19 but with the appropriate normalization factors for these runs. This conversion allows a direct comparison of the yields from the reference cell to those from the production cell.

In addition, it is more useful to plot the yield vs. the density than the yield vs. the pressure. Therefore, the pressure readings (psi) are converted to density (in amagats) by:

$$\rho = \frac{P}{14.696} \cdot \frac{273.15}{273.15 + T}, \tag{25}$$

where T is the effective temperature calculated from the temperature distribution, which was modeled from

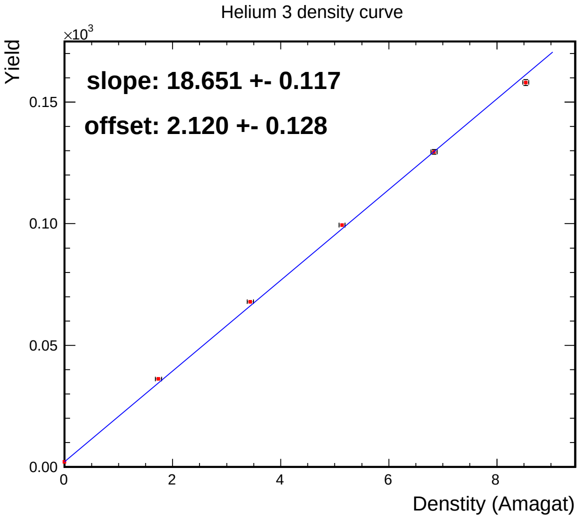

Figure 60: The density curve of the reference-cell ^{3}He runs, fit to a straight line.

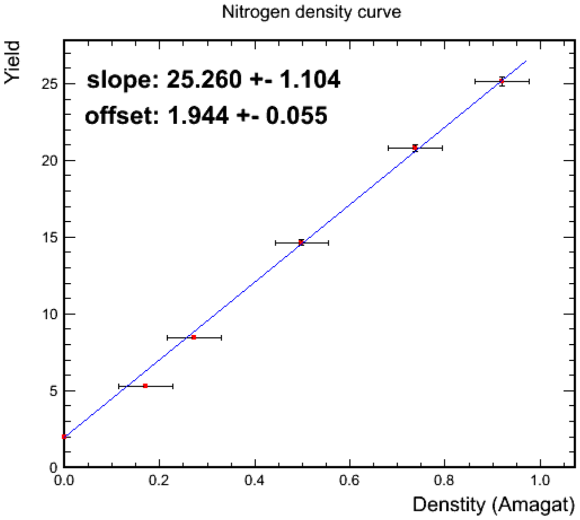

Figure 61: The density curve of the reference cell N_2 runs, fit to a straight line.

the RTD readings. The typical readings of the RTD are 46°C, 60°C and 46°C for the three RTDs attached to the reference cell (from upstream to downstream), respectively. The uncertainty in the pressure reading was assumed to be 1 psi, which is accounted for in the fitting procedure. The results of the ^{3}He and N_2 density curves are shown in Fig. 60 and Fig. 61, respectively. The results were fit to a straight line.

For the N_2 density curve, we assume that the radiative correction ratio for ^{14}N of the reference cell vs. the production cell is the same as that for ^{3}He, which has been explicitly calculated through a Monte-Carlo simulation. Further studies are on-going to estimate the uncertainties due to this approximation.

Yield from the Production Cell

The extracted yield defined in Eqs. 19 and 21 are shown for 9 runs in Figs. 62 and 63, after applying the ^{3}He and ^{14}N elastic cuts. The average yields are 178.29 ± 0.37 and 5.33 ± 0.04 for ^{3}He and ^{14}N, respectively.

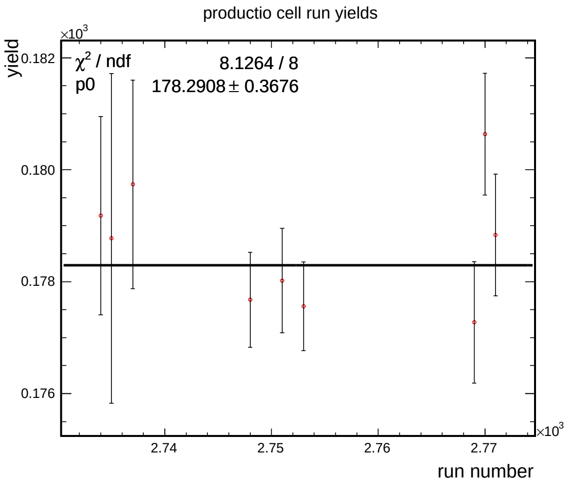

Figure 62: Yields with the ^{3}He elastic cut for the production-cell runs, fit to a constant. We enlarged the statistical error bars by a factor of 1.75 to achieve a reduced chi-squared close to 1.

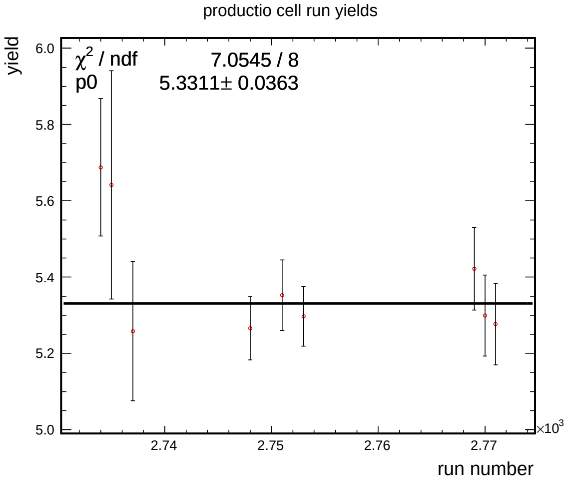

Figure 63: Yields for the production-cell runs with the ^{14}N elastic cut, fit to a constant.

N_2 Contamination

The ^{14}N elastic peak is at smaller values in the missing-mass spectrum than the ^{3}He elastic peak due the larger recoil of the ^{3}He nucleus; however, the inelastically scattered electrons from the ^{14}N nuclei appear underneath the ^{3}He elastic peak. This contamination needs to be removed to extract the pure ^{3}He yield. The factor $R_{\mathrm{N}/^3\mathrm{He}}$ (shown in Eq. 20) has been determined to be 1.38 ± 0.06, by comparing the^{14}N reference-cell data after applying the ^{3}He elastic cut, with those on the reference-cell ^{3}He runs (shown in Fig. 56). Figure 64 shows the yield vs. density for ^{14}N of the reference-cell runs after applying the ^{3}He elastic cut.

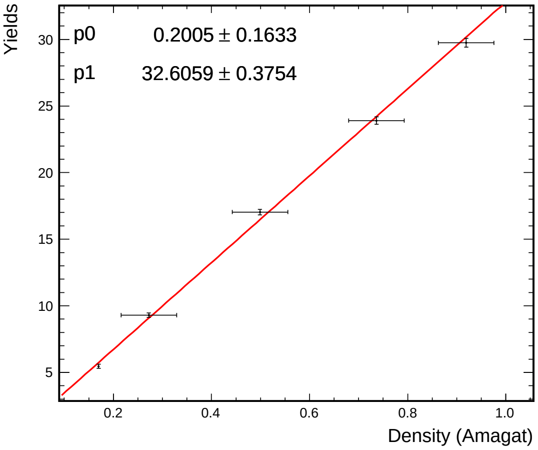

Figure 64: Yields for the reference-cell runs with the ^{3}He cuts, fit to a constant.

Results and Uncertainties

The fit shown in Fig. 61 yields a line with a slope of 25.260 ± 1.104 and an offset of 1.944 ± 0.055. From the analysis, we know that the ^{14}N yield in the production-cell runs is 5.33 ± 0.04, and from that we can extract the density of ^{14}N. Since the background in the production-cell runs can be different from that in reference-cell runs, we estimate the background of the production cell yield in the following way. From the wall and window thickness measurement, we know that the average thickness of the production-cell windows is 95% of the reference-cell windows. Thus, it is a reasonable assumption that the background of the production cell is 95% of the reference-cell background, so that the density of the ^{14}N in the production cell can be written as:

$$\rho_N^{prod} = \frac{Y_N^{prod} - 0.95 \cdot Bkg_N^{ref}}{K_N^{ref}} \tag{26}$$

resulting in a density of ^{14}N in the production cell of 0.138 ± 0.007 amagats. Y_N^{ref} is a normalization factor to convert the ^{14}N yield into density.

For the ^{3}He case, the situation is more complicated due to the ^{14}N contamination. Based on the same assumption for the background, the equation for ^{3}He can be written as

$$\rho_{he}^{prod} = \frac{(Y_{\mathrm{He}}^{prod} - 0.95 \cdot Bkg_{\mathrm{He}}^{ref}) \times (1 - R_{\mathrm{N}/^3\mathrm{He}} \cdot \rho_N^{prod}/\rho_{\mathrm{He}}^{prod})}{K_{\mathrm{He}}^{ref}}\,, \tag{27}$$

where the slope and the background of the ^{3}He density curve are extracted from Fig. 60 as 18.651 ± 0.117 and 2.120 ± 0.128, respectively. K_{He}^{ref} is a normalization factor to convert the ^{3}He yield into density. The ratio $R_{\mathrm{N}/^3\mathrm{He}}$ has been defined in Eq. 20 and is 1.38 ± 0.06 from the earlier analysis. Knowing the density of ^{14}N in the production cell, Eq. 27 becomes a two-order polynomial equation with $\rho_{he}^{prod.}$ as its only variable and the density of the ^{3}He in the production cell is determined to be 9.26 ± 0.06 amagats.

The radiative corrections were also applied without subtracting the yield of the empty-reference cell run, which is only expected to work if the contamination from the glass cell is small within our vertex cuts. This results in another ^{3}He density curve with a slope of 18.59 and an offset of 2.12. From these parameters, we calculate the density of the ^{3}He to be 9.29 amagats, consistent with the original result.

Summary

The production cell used in this work is called “Astralweek”, which was filled with 8.082 amagats of ^{3}He at UVa [10]. Two independent pressure-broadening measurements were done to check the filling density. The result from the UVa measurement is 8.182 amagats, while at JLab it was found to be 8.124 amagats, both with a relative uncertainty of 1.2%. When the cell is heated up, the temperature distribution model can give another 0.5% uncertainty. Hence, the calculated density has a relative uncertainty of up to 1.3%. It is worth noting that in the two pressure-broadening measurements, the ^{14}N density in the cell was assumed to be 1% of the ^{3}He density . Comparing the total density[10] in the cells provides an additional check of the target's density. The model yielded a total density is 9.31 ± 0.12 amagats, while this technique provided 9.40 ± 0.06 amagats for the sum of ^{3}He and ^{14}N gas.

3.8.3 Cross Check between MLE and Angular-bin-fit Methods

Introduction

Raw asymmetries were analyzed by two teams using different methods:

- The Blue Team used a super local pair and angular-bin-fit method. In this method the raw asymmetries are formed from local spin-pairs and then later combined. The combined data are then binned in several bins of ϕ_h and ϕ_S, where ϕ_h and ϕ_S are the azimuthal angle between the lepton plane and hadron plane and the azimuthal angle between the lepton plane and spin plane, respectively. Then, the Collins and Sivers moments are extracted from a two-dimensional fit to the corresponding angular modulation terms [11].
- The Red Team used a maximum-likelihood method (MLE). In this method, a likelihood estimator is constructed and the moments are extracted from the combined data. In contrast to the first method, the MLE extraction works on all data simultaneously and is susceptible to global problems such as yield drift.

The results between these two teams on the asymmetries and the angular modulations were cross-checked and the resulting difference is understood.

Cross Check of Angular Modulations

In Fig. 65 the extracted moments of $\sin(\theta_{\mathrm{S}})\sin(\phi_h+\phi_{\mathrm{S}})$ and $\sin(\theta_{\mathrm{S}})\sin(\phi_h-\phi_{\mathrm{S}})$ angular modulations are shown for the Double Spin Asymmetries (DSA) case; here θ_{S} is the spin polar angle. Although in the DSA case the physical asymmetries within the one-photon exchange approximation are zero, it demonstrates the consistency between the two analysis methods. Finally, the SSA modulation results were also found to be consistent within one third of the statistical uncertainty. The enhancement of the discrepancy from DSA to SSA are believed to be due to the bias generated by a yield drift in the MLE method.

Conclusion

In conclusion, results between the two teams were cross-checked. The difference is expected to be dominated by the fact that the current MLE method is biased by a drifting yield. Based on this result, the following conclusions can be made:

- The Blue Team method is better for the $^{3}\mathrm{He}^{\uparrow}(e,e'\pi^{\pm})$ channel SSA analysis
- Both the Blue Team and the Red Team results are good for the $^{3}\mathrm{He}^{\uparrow}(e,e'\pi^{\pm})$ channel DSA analysis. The results from both teams are consistent.
- The Red Team MLE method is better for the $^{3}\mathrm{He}^{\uparrow}(e,e'\pi^{\pm})$ channel SSA/DSA analysis by yielding an improved statistical precision[13].

---

[10] The sum of the ^{14}N and the ^{3}He densities

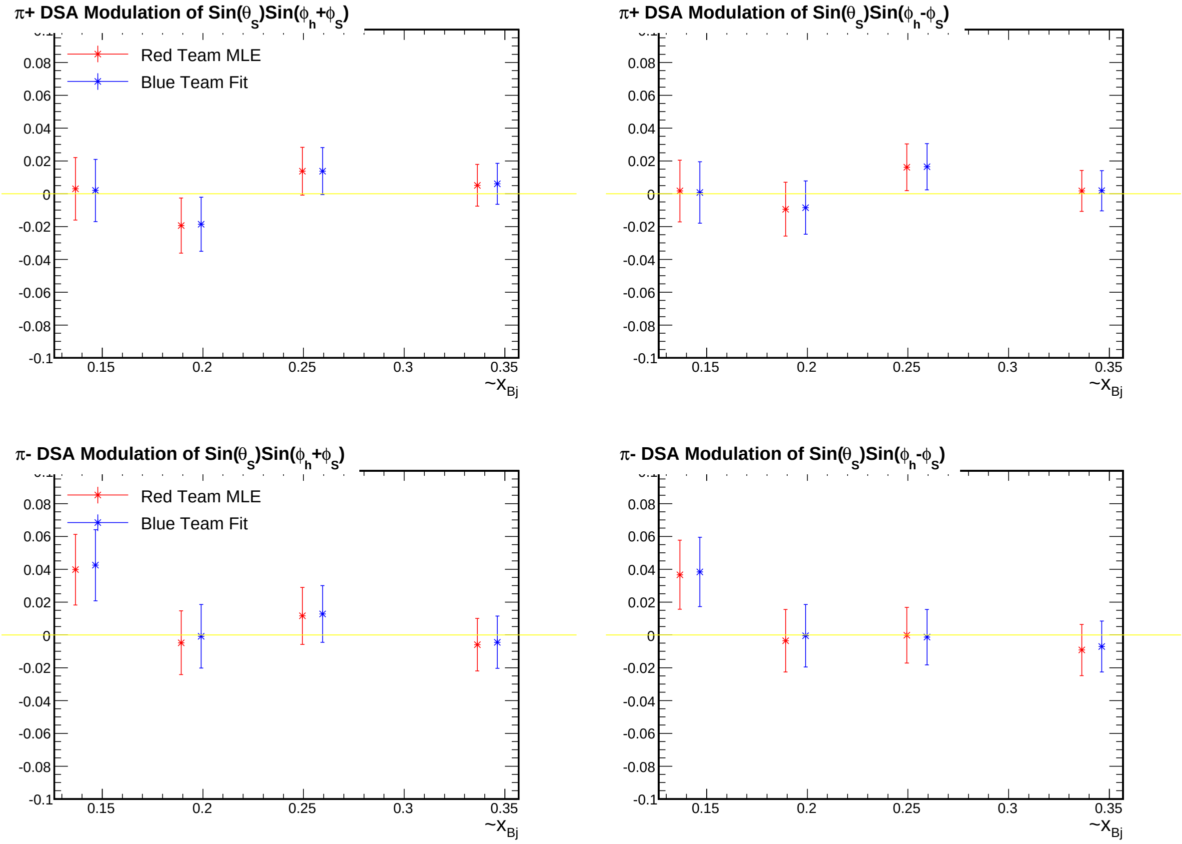

Figure 65: Cross-check of the two-term extraction of the DSA modulations $\sin(\theta_{\mathrm{S}})\sin(\phi_h+\phi_{\mathrm{S}})$ and $\sin(\theta_{\mathrm{S}})\sin(\phi_h-\phi_{\mathrm{S}})$ for the ${}^3\mathrm{He}^{\uparrow}(e,e'\pi^{\pm})$ channels. These two modulations are those of the Collins and Sivers terms in SSA. However, in DSA, they do not represent any physical asymmetries [12]. The target polarization scaling has been applied, while dilutions have not yet been taken onto account.

3.8.4 SIMC-Transversity

The standard Hall C Monte Carlo code SIMC was modified to include a realistic model of the BigBite spectrometer and a physics event generator for the Hall A transversity experiment E06-010. SIMC already included a realistic model of the acceptance and resolution of the Hall A High Resolution Spectrometers (HRSs), and a model for the unpolarized semi-inclusive N$(e, e'h^{\pm})X$ cross sections, making it a natural starting point for a Monte Carlo simulation of coincidence $(e, e'h^{\pm})$ for the analysis of E06-010. SIMC can also be used to calculate the radiative corrections to the SIDIS process. Furthermore, SIMC includes a model for exclusive ρ production, which can be used to estimate this important physics background to the dominant SIDIS reaction mechanism of current fragmentation.

In order to use SIMC in our analysis, we added a model for the BigBite spectrometer, including a realistic description of the BigBite optics derived from calibration data obtained during the transversity experiment, the geometry of the detectors including the MWDCs and shower counter, tracking resolution including energy loss and multiple scattering of the detected particles, and the energy resolution and trigger threshold of the BigBite shower counter. We also included realistic descriptions of the materials of the polarized ^{3}He target to calculate energy loss, multiple scattering and radiation of the incident and scattered particles and a simplified geometry of the target collimators, used to suppress scattering from the glass windows of the ^{3}He target. While the models of the spectrometer acceptance is still being improved, the semi-inclusive $^3\mathrm{He}(e, e'\pi^{\pm})X$ yields from SIMC are already in rather good agreement with the data, for electrons detected in BigBite with momenta above 1 GeV/c, as shown in Fig. 66. For lower momenta, SIMC overestimates the measured yield, mainly because problems experienced with the trigger threshold and efficiency during the experiment are not yet accurately described in SIMC. Additionally, the dependence of the BigBite acceptance on the position of the scattering vertex along the beam line is still in need of improvement.

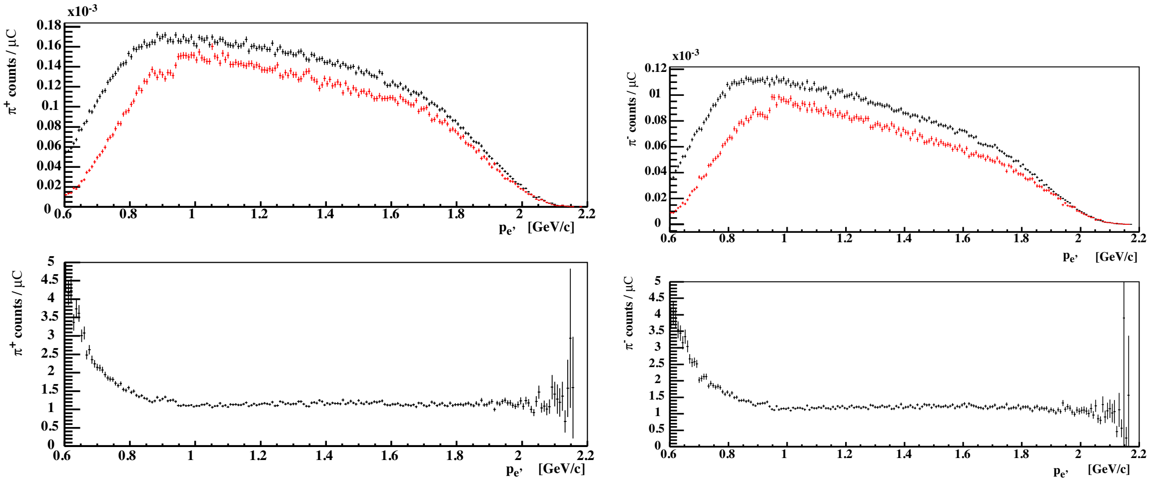

(a) $^3\mathrm{He}(e, e'\pi^+)X$.

(b) $^3\mathrm{He}(e, e'\pi^-)X$.

Figure 66: Comparison of SIMC (black) and data (red) yields for the $^3\mathrm{He}(e, e'\pi^+)X$ (left) and $^3\mathrm{He}(e, e'\pi^-)X$ (right) reactions as a function of electron (BigBite) momentum (top) and the ratio SIMC/data (bottom).

While the aforementioned imperfections of the BigBite acceptance model in SIMC require further improvement in order to use SIMC for the extraction of the SIDIS cross section, the model is already sufficiently close to the experimental data to be used for reliable systematic studies on the extraction of single-spin-asymmetries (SSAs), particularly the Collins and Sivers effects. The similarity between the real and simulated experimental acceptances is illustrated in Fig. 67, which shows the correlations between Bjorken x and Q^2, the invariant mass W, the hadron energy fraction z, and the missing mass W'. To study the effect of the finite spectrometer acceptance in the extraction of SSAs from the data, we added a physics event generator for SIDIS reactions on a transversely polarized ^{3}He target. Our SIDIS cross-section model for polarized ^{3}He assumes a simple incoherent sum over free nucleons at rest; i.e., $\sigma_{^3\mathrm{He}} = 2\sigma_p + \sigma_n$. The proton and neutron unpolarized SIDIS cross sections were calculated using an ideal leading-order approximation in which the SIDIS structure function is given by a sum over quark flavors of simple products of PDFs $q(x, Q^2)$ and fragmentation functions (FFs) $D_q^h(z, Q^2)$: $\sigma_h \propto \sum_q q(x, Q^2) D_h^q(z, Q^2)$. We used the leading-order versions of the MSTW2008 PDFs [14] and the recent DSS2007 FFs [15]. The transverse momentum dependence of the cross section was included assuming a standard Gaussian factorization, with quark-flavor and hadron-species independent widths $\left\langle k_\perp^2 \right\rangle = 0.25\ \mathrm{GeV}^2$ for the intrinsic quark transverse momentum, relative to the momentum transfer $\vec{q}$, and $\left\langle p_\perp^2 \right\rangle = 0.20\ \mathrm{GeV}^2$ for the intrinsic transverse momentum of the produced hadrons, relative to the fragmenting quarks. This results in an overall p_T^2-dependent cross-section weight of:

$$\frac{d\sigma}{dp_T^2 d\phi_h} \propto \frac{1}{2\pi(z^2 \left\langle p_\perp^2 \right\rangle + \left\langle k_\perp^2 \right\rangle)} e^{-\left(\frac{p_T^2}{z^2 \left\langle p_\perp^2 \right\rangle + \left\langle k_\perp^2 \right\rangle}\right)}, \tag{28}$$

where p_T^2 is the transverse momentum of the SIDIS hadron relative to $\vec{q}$. To calculate the SSAs resulting from the Collins and Sivers effects, we used the phenomenological global fits of Anselmino and collaborators [16] for the Collins moments and [17] for the Sivers moments.

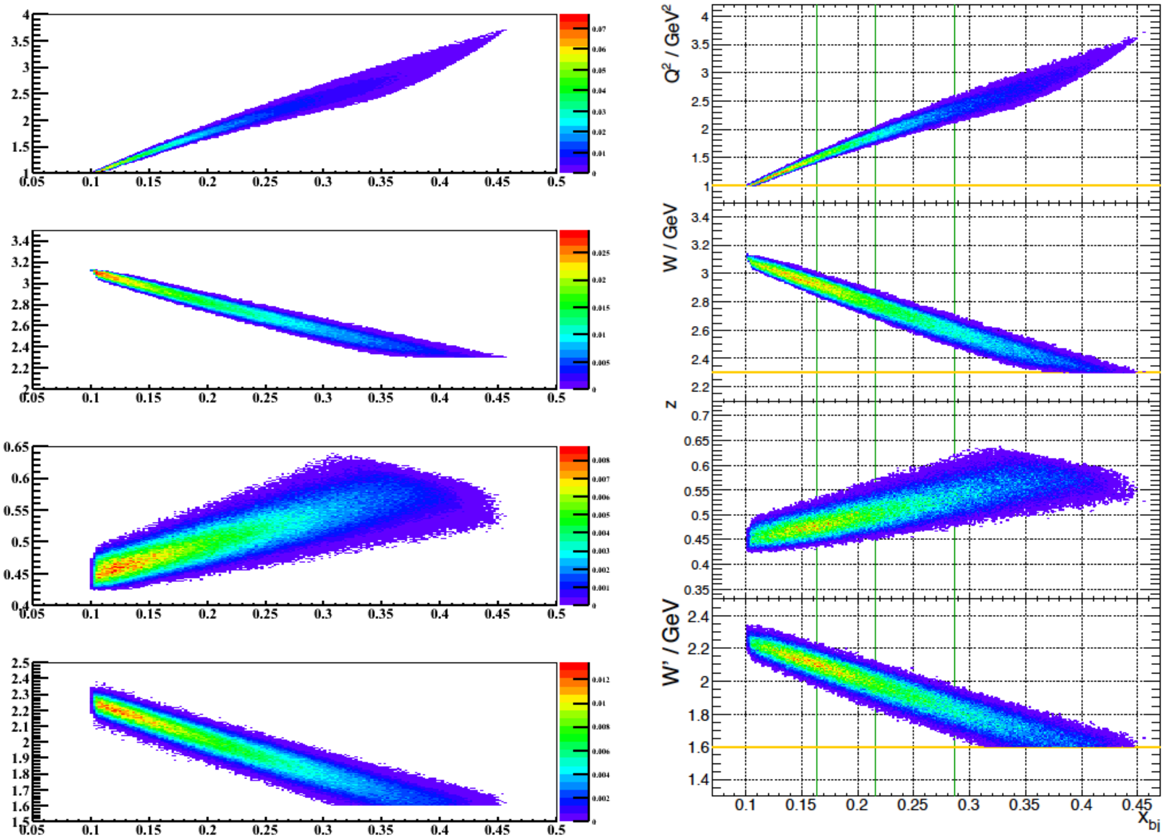

(a) SIMC kinematic phase space

(b) Data kinematic phase space

Figure 67: Comparison of the phase-space coverage in SIMC and data for Q^2, W, z, and W' as a function of x.

In SIMC, events are "injected" into the spectrometers with all independent variables (interaction vertex, particle angles, particle momenta) randomly generated within a phase space, that exceeds the size of the spectrometer acceptance for each of the scattered particles. Each scattered particle is then transported through its respective spectrometer model, and checked against numerous apertures along the way, taking into account the decay of unstable particles where applicable. If the particle reaches the detector, its trajectory is then "smeared" for detector resolution, and the smeared track is then transported back to the target. If both the scattered electron and hadron tracks pass all apertures of Bigbite and the left HRS, respectively, the cross section corresponding to the randomly generated kinematics of both particles is calculated. In the case of SIDIS, the unpolarized cross section is fully differential in x, Q^2, z, p_T^2, and ϕ_h. The Collins and Sivers effect asymmetries were included in the cross section as:

$$\begin{aligned}\sigma_{UT}(x, Q^2, z, p_T^2, \phi_h, \phi_S) &= \sigma_0(x, Q^2, z, p_T^2)\frac{1}{2\pi}\Big[1 + \\ &\quad |\mathbf{S}_T|\, A_{UT}^{Coll}(x, Q^2, z, p_T^2)\sin(\phi_h + \phi_S) + \\ &\quad |\mathbf{S}_T|\, A_{UT}^{Siv}(x, Q^2, z, p_T^2)\sin(\phi_h - \phi_S)\Big],\end{aligned} \tag{29}$$

where ϕ_h and ϕ_S are, respectively, the azimuthal angles of the hadron transverse momentum and the target transverse spin relative to $\vec{q}$ and $|\mathbf{S}_T|$ is the transverse component of the target polarization.

Equal integrated luminosities were simulated in each of the four target spin directions used in the transversity experiment (up, down, left, right). The output of SIMC is an ntuple with events distributed according to the acceptance-convoluted cross section, which is used for further analysis. The Collins and Sivers moments were extracted from these simulated data, which are smeared by detector resolution, energy loss, multiple scattering and radiative corrections (if applicable), using the same analysis code applied to the real data and compared to the theoretical (input) asymmetries. Our studies so far indicate that the systematic effects due to finite acceptance and detector resolution in a simultaneous maximum-likelihood extraction of the Collins and Sivers moments are small for the case when no other, "unwanted" azimuthal modulations of the cross section are present. Figure 68 shows the results of this extraction for the case where the input Collins and Sivers asymmetries are taken from the phenomenological fits described above. A simultaneous maximum-likelihood extraction of the Collins and Sivers moments from a high-statistics SIMC run successfully reproduces the simulated asymmetries, while a one-term extraction shows the systematic effects of neglecting the other term, which results from the finite experimental acceptance. Furthermore, for the theory curves used in the simulation, the effects of bin-centering are small, as the average asymmetries in the four x bins used in our analysis are close to the theoretical asymmetries evaluated at the average kinematics of the chosen bins.

In an additional study, the analysis of small-statistics subsamples of a large-statistics SIMC run was performed in order to investigate the bias and efficiency of the maximum-likelihood method used in the analysis. In Figs. 69 and 70, a high-statistics SIMC data set with, respectively, 10% input Sivers and Collins asymmetries was subdivided into approximately 50 trials with statistics equal to the π^+ data of experiment E06-010. In both cases, at least within the statistical precision of the study, the results of the maximum-likelihood extraction for any given trial are Gaussian-distributed about the input value, with a σ in very good agreement with the average estimated statistical uncertainty in the extraction. This study shows that the maximum-likelihood estimators (MLE) used for the analysis are unbiased (the average extracted result for a "large" number of trials is equal to the "true" asymmetry) and efficient (the statistical uncertainty calculated in the MLE extraction equals the variance of the results obtained in a large number of independent trials, which defines the statistical uncertainty). Similar results are obtained for both Collins and Sivers asymmetries when the SIMC data are subdivided into approximately 2500 trials with even lower statistics equal to the K^- data of E06-010, shown in Figs. 71 (10% Sivers) and 72 (10% Collins). Studies of the systematic effects of such "unwanted" terms as the "Pretzelosity" asymmetry, higher-twist modulations of A_{UT}, and the Cahn and Boer-Mulders effects in the unpolarized cross section are ongoing. Further investigations will include radiative corrections, exclusive ρ backgrounds, nuclear effects in ^{3}He, and a further improvement of the spectrometer acceptance models, particularly for BigBite, towards an extraction of the SIDIS cross section for ^{3}He.

3.8.5 Preliminary Results

The upper panels of Fig. 73 show the moments of the ^{3}He Collins single-spin asymmetry for π^+ (left) and π^- (right) channels, respectively. The Collins moments on ^{3}He are not large, mostly consistent with zero within the statistical uncertainties, except for the π^+ channel at the highest x-bin, where data favors a negative Collins moment.

The lower panels of Fig. 73 show the moments of the ^{3}He Sivers single-spin asymmetry for π^+ (left) and π^- (right) channels. Again, the Sivers moments on ^{3}He are relatively small, at the level of a few percent. For the π^+ channel, which favors the d-quark in nucleon, as π^+ carries a valence u-quark from the neutron, and it is coupled with the "favored" fragmentation function, the data suggest negative values for the Sivers moment, in general agreement with the trend predicted by Anselmino *et al*, noticeably smaller in magnitude. On the other hand, the Sivers moment for the π^+ channel indicates a different trend, slightly favoring positive values.

References

[1] JLab E06-010, Spokespersons; J.-P. Chen, E. Cisbani, H. Gao, X. Jiang, and J.-C. Peng.

[2] M. G. Alekseev *et al.*, Phys. Lett., **B692**, 240 (2010).

[3] A. Airapetian *et al.*, Phys. Rev. Lett., **94**, 012002 (2005).

[4] A. Airapetian it et al., Phys. Rev. Lett., **103**, 152002 (2009).

[5] Kevin Kramer *et al.*, Nucl. Instrum. Meth., **A582**, 318 (2007).

[6] X. Qian. *Measurement of Single Spin Asymmetry in* $n^\uparrow(e,e'\pi^\pm)x$ *on Transversely Polarized* ^{3}*He*, `http://www.tunl.duke.edu/~mep/thesis/Qian_dissertation.pdf`, 2010.

[7] https://hallaweb.jlab.org/dvcslog//transversity/208.

[8] Jin Huang, private communication.

[9] A. Deur. *Single Arm Monte Carlo for Polarized* ^{3}*He Experiments in Hall A*, `http://www.jlab.org/e94010/tech_note_33.ps.gz`.

[10] Web page of all production cells' information in University of Virginia. `http://galileo.phys.virginia.edu/research/groups/spinphysics/transversity/transcells.html`.

[11] K. Allada *et al.* *Hall-A Neutron Transversity Experiment (E06-010): Analysis Not*, `http://www/~kalyan/longnote/longnote.pdf`.

[12] A. Bacchetta *et al.* JHEP, **0702** 093, (2007).

[13] J. Huang. Transversity collaboration meeting talk, may 2010. `http://www.jlab.org/~jinhuang/Meeting/2010.05.22%20Transversity%20Collaboration%20Meeting/DSA.pdf`.

[14] A. Martin, W. Stirling, R. Thorne, and G. Watt. The European Physical Journal C - Particles and Fields, **63**, 189 (2009). 10.1140/epjc/s10052-009-1072-5.

[15] Daniel de Florian, Rodolfo Sassot, and Marco Stratmann. Phys. Rev. **D 75**, 114010, (2007).

[16] M. Anselmino, M. Boglione, U. D'Alesio, A. Kotzinian, F. Murgia, A. Prokudin, and C. Türk. Phys. Rev. **D75**, 054032 (2007).

[17] M. Anselmino, M. Boglione, U. D'Alesio, A. Kotzinian, F. Murgia, and A. Prokudin. Phys. Rev. **D 72**, 094007 (2005).

[18] M. Anselmino *et al.* Phys. Rev. **D 71**, 074006 (2005).

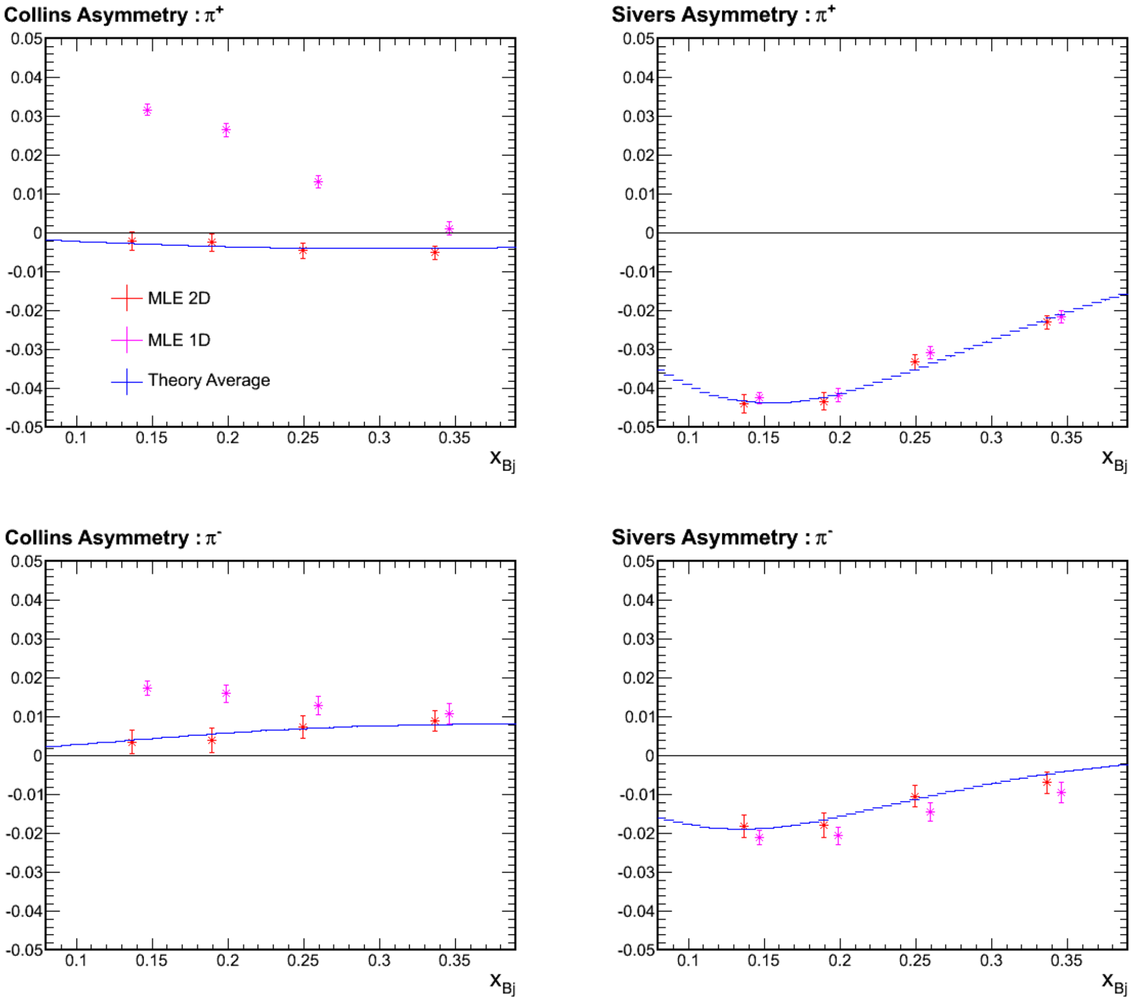

Figure 68: Successful maximum-likelihood extraction of the Collins and Sivers moments from SIMC-generated “pseudo-data”, using the same analysis code applied to the real data. “MLE 1D” refers to a one-term extraction of the term in question, while “MLE 2D” refers to a two-term Collins + Sivers extraction. “Theory average” represents the statistical average of the asymmetry within the fine bins in x_{Bj} shown.

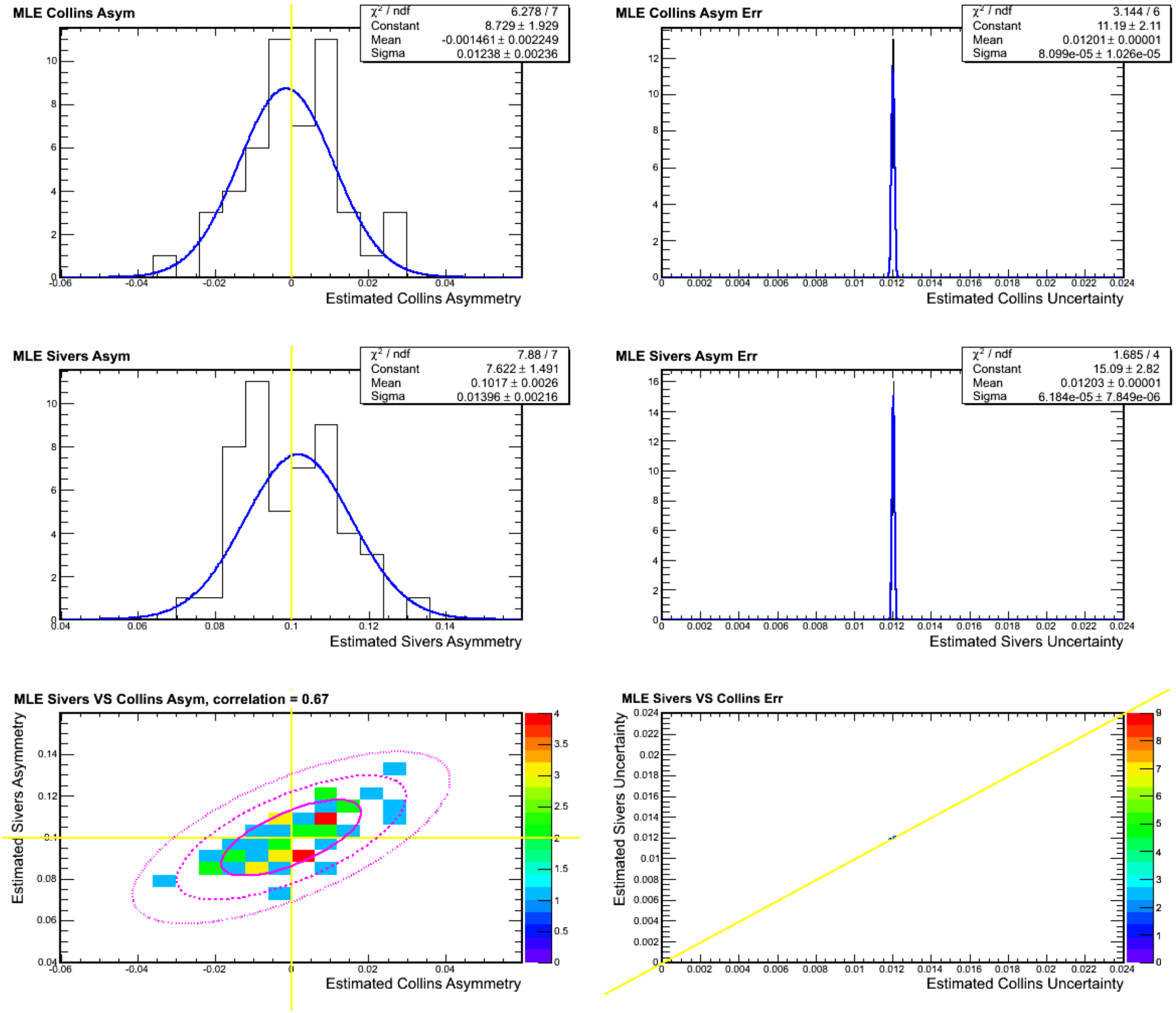

Figure 69: Results of subdividing a high-statistics SIMC run into 50 trials with statistics equal to the π^+ data from E06-010, for an input asymmetry of 10% Sivers and 0% Collins.

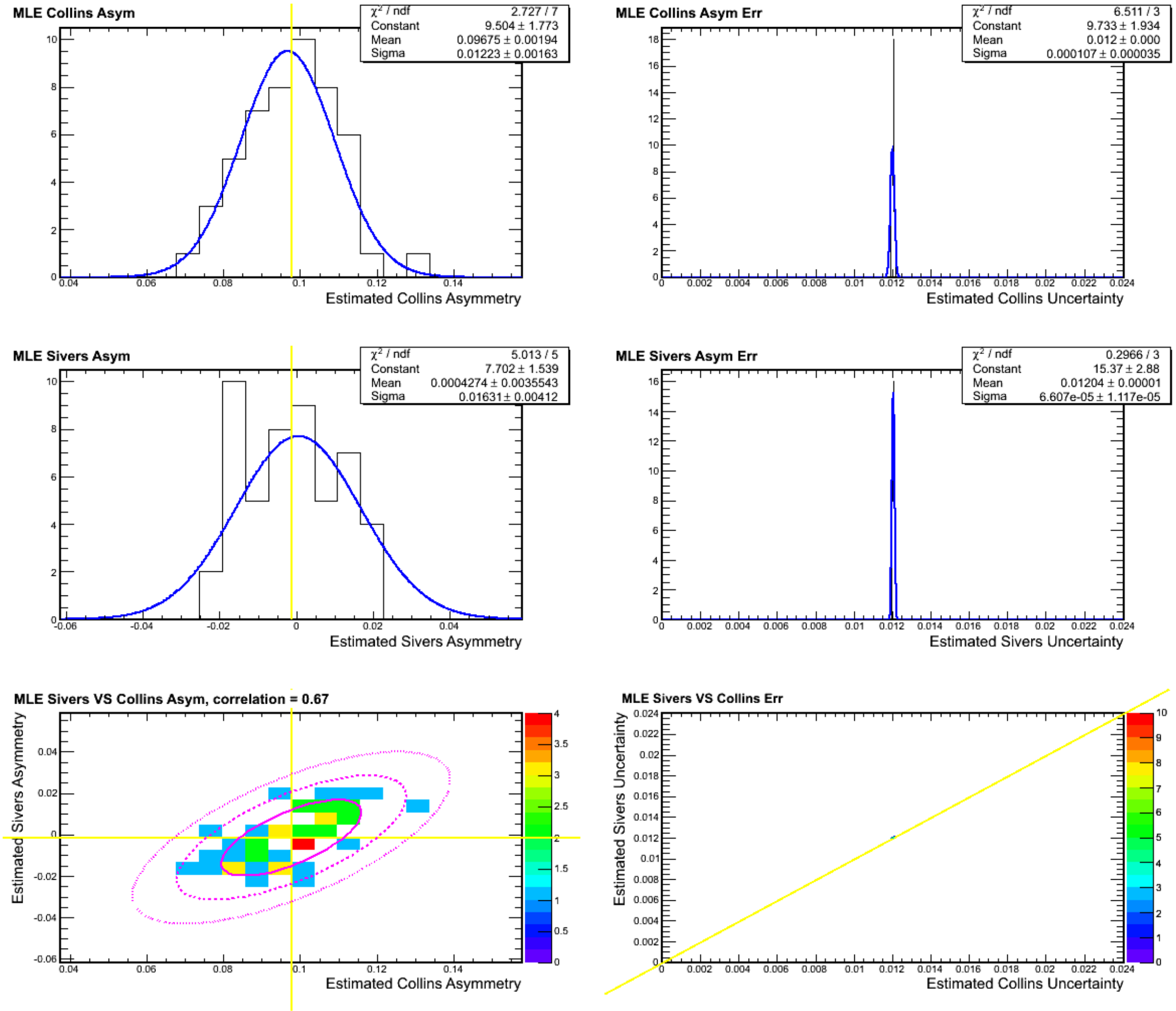

Figure 70: Results of subdividing a high-statistics SIMC run into 50 trials with statistics equal to the π^+ data from E06-010, for an input asymmetry of 0% Sivers and 10% Collins.

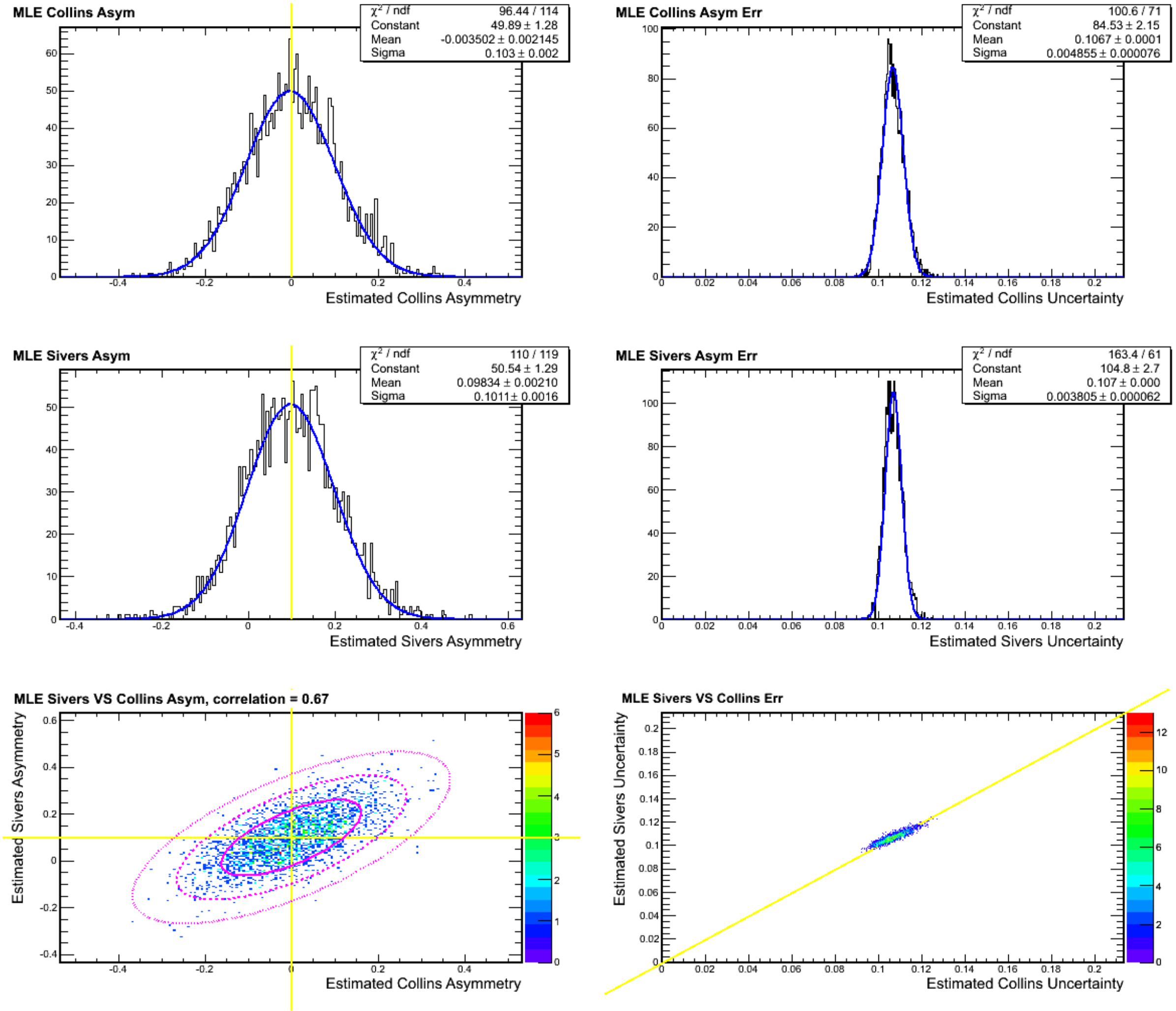

Figure 71: Results of subdividing a high-statistics SIMC run into 2500 trials with statistics equal to the K^- data from E06-010, for an input asymmetry of 10% Sivers and 0% Collins.

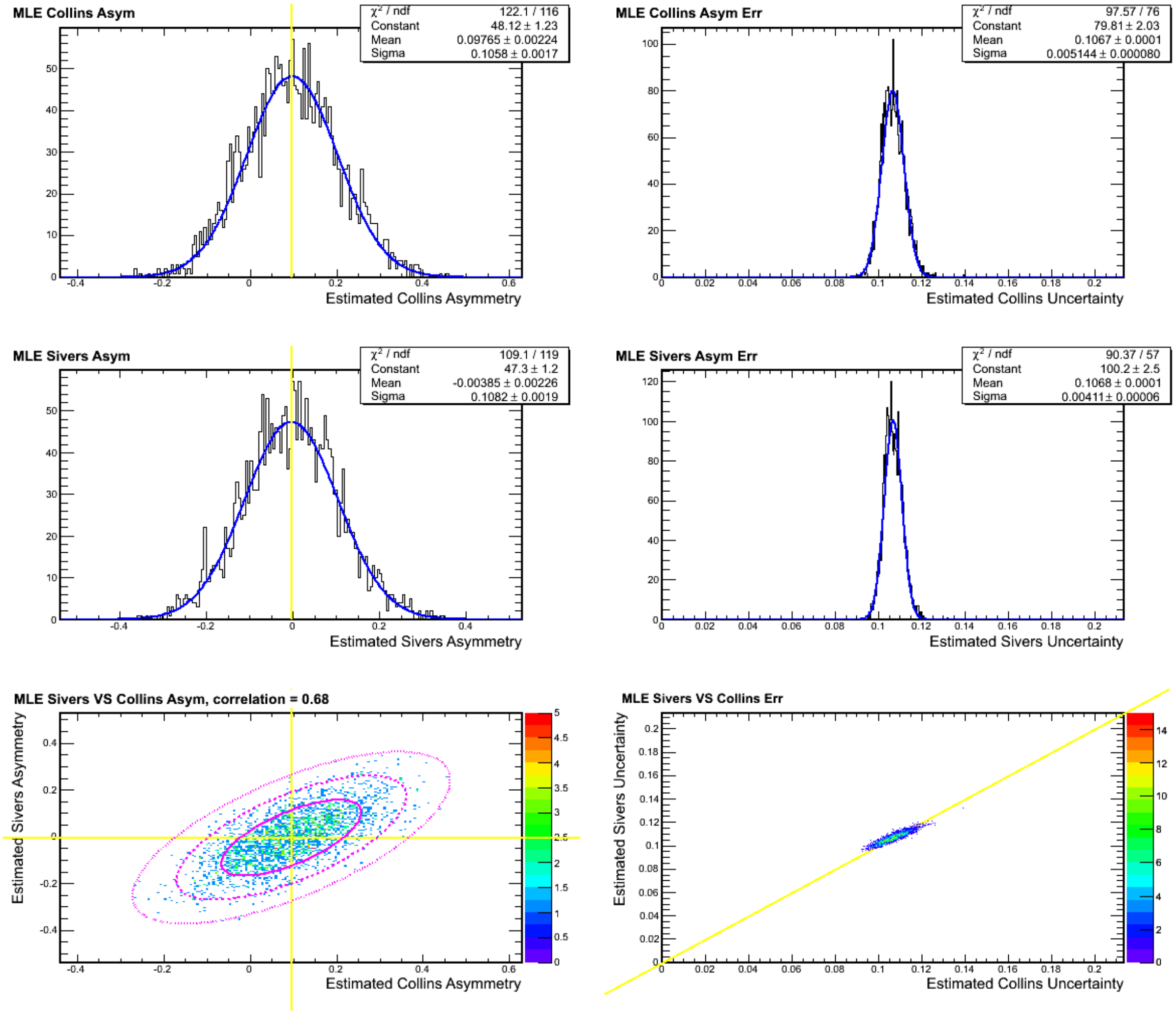

Figure 72: Results of subdividing a high-statistics SIMC run into 2500 trials with statistics equal to the K^- data from E06-010, for an input asymmetry of 0% Sivers and 10% Collins.

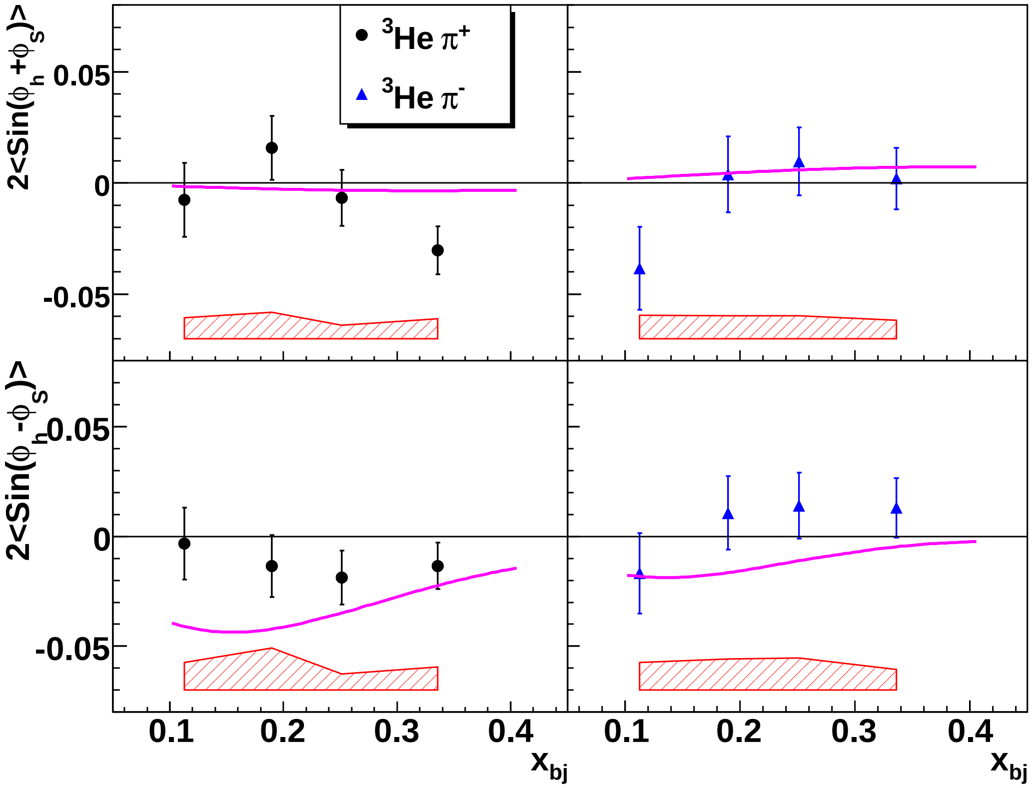

Figure 73: The preliminary results for the Collins and Sivers moments of ^{3}He. The error bars represent the statistical uncertainties. The different sources of systematic uncertainties are shown as a red band. The magenta curve represents the theoretical calculation by Anselmino *et al.* [16, 18]

4 Publications

1. M. Paolone *et al.*, Polarization Transfer in the ^{4}He(e,e'p)^{3}He Reaction at $Q^2 = 0.8$ and 1.3 GeV^2, Phys. Rev. Lett. **105**, 072001 (2010).
2. M. Coman *et al.*, Cross sections and Rosenbluth separations in H(e, e'K$^+$)Λ up to $Q^2 = 2.35$ GeV^2, Phys. Rev. **C81**, 052201 (2010).
3. I. Pomerantz *et al.*, Hard Photodisintegration of a Proton Pair, Phys. Lett. **B684**, 106 (2010).
4. S. Riordan *et al.*, Measurements of the electric form factor of the neutron up to Q^2=3.4 GeV^2 using the reaction ^{3}He(e,en)pp, Phys. Rev. Lett. **105**, 262302 (2010), 1008.1738 [nucl-ex].
5. Y. Qiang *et al.*, Properties of the $\Lambda(1520)$ resonance from high-precision electroproduction data, Phys. Lett. **B694**, 123 (2010).

5 Theses

1. *High Precision Measurement of the Proton Elastic Form Factor Ratio at Low* Q^2, Xiaohui Zhan, MIT
2. *Measurement of Single-Spin Asymmetries in the Semi-Inclusive DIS reaction* $n^{\uparrow}(e, e'\pi^{+})X$ *using Transversely Polarized* ^{3}*He Target*, Kalyan Allada, University of Kentucky
3. *Measurement of Single-Spin Asymmetries in the Semi-Inclusive DIS reaction* $n^{\uparrow}(e, e'\pi^{-})X$ *using Transversely Polarized* ^{3}*He Target*, Chiranjib Dutta, University of Kentucky
4. *Measurement of the Target-Normal Single-Spin Asymmetry* A_y^n *in the Deep-Inelastic Region from the Reaction* $^3He^{\uparrow}(e,e')$, Joe Katich, College of William & Mary
5. *Measurement of the Single-Spin Asymmetry in the* $n^{\uparrow}(e, e'\pi^{-})X$ *Reaction on a Transversely Polarized* ^{3}*He Target*, Xin Qian, Duke University

6 Hall A Collaboration Member List

Argonne National Lab
John Arrington
Frank Dohrmann
Paul Reimer
Krishni Wijesooriya
Budker Institute of Nuclear Physics
Dima Nikolenko
Igor Rachek

Cairo University
Hassan Ibrahim

California Institute of Technology
Steffen Jensen
Cathleen Jones

California State University
Konrad A. Aniol
Juan Carlos Cornejo
Martin B. Epstein
Dimitri Margaziotis

Carnegie Mellon University
Gregg Franklin
Megan Friend
Diana Parno
Brian Quinn
Luminita Todor

China Institute of Atomic Energy (CIAE)
Xiaomei Li
XinHu Yan
Shuhua Zhou

College of William and Mary
David S. Armstrong
Todd Averett
Keith Griffioen
Joe Katich
Aidan Kelleher
Lubomir Pentchev
Charles Perdrisat
Bo Zhao

Dapnia/SphN
Etienne Burtin
Christian Cavata
Nicole d'Hose
Jean-Eric Ducret
Stephanie Escoffier
Bernard Frois
Sophie Kerhoas

David Lhuillier
Jacques Marroncle
Damien Neyret
Stephane Platchkov
Thierry Pussieux
Franck Sabatie
Antonin Vacheret
Pascal Vernin

Duke University
Steve Churchwell
Haiyan Gao
Calvin Howell
Min Huang
Xin Qian
Yi Qiang
Richard Walter
Qiujian Ye

Faculte des Sciences de Monastir (Tunisia)
Malek Mazouz

Florida International University
Armando Acha
Werner Boeglin
Luminiya Coman
Marius Coman
Hari Khanal
Laird Kramer
Pete Markowitz
Brian Raue
Jeorg Reinhold

Fudan University
Xiaofeng Zhu

General Electric
Jianguo Zhao

Gent State University
Natalie Degrande
Luc Van de Hoorebeke
Robert Van de Vyver

Gesellschaft fur Schwerionenforschung (GSI)
Javier Rodriguez Vignote

Hampton University
Leon Cole
Ashot Gasparian
Peter Monaghan

Harvard Medical School
Hong Xiang

Harvard University
Richard Wilson

Hebrew University of Jerusalem
Guy Ron

INFN/Bari
Raffaele de Leo

INFN/Catania
Vincenzo Bellini
Sutera Concetta Maria
Antonio Guisa
Francesco Mammoliti
Giuseppe Russo
Maria Leda Sperduto

INFN/Roma
Marco Capogni
Francesco Cusanno
Salvatore Frullani
Franco Garibaldi
Franco Meddi
Guido Maria Urciuoli
Evaristo Cisbani
Rachel di Salvo
Mauro Iodice

Institut de Physique Nucleaire
Louis Bimbot

ISN Grenoble
Serge Kox
Jean Mougey
Gilles Quemener
Eric Voutier

Jefferson Lab
Alexandre Camsonne
Larry Cardman
Jian-Ping Chen
Eugene Chudakov
Kees de Jager
Alexandre Deur
Ed Folts
David Gaskell
Javier Gomez
Ole Hansen
Douglas Higinbotham
Tanja Horn
Mark K. Jones
John Lerose
Bert Manzlak

David Meekins
Bob Michaels
Sirish Nanda
Noel Okay
Lester Richardson
Yves Roblin
Arun Saha
Brad Sawatzky
Jack Segal
Dennis Skopik
Patricia Solvignon
Mark Stevens
Riad Suleiman
Vincent Sulkosky
Stephanie Tysor
Bogdan Wojtsekowski

Jozef Stefan Institute
Miha Mihovilovic
Simon Sirca

Kent State University
Bryon Anderson
Mina Katramatou
Elena Khrosinkova
Elena Long
Richard Madey
Mark Manley
Gerassimos G. Petratos
Andrei Semenov
John Watson

Kharkov Institute of Physics and Technology
Oleksandr Glamazdin
Viktor Gorbenko
Roman Pomatsalyuk

Kharkov State University
Pavel Sorokin

Lanzhou University
Yi Zhang

Longwood University
Tim Holmstrom
Keith Rider
Jeremy St. John
Wolfgang Troth

Los Alamos Laboratory
Lei Guo
Xiaodong Jiang
Han Liu
Ming Xiong Liu

LPC Clermont-Ferrand France
Pierre Bertin
Helene Fonvielle
Eric Fuchey
Florian Itard
Bernard Michel
Carlos Munoz Camacho

Mississippi State University
Dipangkar Dutta
Amrendra Narayan
Nuruzzaman

MIT
Bill Bertozzi
Shalev Gilad
Jin Huang
Bryan Moffit
Navaphon Tai Muangma
Kai Pan
Andrew Pucket
Nikos Sparveris
Wang Xu
Xiaohui Zhan
Cesar Fernandez Ramirez

Negev Nuclear Research Center
Sharon Beck
Arie Beck

NIKHEF
Jeff Templon

Norfolk State University
Vina Punjabi

North Carolina Central University
Benjamin Crowe
Branislav (Branko) Vlahovic

Northwestern University
Issam Qattan
Ralph Segel

Ohio University
Julie Roche

Old Dominion University
Gagik Gavalian
Wendy Hinton
Jeff Lachniet
Larry Weinstein
Charles Hyde

Pacific Northwest National Lab
Kathy McCormick
Brian Milbrath

Princeton University
Ioannis Kominis

Regina University
Alexander Kozlov

Renaissance Tech
Robert Lourie
Joseph Mitchell
Paul Ulmer

Rutgers University
Lamiaa El Fassi
Ron Gilman
Gerfried Kumbartzki
Ronald Ransome
Elaine Schulte

Saint Norbert College
Michael Olson

Seoul National University
Seonho Choi
Byungwuek Lee

Smith College
Piotr Decowski

St Mary's University
Adam Sarty
Jackie Glister

SUBATECH
Jacques Martino

Syracuse University
Zafar Ahmed
Richard Holmes
Abdurahim Rakhman
Paul A. Souder

Tel Aviv University
Nathaniel Bubis
Or Chen
Igor Korover
Jechiel Lichtenstadt
Eli Piasetzky
Ishay Pomerantz
Ran Shneor

Temple University
David Flay
Sebastian Incerti
Zein-Eddine Meziani
Matthew Posik
Huan Yao

Tohoku University
Kouichi Kino
Kazushige Maeda
Teijiro Saito
Tatsuo Terasawa
H. Tsubota

Universidad Complutense de Madrid (UCM)
Joaquin Lopez Herraiz
Luis Mario Fraile
Maria Christina Martinez Perez
Jose Udias Moinelo

Universitat Pavia
Sigfrido Boffi

University La Sapienza of Rome
Fulvio De Persio

University of Glasgow
John Annand
David Hamilton
Dave Ireland
Ken Livingston
Dan Protopopescu
Guenther Rosner

University of Illinois
Ting Chang
Areg Danagoulian
Alan Nathan
J.C. Peng
Mike Roedelbronn
Youcai Wang
Lindgyan Zhu

University of Kentucky
Kalyan Allada
Dan Dale
Chiranjib Dutta
Tim Gorringe
Wolfgang Korsch
Piotr Zolnierczuk

University of Lund
Kevin Fissum

University of Maryland
Elizabeth Beise
Fatiha Benmokhtar
Herbert Breuer
George Chang
Nicholas Chant
Harry Holmgren
Philip Roos

University of Massachusetts, Amherst
Krishna S. Kumar
Dustin McNulty
Luis Mercado
Jon Wexler

University of New Hampshire
John Calarco
Greg Hadcock
Bill Hersman
Maurik Holtrop
Donahy John
Mark Leuschner
Sarah Phillips
Karl Slifer
Timothy Smith

University of Regina
Ed Brash
Garth Huber
George Lolos
Zisia Papandreou

University of Saskatchewan
Ru Igarashi

University of Science and Technology of China (USTC)
Yi Jiang
Hai-jiang Lu
Yunxiu Ye

University of South Carolina
Simona Malace
Mike Paolone
Steffen Strauch

University of Virginia
Khem Chirapatpimol
Brandon Craver
Mark Dalton
Xiaoyan Deng
Gordon D. Gates
Mitra Hashemi Shabestari
Ge Jin

Sudirukkuge Tharanga Jinasundera
Richard Lindgren
Nilanga Liyanage
Vladimir Nelyubin
Blaine Norum
Kent Paschke
Seamus Riordan
Oscar Rondon
Rupesh Silwal
Jaideep Singh
Ramesh Subedi
Kebin Wang
Diancheng Wang
Xiaochao Zheng
Jiayao Zhou

Yamagata University
Seigo Kato
Hiroaki Ueno

Yerevan Physics Institute
Nerses Gevorgyan
Edik Hovhannisyan
Armen Ketikyan
Vahe Mamyan
Samvel Mayilyan
Artush Petrosyan
Albert Shahinyan
Hakob Voskanian

Past Members
Mattias Anderson
Maud Baylac
Hachemi Benaoum
J. Berthot
Tim Black
Alexander Borissov
Vincent Breton
Zhengwei Chai
Pibero Djawotho
Kim Egiyan
Catherine Ferdi
Robert Feuerbach
Mike Finn
Oliver Gayou
Charles Glashausser
Brian Hahn
Riccardo Iommi
Stephanie Jaminion
Lisa Kaufman
James D. Kellie
Ameya Kolarkar
Norm Kolb
Kevin Kramer

Elena Kuchina
Serguei Kuleshov
Geraud Lavessiere
Antonio Leone
Meihua Liang
Justin McIntyre
Wilson Miller
Pierre Moussiegt
Roberto Perrino
Bodo Reitz
Rikki Roche
David Rowntree
Gary Rutledge
Marat Rvachev
Neil Thompson
Dan Watts
Jingdong Yuan
Jingdong Zhou